Title	Study of Spin-Polarized Scanning Electoron Microscopy for Observing Magnetic Domains
Author(s)	松山, 秀生
Citation	大阪大学, 1994, 博士論文
Version Type	VoR
URL	https://doi.org/10.11501/3097508
rights	
Note	

Study of Spin-Polarized Scanning Electron Microscopy for Observing Magnetic Domains

by
Hideo Matsuyama

1994

CONTENTS

List of Abbreviations

Abstract

1. Introduction 1

2. Spin-Polarized Scanning Electron Microscopy (spin SEM) 5

§2.1 Polarized Electrons 5

§2.2 Spin Polarization of Secondary Electrons 5

§2.3 Spin Detector 7

§2.4 Spin-Polarized Scanning Electron Microscopy 10

References 14

3. Application of Spin SEM

- Surface Néel Wall Observation - 15

§3.1 Introduction 15

§3.2 Experimental 15

§3.3 Results and Discussion 16

§3.4 Conclusions 18

References 24

4. Data Acquisition and Display System (DAD System) 25

§4.1 Introduction 25

§4.2 Function of System 27

§4.3 Apparatus 31

§4.4 Results and Discussion 34

§4.5 Conclusions 52

References 54

5. Application of DAD System

- Side Plane Domain Observation of Fe-C/Ni-Fe/BN Multilayers - 55

§5.1 Introduction 55

§5.2 Experimental 56
§5.3 Domain Observations 56
§5.4 Conclusions 62
References 63
6. 20-nm Resolution Spin SEM 64
§6.1 Introduction 64
§6.2 System Design for High Spatial Resolution 65
§6.2.1 Necessary Conditions 65
§6.2.2 Electron Gun 67
§6.2.3 Objective Lens 67
§6.2.4 Mott Detector 70
§6.2.5 Secondary Electron Collector and Transport Optics 70
§6.3 *S/N* of the Image 73
§6.4 System 75
§6.5 Experimental Procedure 75
§6.6 Results and Discussion 77
§6.7 Conclusions 81
References 82
7. Application of 20-nm Resolution Spin SEM
- Domain Observation of Longitudinal Thin-Film Media - 83
§7.1 Introduction 83
§7.2 Experimental Procedure 83
§7.3 Results and Discussion 84
§7.4 Conclusions 90
References 91
8. Summary 92
Acknowledgment 94

List of Publications 95

List of Abbreviations

AD	analog-to-digital
CRT	cathode ray tube
DA	digital-to-analog
DAD	data acquisition and display
DSP	digital signal processor
ECW	edge curling wall
FCI	flux changes per inch
FWHM	full width at half maximum
I/O	input/output
MFM	magnetic force microscopy
SEM	scanning electron microscopy
S/N	signal to noise ratio
TEM	transmission electron microscopy
WD	working distance

Abstract

A new data-acquisition and display (DAD) system designed for the spin-polarized scanning electron microscopy (spin SEM), which is able to observe magnetic microstructures, has been developed. Moreover, a completely redesigned spin-SEM with the spatial domain-resolution of 20 nm has been developed.

The DAD system is composed of 32 frame memories (512 x 512 x 16 bit), an image processor with two high-speed digital signal processors, and a 1280 x 1024 pixel color monitor. It has the following capabilities: electron probe control; high-speed (21 s/512 x 512 pixel image) computing and recording of two components (P_x, P_y) of secondary-electron spin polarization; computing and displaying the average P_x and P_y obtained by repetitive scanning; domain image formation for an arbitrary component from (P_x, P_y) data (8 s/512 x 512 pixel image); variable speed scanning to obtain a homogeneous quality image in minimum time, even when secondary-electron intensity varies due to surface inclination; two-dimensional display of polarization vector distribution; and angle image of the magnetization direction in both black and white and color representation.

We applied the spin SEM with the DAD system to observe magnetization distributions on the top and side planes of four-magnetic layer (0.5 μm/layer) strips (300 x 50 μm^2). From the domain images of the side planes, the magnetization direction of each magnetic layer is studied. The strips do not always show the predicted energy minimum magnetic structure, in which the magnetization direction alternates layer by layer.

To improve the spatial resolution of the spin SEM, we have used a thermal-assisted field emission gun to provide a high, stable emission current. In addition, we have developed an objective lens whose conical shape accommodates a short working distance and enables a secondary electron collector to be placed close to the sample to collect most of the secondary electrons. Included in this system are a newly developed high-efficiency Mott detector, a low-

loss secondary-electron collector, and transport optics. As a result, 20-nm resolution has been achieved.

With the high resolution spin SEM, a noise generating mechanism is studied by observing recorded bits of two kinds of high-density recording media, in the 50-140 kFCI range, that produce different levels of noise. The noise power is found to be mainly correlated with the zigzag wavelength of the bit boundary.

1. Introduction

The observation of magnetic microstructures is very important not only in such fundamental fields as the study of magnetic domain walls but also in industrial applications such as magnetic recording and permanent magnets. The recording density is increasing rapidly, and to increase the density further, it is essential to observe detailed recorded-bit structures (magnetization distribution), particularly the boundary between the bits. Since the minimum bit length in current products has reached 250 nm, the resolution needs to be less than several tens of nanometers so as to apply to future-generation recording systems.

There are various domain-observation methods such as Lorentz microscopy,[1] electron holography,[2] differential phase contrast Lorentz microscopy,[3] Bitter method,[4] optical microscopy using Kerr effect (Kerr microscopy),[5] scanning electron microscopy using the deflection of secondary electrons near the sample surface (Type I)[6] or deflection of scattered electrons inside the sample (Type II),[7] magnetic force microscopy (MFM),[8] and so on. These methods are classified into two groups, transmission and reflection types. The former three methods (transmission type) are capable of 10-nm spatial resolution, and could meet that resolution requirement. The sample thickness, however, is restricted to below several hundreds of nanometers due to the limitation of the electron penetration depth. The resolution of the other methods, which are of the reflection type, is not as high as that of the transmission methods, although it is not necessary to thin the sample. On the other hand, there are no methods sensitive to the magnetization except Kerr microscopy.[9] However, its resolution is limited to about 200 nm. Furthermore, magnetic domain images obtained with these methods usually contains morphological contrast.

In 1984, Koike et al. developed a spin-polarized scanning electron microscopy (spin SEM),[10] in which the magnetization distribution of a sample is directly imaged by using the spin polarization of secondary electrons (see Section 2.4), and subsequently by other researchers.[11-15] This method has some excellent capabilities; high spatial resolution even in reflection type method, quantitative detection of magnetization directions, magnetic contrast independent of surface morphology. The spatial resolution of this method is expected to be less than 10 nm. Although spin SEM is therefore in principle suitable for observing the bit structures of the media, the resolution attained with our spin SEM is 200 nm and the best resolution achieved so far is about 50 nm.[12,16] These values are not high enough. Thus, the main purpose of this study is to develop a spin SEM with 20-nm resolution, whose value is comparable to those of transmission-type methods.

To apply the spin SEM for observing magnetic microstructures to its fullest potential, a data acquisition and display (DAD) system designed for the spin SEM is required to develop. In an ordinary SEM, the intensity of secondary electrons is detected with the conventional electron detector and is used as a brightness signal on a cathode ray tube (CRT). On the other hand, a spin detector used in the spin SEM detects two polarization components simultaneously during one probe-scan, which are calculated from two pairs of output signals from the spin detector (see Section 2.3). The DAD system for the spin SEM is required to calculate two polarization components and to display both components on the CRT at every step of the probe scan. Moreover, to analyze the magnetization distribution quantitatively, the offset included in a measured polarization must be corrected after the scan. Thus, two images produced by two components need to be stored in frame memories. The DAD system also needs to have a slow-speed scanning function, since the efficiency of the spin detector is much lower than that of the conventional electron detector. Besides these functions, the DAD system needs various functions such as angle representation and vector mapping of the magnetization direction. Therefore, the DAD system for the spin SEM is much different from that for the ordinary SEM.

In Chapter 2, the spin SEM with 200-nm resolution we previously developed will be generally explained. The application of the 200-nm resolution spin-SEM to observing surface Néel walls of soft ferromagnetic materials is given in Chapter 3. The detail of the DAD system is described in Chapter 4. The application of the DAD system to observing side plane domains of Fe-C/Ni-Fe/BN magnetic multilayer strips will be described in Chapter 5. In Chapter 6, the spin SEM with 20-nm resolution will be described. The application of 20-nm resolution spin-SEM to observing recorded bits of two kinds of high-density recording media, in the 50-140 kFCI (flux changes per inch) range is given in Chapter 7. Chapter 8 briefly summarizes the contents of presented in the proceeding chapters.

References

1. M. E. Hale, H. W. Fuller, and H. Rubinstein, J. Appl. Phys. **30**, 789 (1959).

2. A. Tonomura, T. Matsuda, J. Endo, T.Arii, and K. Mihama, Phys. Rev. Lett. **44**, 1430 (1980).

3. J. N. Chapmann and G. R. Morrison, J. Magn. Magn. Mater. **35**, 254 (1983).

4. L. V. Hamos and P. A. Thiessen, Z. Phys. **71**, 442 (1931).

5. H. J. Williams, F. G. Foster, and E. A. Wood, Phys. Rev. **82**, 119 (1951).

6. J. R. Banbury and W. C. Nixon, J. Sci. Instrum. **44**, 889 (1967).

7. J. Philibert and R. Tixier, Micron **1**, 174 (1969).

8. Y. Martin and H. K. Wickramasinghe, Appl. Phys. Lett. **50**, 1455 (1987).

9. J. E. Monson, *Magnetic recording handbook*, ed. by C. D. Mee and E. D. Daniel, (McGraw-Hill, New York 1990) chapter 6.

10. K. Koike and K. Hayakawa, J. Appl. Phys. **45**, 585 (1984).

11. J. Unguris, G. G. Hembree, R. J. Cellota, and D. T. Pierce, J. Magn. Magn. Mater. **54**, 1629 (1986).

12. H. P. Oepen and J. Kirschner, Phys. Rev. Lett. **62**, 819 (1989).

13. G. P. Cameron and J. H. Judy, IEEE Trans. Magn. **MAG-24**, 3063 (1988).

14. R. Allenspach, M. Stampanoni, and A. Bischof, Phys. Rev. Lett. **65**, 3344 (1990).

15. T. VanZandt, R. Browning, and M. Landolt, J. Appl. Phys. **69**, 1564 (1991).

16. G. G. Hembree, J. Unguris, R. J. Celotta, and D. T. Pierce, Scanning Microsc. Suppl. **1**, 229 (1987).

2. Spin-Polarized Scanning Electron Microscopy (spin SEM)

2.1 Polarized Electrons

An electron has a spin angular momentum, and its magnitude along an arbitrary direction i is $\hbar/2$, or $-\hbar/2$. In an electron beam, the ith polarization component of electron beam, P_i is given by

$$P_i = \frac{N_{i+} - N_{i-}}{N_{i+} + N_{i-}}, \tag{2.1}$$

where N_{i+} and N_{i-} are the numbers of electrons having the value of the spin angular momentum along the i direction, $\hbar/2$ or $-\hbar/2$. Generally, an electron beam with $\boldsymbol{P} \neq \boldsymbol{0}$ is said to be (spin-) polarized.

2.2 Spin Polarization of Secondary Electrons

In 1976 Chrobok first discovered that the secondary electrons from a ferromagnetic material EuO are polarized, and the direction of the polarization vector is antiparallel to the magnetization direction.[1] Since then, this polarization phenomenon in secondary electrons was found in other 3d-ferromagnetic materials such as Fe-based glass alloy in 1982,[2] Ni single crystal in 1984.[3]

Figure 2.1 shows the secondary-electron polarization of Fe(110) as a function of the energy of secondary electrons obtained by Kirschner et al. in 1992.[4] At energies above 15 eV, the polarization is almost constant and its magnitude is about 28%, which is about the same as the d-band polarization. With decreasing energy, the polarization increases and reaches a

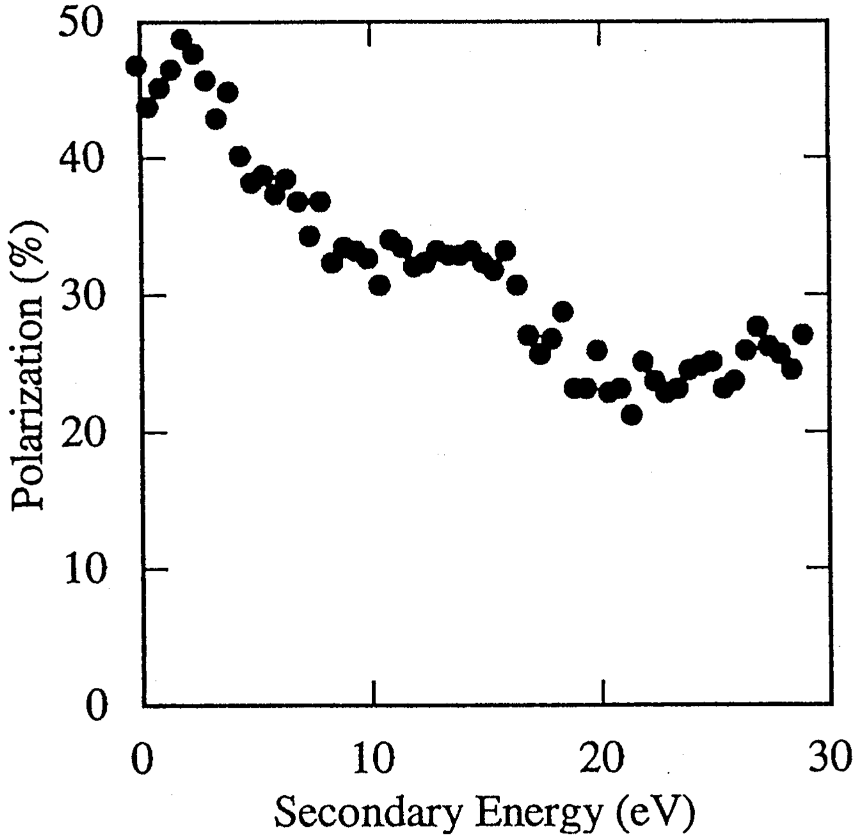

Fig. 2.1. Secondary-electron polarization as a function of the energy of secondary energy. [after J. Kirschner et al. in 1992[4]]

maximum of 45% near zero energy. These polarization behaviors are common to the other 3d-ferromagnetic materials, and can be qualitatively understood by excitations of d-band electrons and spin-dependent inelastic scattering.

When the probe electrons are injected into a sample, they predominantly excite 3d-electrons maintaining their d-band polarization. Some of the excited electrons are directly emitted from the sample, and others also excite 3d-electrons. The polarization of the directly excited electrons is almost the same as d-band polarization. On the other hand, electrons excited through the cascade process lose their energy on average and in the process of spin-dependent inelastic scattering enhances their polarization. Therefore, the polarization of secondary electrons retains the d-band polarization in their high-energy range, and increases with decreasing electron energy.

These processes produce secondary electrons with polarization vector parallel to that of electrons in the d-band. This means that the spin polarization vector of secondary electrons in the d-band is antiparallel to the magnetization vector, because, in the case of an electron with a negative charge, the spin angular momentum is antiparallel to the magnetic dipole moment and spin polarization is defined in terms of spin angular momentum as is seen Eq. (2.1).

As described above, the magnetization is not able to be determined quantitatively by the polarization of secondary electrons due to the polarization enhancement with decreasing the secondary energy. This enhancement is, however, favorable to producing the domain image.

2.3 Spin Detector

There are four different kinds of spin detectors used in spin SEM; Mott,[5] defuse scattering,[6] polarized low energy electron diffraction,[7] and absorbed current detectors.[8] We use the Mott detector for polarization analysis.

Figure 2.2 shows the basic principle of the Mott detector. When high-energy polarized electrons hit a Au foil target and are elasticity scattered at the target, the electrons scattered into two symmetrical left and right directions are detected by a pair of electron detectors. Both

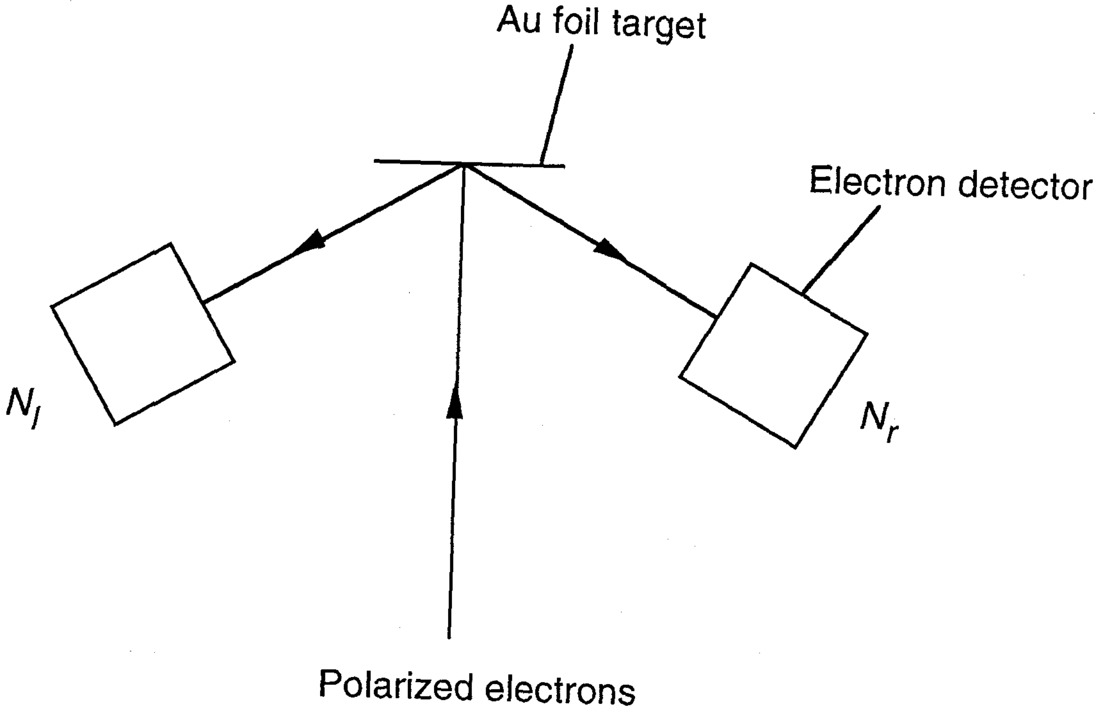

Fig. 2.2. Basic principle of the Mott detector.

scattering intensities are not the same due to the spin-orbit interaction between the fast electron and the Au atom. When the numbers of scattered electrons are defined as N_l and N_r, one polarization component normal to the scattering plane, P_i, is determined by

$$P_i = \frac{1}{S}\frac{N_l - N_r}{N_l + N_r}, \tag{2.2}$$

where S is a Sherman function determined only by the scattering condition. Another polarization component is detected by another pair of electron detectors located at the positions rotated 90° about the incident beam direction (not shown in Fig. 2.2).

The polarized electrons are ordinary accelerated to around 100 keV, since the spin orbit interaction increases with the energy of the polarized electrons. In this case, the Sherman function has a maximum at the scattering angles from the electron incident direction of around ±120°.[9]

Scattered electrons are ordinarily counted one by one with a pair of electron detectors, where the error of the measured polarization is mainly determined by the statistical error of the electron counts. The statistical error, δP_i, is given by

$$\delta P_i = \sqrt{\frac{1}{N}\left(\frac{1}{S^2} - P_i^2\right)}, \tag{2.3}$$

where $N=N_l + N_r$. Since $P_i \leq 1$ and $S \leq 0.3$ for a general polarization detector, $1/S^2 \gg P_i^2$ so that Eq. (2.3) becomes

$$\begin{aligned} \delta P_i &= \frac{1}{\sqrt{S^2 N}} \\ &= \frac{1}{\sqrt{\xi S^2 N_o}}, \end{aligned} \tag{2.4}$$

where N_o is the total number of electrons injected into the target, and $\xi = N/N_o$. Eq. (2.4) indicates that the statistical error, δP_i, becomes smaller as ξS^2 increases. Thus, ξS^2 quantitatively represents the efficiency of the Mott detector. This value is written as

$$F = \xi S^2 , \tag{2.5}$$

and is used as a figure of merit for the Mott detector.[4]

Using (2.4) and (2.5), the signal-to-noise ratio S/N of the Mott detector is roughly estimated by

$$\frac{S}{N} \approx \frac{P_i}{\delta P_i} \approx \sqrt{F N_o} . \tag{2.6}$$

The S/N of the ordinary electron detector used in SEM is written as

$$\frac{S}{N} \approx \frac{N_o}{\delta N_o} \approx \sqrt{N_o} . \tag{2.7}$$

From (2.6) and (2.7) the Mott detector needs F times as many secondary electrons as the ordinary electron detector to produce the same S/N image. Since F is 6 x 10^{-6} in our Mott detector, its efficiency is about 10^{-5} as high as that of the ordinary electron detector.

2.4 Spin-Polarized Scanning Electron Microscopy

The schematic diagram of our spin SEM is shown in Fig. 2.3. The spin SEM system mainly consists of an electron gun with an objective lens, a Mott detector, a secondary collector and transport optics, an ion gun, a sample chamber, a signal processor, and a display. But the sample chamber is not shown in the figure. The Mott detector used, whose size is 800 mm in length and 370 mm in diameter, is attached to the chamber vertically, and the electron gun

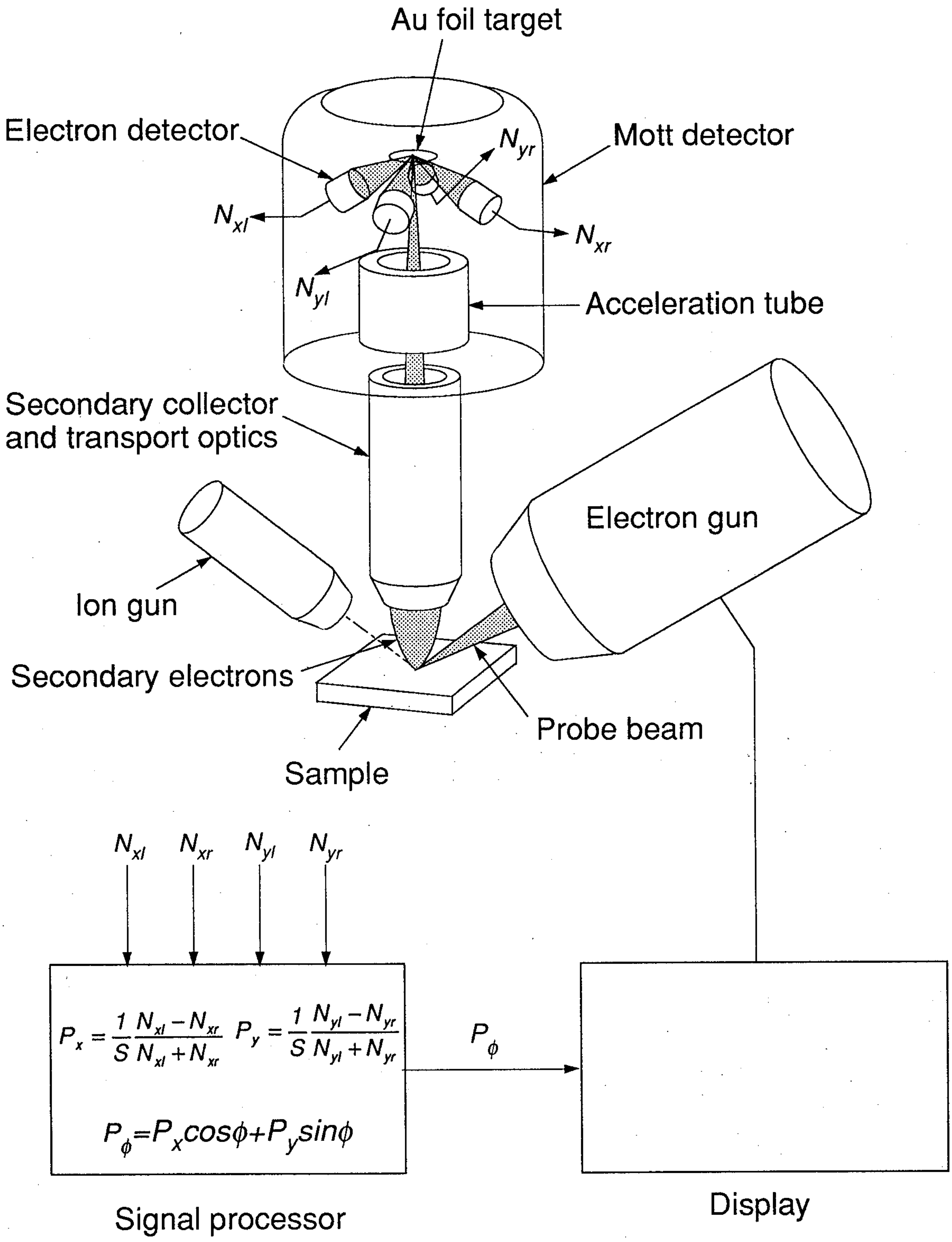

Fig. 2.3. Schematic diagram of the spin SEM.

is placed on its optical axis at a 60° slant towards the horizontal line from the vertical direction. The ion gun is used for sample surface cleaning before domain observation.

When the probe electron beam generated from the electron gun is focused onto the sample surface with the objective lens, secondary electrons are emitted from the probe-beam injection-point on the sample. These secondary electrons are collected with the secondary collector, and are led to the Mott detector through the transport optics. With the Mott detector, independent two components, P_x and P_y, of the polarization vector parallel to the sample surface are detected. Two detected signals are input to the signal processor, where an arbitrary polarization-component, P_ϕ, parallel to the sample is calculated from P_x and P_y. The signal of the P_ϕ component is used as a cathode ray tube (CRT) brightness signal in the display. The sample surface is raster-scanned with the probe beam, and synchronized with its raster scanning, the P_ϕ polarization component is imaged on the CRT.

Therefore, the magnification of the obtained image is determined by the ratio between the probe-scanning area on the sample and the domain-display area on the CRT, and the spatial resolution is mainly determined by the probe beam diameter. Since the technology to get a fine probe is still developing in the field of SEM, we can expect high-spatial resolution with spin SEM. However, our spin SEM had a resolution of 200 nm.[10]

In addition to high spatial resolution, the spin SEM has some excellent capabilities such as morphology-independent detection. The morphology-independent detection capability is unique and important, especially for investigating the magnetic microstructure of a three-dimensional (3-D) sample, as other methods do not have similar capabilities. Secondary electron intensity generally varies according to the surface morphology. In spin SEM, the polarization of secondary electrons has the value of (N_l-N_r) normalized by (N_l+N_r). Since (N_l+N_r) is proportional to the secondary electron intensity, polarization is independent of the secondary electron intensity.

Since the probing depth of this method is about 1 nm,[11] it is necessary to remove the adsorbed layer on the sample surface before the domain observation. Ion sputtering using the ion gun and to maintain ultra-high-vacuum in the sample chamber are needed. The vacuum pressure of our chamber is usually 10^{-10} Torr.

References

1. G. Chrobok and M. Hofmann, Phys. Lett. **57A**, 257 (1976).
2. J. Unguris, D. T. Pierce, A. Galejs, and R. J. Cellota, Phys. Rev. Lett. **49**, 72 (1982).
3. H. Hopster, R. Raue, and E. Kisker, Phys. Rev. Lett. **50**, 70 (1983).
4. J. Kirschner and K. Koike, Surf. Sci. **273**, 147 (1992).
5. K. Koike and K. Hayakawa, Jpn. J. Appl. Phys. **23**, L187 (1984).
6. J. Unguris, D. T. Pierce, and R. J. Cellota, Rev. Sci. Instrum. **57**, 1314 (1986).
7. J. Kirschner and R. Feder, Phys. Rev. Lett. **42**, 1008 (1979).
8. K. Koike, H. Matsuyama, and K. Hayakawa, Jpn. J. Appl. Phys. **27**, L1352 (1988).
9. J. Kessler, *Polarized electrons*, (Springer, Berlin, Heidelberg 1976).
10. K. Koike, H. Matsuyama, H. Todokoro, and K. Hayakawa, Jpn. J. Appl. Phys. **24**, L833 (1985).
11. K.Koike and J. Kirschner, J. Phys. D: Appl. Phys. **25**, 1139 (1992).

3. Application of Spin SEM

— Surface Néel Wall Observation —

3.1 Introduction

Hubert and LaBonte independently proposed a two-dimensional wall model instead of conventional Bloch or Néel walls.[1,2] They performed two-dimensional computations for magnetic wall structures in films on the basis of a stray-field-free configuration; 180° domain walls are Néel-like near the surface and Bloch-like in the middle of films. In addition, the wall structure is asymmetric with respect to the wall plane and the width is much larger than the one-dimensional estimate. Hubert generalized this model for thicker films, and predicted the surface Néel wall width quantitatively as a function of film thickness.[3]

The asymmetric wall structure was first observed experimentally by S. Tsukahara and H. Kawakatsu[4] and subsequently by other researchers,[5,6] all using transmission electron microscopes; the information obtained was for wall structures averaged over the film thickness that was limited to below a few hundred nanometers for electron beam transmission.

In this Chapter, the first observations of Néel walls near the surface of 1-μm-thick CoTaZr amorphous film[7] and 0.2, 1.4, and 2.0-μm-thick permalloy films were made.[8] Moreover, the Néel wall widths of these permalloy samples were quantitatively measured.[8]

3.2 Experimental

The spin SEM can be operated either in image mode or line-scan mode. In the former mode the image is obtained using any spin-polarization component as image brightness. In the latter mode two components P_x, P_y are measured by scanning a probe electron beam along a line on the sample and they are recorded in digital memories for subsequently calculating magnetization distribution.

CoTaZr (92 at% Co, 5 at% Ta, 3 at% Zr) amorphous film was made by sputtering onto a titanium substrate to form a stripe pattern. The width of each stripe was 15 μm. Permalloy polycrystalline films, 0.2, 1.4 and 2.0 μm thick, were deposited on glass substrates by the sputtering method to form rectangles and patterns of thin-film heads for magnetic recording. The exposed part of the substrates was covered with Cu to avoid the charge build up during observation.

Observations were made for the pressure range from 10^{-8} to 10^{-9} Torr after cleaning by Ar ion bombardment. A field-emission type electron gun was operated at an acceleration voltage of 6 kV and total emission current of typically 50 μA. Electron count rate according to the Mott detector was some 10^5 counts per second. In image mode, total time to form an image frame was about 10 minutes. In line-scan mode, dwell time for one point on the sample was set at 1 second. Polarizations were obtained as the average of four repeated line-scans.

Error due to the instrumental asymmetry of the Mott detector was corrected on the assumption that magnetizations on both sides of the wall are parallel to the surface and antiparallel to each other. The error bars shown later were derived only from statistical estimates.

3.3 Results and Discussion

Fig. 3.1 shows the domain images of CoTaZr amorphous film. The polarization detection direction is indicated by the arrow at the top of the figure. Part of the area in Fig. 3.1(a) is magnified in Fig. 3.1(b). The arrows in Fig. 3.1(b) show magnetization directions assumed from image contrast. The sample has closure domain structure and their inner parts are separated by 180° walls. Furthermore, 180° walls show Néel-type image contrast, whose width is about 1 μm. This value is very large compared with that calculated from the one-dimensional wall model, which predicts a width of about 60 nm.

To measure the wall width quantitatively as a function of the film thickness, the 0.2, 1.4, and 2.0-μm-thick permalloy films were observed in both image and line-scan modes. Fig. 3.2

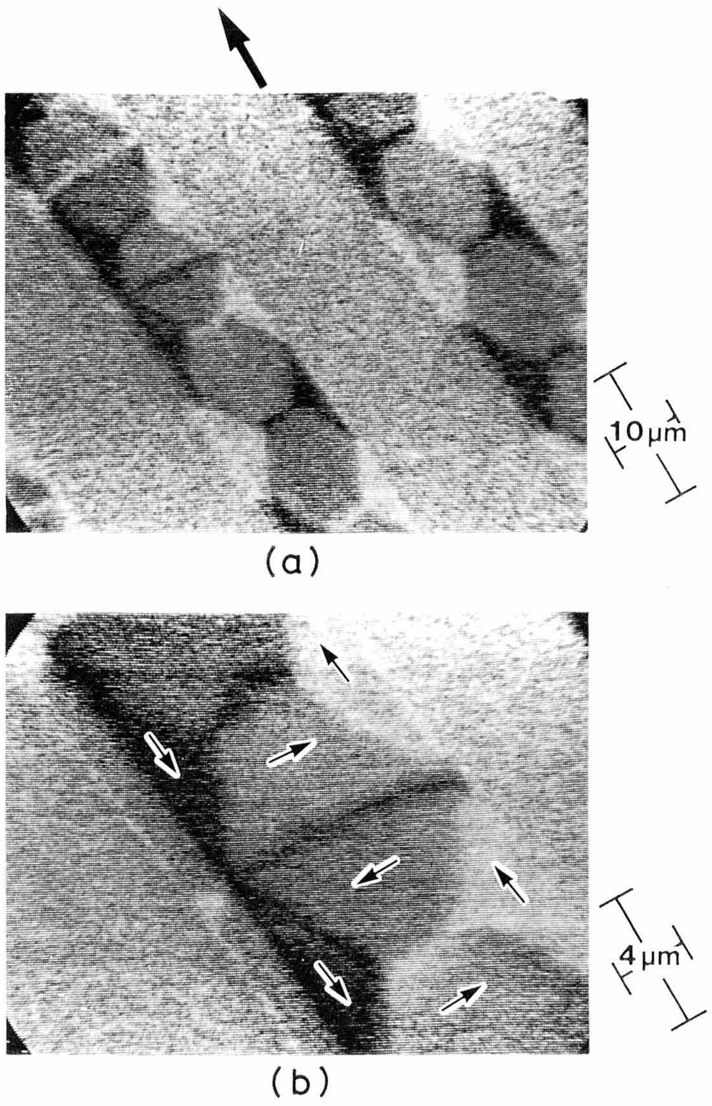

Fig. 3.1. Domain images of 1-μm-thick CoTaZr amorphous film. Part of the image (a) is magnified in (b).[7]

shows domain images of 0.2, 1.4, and 2.0-μm-thick films with polarization detection direction indicated by the top arrow. Smaller arrows in the pictures show magnetization direction. As with CoTaZr sample, these films as a whole have closure domain structures and their inner parts are separated by the Néel-type walls. The width of the Néel-type wall increases with film thickness.

High-magnification domain images of the 180° wall in the 1.4-μm-thick film are shown in Fig. 3.3. Polarization detection directions of images (a) and (b) were perpendicular to and parallel to a wall, respectively. Polarization components P_x, P_y along a straight line in Fig. 3.3 were recorded. The data are shown in Fig. 3.4(a), and the rotation angle θ calculated from these data is shown in Fig. 3.4(b). Néel wall width W_s here is 0.84 μm. The wall widths of 0.2 and 2.0-μm-thick samples are also determined in the same way, and the wall width W_s against film thickness D is shown in Fig. 3.5. The solid line shows the result of the Hubert model. The wall widths measured are larger than those calculated by one-dimensional estimate, and the widths of 0.2 and 1.4-μm-thick samples are comparatively consistent with the result of the Hubert model. However, the wall width of the 2.0-μm-thick sample is much larger than that of the Hubert model. The magnetizations of 2.0-μm-thick sample fluctuate more than those of 0.2 and 1.4-μm-thick samples judging from the magnetic contrast of Fig. 3.5. This might be a cause of widening the wall.

3.4 Conclusions

Néel walls have been observed on the surface of both 1-μm-thick CoTaZr amorphous film and 0.2, 1.4, and 2.0-μm-thick permalloy films. The magnetization rotation angle across the Néel wall was calculated from the in-plane polarization components P_x and P_y detected by the spin SEM, by which the Néel-wall widths were quantitatively determined. At all thickness ranges, these wall widths are larger than those calculated from the one-dimensional wall model. The wall widths of 0.2 and 1.4-μm-thick samples are comparatively consistent with the result of the two-dimensional wall model predicted by Hubert, although the width of the 2.0-μm-thick

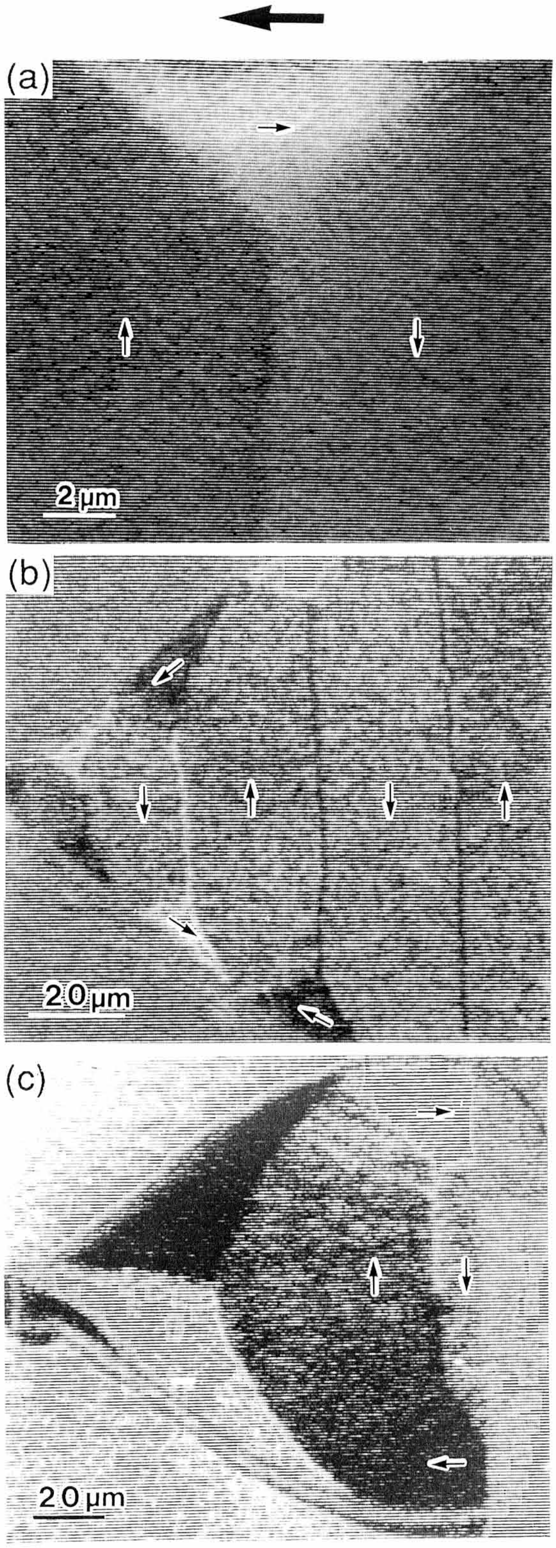

Fig. 3.2. Images of magnetic domains in permalloy films: thickness is 0.2, 0.4, and 2.0 µm for (a), (b), and (c), respectively. The arrow at the top shows the direction of polarization detection and the arrows in each picture indicate magnetization direction.[8]

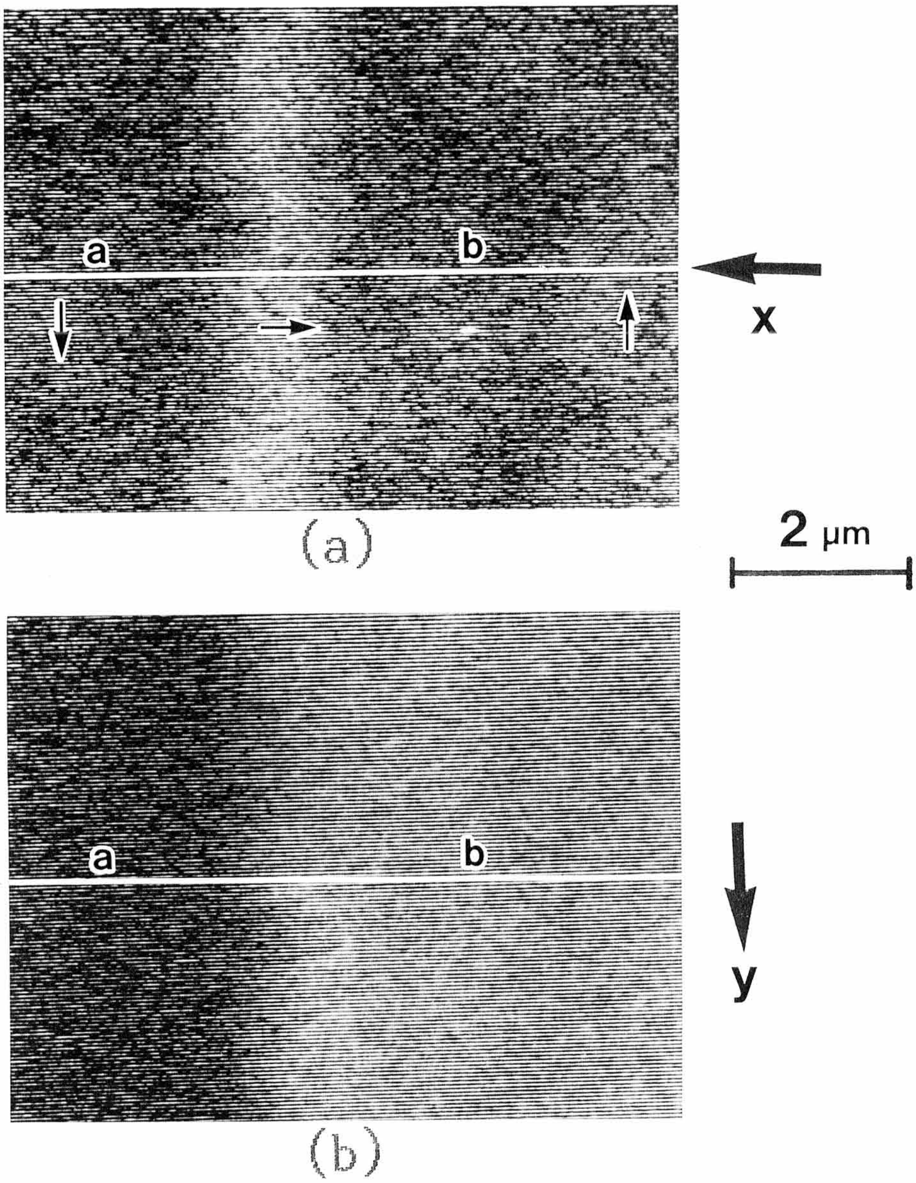

(a)

(b)

Fig. 3.3. High-magnification images of 1.4 μm-thick permalloy film. Polarization detection direction is indicated by an arrow on the right side; i.e. along x-axis (a) and y-axis (b).[8]

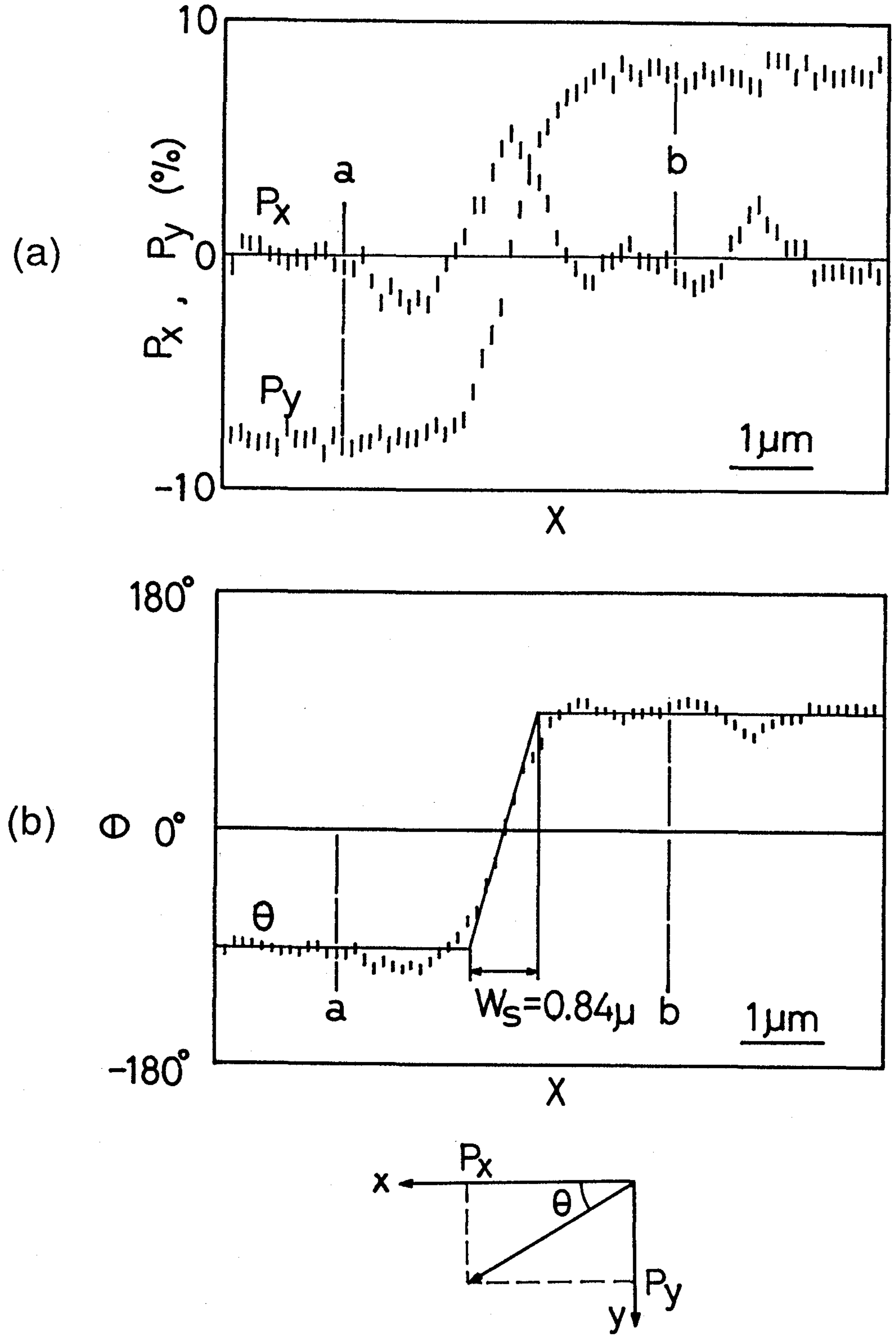

Fig. 3.4. Spin polarization components P_x, P_y derived from the data in Fig. 3.3: (a) and its rotation angle $\theta=\tan^{-1}(P_y/P_x)$: (b).[8]

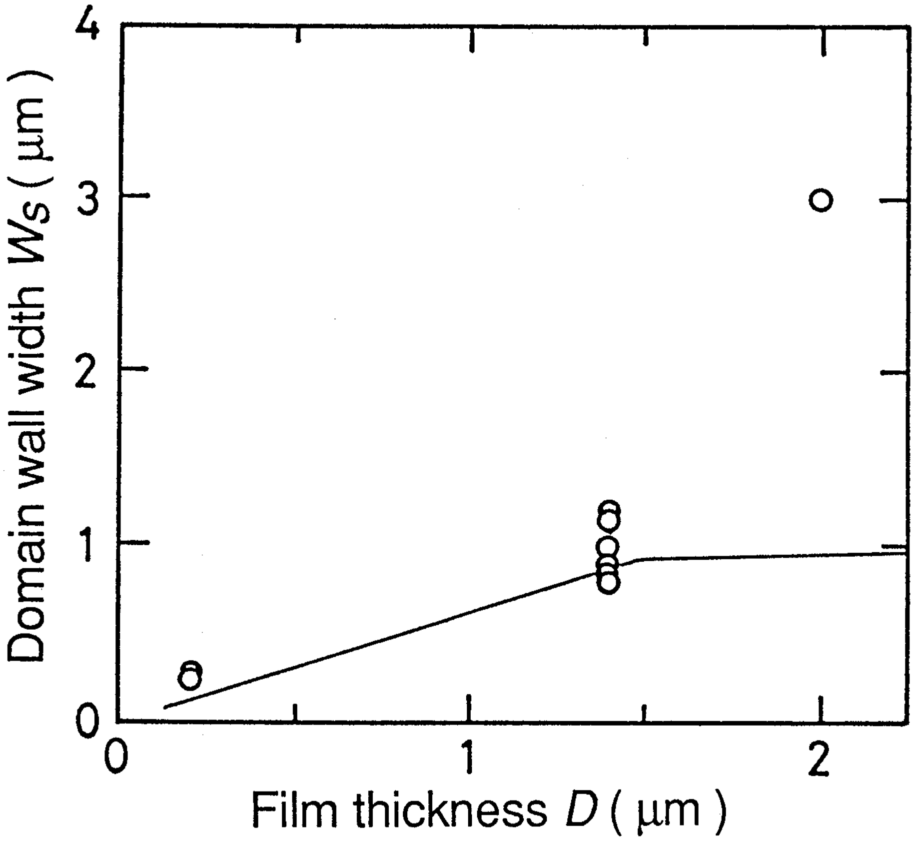

Fig. 3.5. Domain wall width against film thickness. The solid line is the result predicted by Hubert's stray-field-free magnetization configuration model.[8]

sample is much larger than that of the Hubert model.

References

1. A. Hubert, Phys. Stat. Sol. **32**, 519 (1969).

2. A. E. LaBonte, J. Appl. Phys. **40**, 2450 (1969).

3. A. Hubert, Z. angew. Phys. **32**, 58 (1971).

4. S. Tsukahara and H. Kawakatsu, J. Phys. Soc. Jpn. **32**, 1493 (1972).

5. D. C. Hothersall, Phys. Stat. Sol. **51**, 529 (1972).

6. T. Suzuki and K. Suzuki, Jpn. J. Appl. Phys. **15**, 707 (1976).

7. K. Koike, H. Matsuyama, K. Hayakawa, K. Mitsuoka, S. Narishige, Y. Sugita, K. Shiiki, and C. Saka, Appl. Phys. Lett. **49**, 980 (1986).

8. H. Matsuyama, K. Koike, K. Hayakawa, K. Mitsuoka, S. Sudo, S. Narishige, and Y. Sugita, IEEE Trans. Magn. **MAG-23**, 2173 (1987).

4. Data Acquisition and Display System (DAD System)

4.1 Introduction

Two-dimensional quantitative measurements of magnetization directions have already been achieved on metallic glasses using digitally enhanced Kerr microscopy[1]. The distribution of magnetization directions on the sample is displayed by arrows, and additionally, with the help of a color code. However, since the magnetic signal is comparable to or smaller than the morphological signal, this measurement requires an image-contrast normalization process that includes magnetically saturating the sample. In this process, the magnetic structure is destroyed during the measurement. However, since the magnetic signal obtained by spin SEM is almost independent of surface morphology, two components of the magnetization can be measured quantitatively without morphology correction, i.e., without the magnetic structure destruction found in Kerr microscopy.

The capability of morphology-independent detection is unique and important, especially for investigating the magnetic microstructure of a three-dimensional (3-D) sample, as other methods do not have similar capabilities (see Section 2.4).

As opposed to conventional SEM electron detectors, a serious and specific problem common to spin detectors are their low efficiency in detecting image signal:[2-4] typically, it takes more than 10 min to form a fine 250 x 256 pixel image at 3 nA probe current. In addition, the measured polarization generally includes offsets that must be corrected, especially in quantitative analysis.

Due to the above-mentioned drawbacks of spin detectors, the excellent capabilities of spin SEM are not used to their fullest potential. For two-dimensional vector mapping, a much longer image acquisition time is necessary for high-precision vector direction measurement. Additionally, offset included in a measured polarization must be corrected. This is quite a complex task if the offset is dependent on the image position. A morphology-independent magnetic image of an Fe sample having very small grooves with depth of around 1 μm has been reported.[5] For samples with much larger morphology or 3-D shapes, there would be some areas where secondary electron emission is reduced. To attain a high image quality for those areas, extended image acquisition time is needed. On the other hand, a large probe current and large image-acquisition time cause sample surface contamination, reducing the intrinsic polarization signal. Furthermore, many scanning trials are required to determine an appropriate observing area on the sample before obtaining the high-quality image. Therefore,we must reduce the time for determining the observing area as much as possible.

To meet the requirements of processing plural signals from the spin detector, to erase the intrinsic problem, and to utilize the excellent capabilities of spin SEM, the data-acquisition and display (DAD) system must be equipped with many new functions.

As stated in Section 2.4, the DAD system developed by Hitachi was composed of the modified commercial-SEM display system and the analog signal processor;[6] the latter computed the polarization component P_ϕ along an arbitrary but fixed direction, ϕ, from the Mott detector signals by applying the coordinate rotation formula to P_x and P_y. However, in spite of simultaneous detection of two independent components P_x and P_y, only one P_ϕ image was recorded on a photograph during each scan.

Spin SEM developed by the National Institute of Standards and Technology adopted an improved display system with a computer, although the detailed functioning has not been published yet.[7] Briefly, with the display system, three 256 x 192 pixel images of P_x, P_y, and intensity N proportional to secondary electron intensity are obtained simultaneously and stored in the computer at some 10 ms/pixel. Thus, magnetic and surface-topographic information are obtained in one scan. It is possible to obtain another component P_z image with an additional spin detector placed orthogonally to the detector for P_x and P_y.

In this Chapter, the DAD system will be described in detail, including practical applications to a bulk magnetic recording head and a multilayered film which is expected to be used in future generation magnetic recording system for main frame computers.[8]

4.2 Function of System

The system has the following functions: high-speed scanning (with some loss of image quality) for quick search; repetitive scanning and magnified scanning for easy operation; variable-speed scanning for high-quality imaging even for a 3-D sample; on-line digital computing and recording of two polarization components, P_x and P_y, with signals from the spin detector; displaying the magnetization distribution as superimposed arrows on magnetic images or an ordinary SEM image after correcting offsets caused by instrumental asymmetries; and angle representation of the magnetization direction. Finally, a frame memory enabling real-time observation even for very slow scanning is provided.

We adopted a 256 gray scale, which is enough to be viewed continuously with a black-and-white image. The pixel number can vary from 64 x 64, 128 x 128, 256 x 256, and 512 x 512.

Scan speed

The scan speed can be set from 50 μs/pixel to 50.12 ms/pixel with 50 μs step and from 50 ms/pixel to 10.23 s/pixel with 10 ms step. The maximum speed, 50 μs/pixel (21 s/512 x 512 pixel image, 5.2 s/256 x 256 pixel image, 1.3 s/128 x 128 pixel image, 0.4 s/64 x 64 pixel image) was determined under the condition of signal-noise-ratio $S/N=1$ for an Fe sample with an electron probe energy of 5 keV and a probe current of 3 nA. In fact, our preliminary experiments indicated that the outline of the domains can be identified even at $S/N=1$. In this case, the image acquisition time is one to two orders of magnitude as fast as that for a high quality image. A much slower-speed scanning is available for high S/N image. A variety of pixel number and scan-speed choices enables observers to obtain images to suit their observation purpose.

Constant and variable-speed scanning

The sample can be scanned at constant speed or variable speed. The constant-speed scanning has a single-scanning mode like that of conventional SEM, and a multiscanning mode. In the latter mode, an image is obtained by repetitive scanning and polarization averaging, where the number of repetitions can be selected and preset from 2 to 999. The average polarization $\overline{P_{in}}$ (i=x or y) at the nth time repetitive scanning is calculated with the following function, and is stored in the frame memory:

$$\overline{P_{in}} = \frac{1}{n}\left\{(n-1)\overline{P_{in-1}} + P_{in}\right\} \qquad (n \geq 2).$$

Here, P_{in} is the polarization obtained at the nth time scanning, and $\overline{P_{i1}}=P_{i1}$ Of course, the user can stop the scanning at any time. This function is very convenient for investigating samples with unknown magnetization distribution as the user is unable to preset the appropriate parameters, i.e., the scan speed and the pixel number, before scanning.

If a sample has areas where secondary electron intensity decreases, then the statistical noise increases. To obtain low noise images for such areas at constant speed scanning, we have to lengthen the time for every pixel, which results in increased image-acquisition time. In this case, variable speed scanning is very valuable for saving time. In this scanning mode, the secondary electron intensity is fed back to the scan speed in real time, so that the detected electron number is constant for each pixel. Thus, a higher quality image can be obtained in a shorter time. This mode is especially useful for observing a sample having a three-dimensional surface structure, as the secondary intensity varies depending on surface orientation.

Rescanning

This system has a function in which 1/2, 1/4, or 1/8 of the image may be magnified onto the full monitor screen. The magnification is done by displaying image data corresponding to the area to be magnified in a frame memory on the monitor. In this function, however, the pixel number of magnified-image decreases. To avoid the decrease in pixel number, it is also possible to rescan any part of the preobserved area with any scanning mode. The area can be specified on the preobserved image with an acquisition square frame of 1/2, 1/4, or 1/8 of the preobserved image. As a result, a magnified image of x 2, x 4, or x 8 of the original image can be obtained with any pixel number. The same function can be obtained by the combination of image shift and magnification of the conventional SEM display. However, these operations are troublesome and time consuming, as it is not easy to determine the area one wants to observe. This rescan function is especially convenient for viewing many magnified images of different positions in a prescanning area.

Data storage

All data obtained during the scanning, including the four outputs of the Mott detector and a sample-absorbed current, I_s, are temporarily recorded in frame memories in parallel for quantitative analysis and image processing. After scanning, the data stored in the memories can be recorded on a hard disk, a floppy disk, or a magneto-optical disk to permanently preserve the data.

From the data obtained with the Mott detector, the system calculates polarization vector components P_x and P_y, magnitude P, and angle ϕ of the polarization vector component in the x-y plane as follows:

$$P = \sqrt{P_x^2 + P_y^2},$$

$$\phi = \tan^{-1}\left(\frac{P_x}{P_y}\right).$$

P is related to the magnitude of the magnetization vector component in the x-y plane, and $\phi+\pi$ is the direction of the magnetization vector component in the x-y plane. These values represent magnetization-direction distribution.

Correcting measured polarization

A major problem when calculating P and ϕ is that the measured polarization components generally contain offsets due to instrumental asymmetries. In the Mott detector, these are generally caused by the mechanical asymmetry of the scattering system, and the deviation from geometrical symmetry of electron injection position and angle into the Au foil target. Since an image on the back focal plane of an extraction lens for secondary electron collection is focused on the target in the Mott detector, the electron injection position is constant and independent of the secondary emitting position on the sample. In addition, the angle of injection to the Au foil target is almost constant, since secondary electrons are accelerated to an energy of 100 keV. Therefore, offsets due to asymmetries are almost constant all over the observation area, which is, however, restricted to about 1 mm^2 by the electron collection area of the secondary collector. If there is a nonmagentic part in the observation area, the offset for every pixel equals the observed apparent polarization in the nonmagnetic area, and the measured polarization can be corrected by subtracting the value in the nonmagnetic area from the whole image data.

Another method for correcting the offsets is as follows. If the magnetization vectors of the flat surface lie in the surface plane, as with soft magnetic materials, one can determine offsets so that the corrected P is the same for all areas with the same materials.

Representation of magnetization direction

The system can represent magnetization-direction distribution in three ways. One is vector mapping similar to that performed in Kerr microscopy.[1] Here, magnetization vectors of the sampling points are represented by arrows where the direction is parallel to the magnetization direction and the length is proportional to the magnitude of the polarization vector. The position of the sampling points can be on the square mesh where size can be arbitrarily specified, or it can be on any point specified by marking the image with a mouse. The magnetization direction of the sampling points can be calculated by using data of a specified pixel or by using data from 3 x 3 to 9 x 9 pixels around the specified point for reducing statistical noise. Second, using a vector angle as the image's black and white brightness signal, where there is one-to-one correspondence between the gray level and magnetization direction of each pixel. 256 gray levels are used for image representation. Finally, colors are used to represent vector angles as performed in Kerr microscopy,[1] or in spin SEM.[9] Here, one-to-one correspondence is maintained between the color and magnetization direction of each pixel. Again, the number of colors prepared for representation is 256. Each of the above characteristics will be discussed in detail later.

Real-time observation

For real-time observation, the interval between the beginning of the data acquisition for one pixel and its display is within three times the pixel dwell time (minimum 150 μs). The dead time of data acquisition, during which no signal is collected, is constant and less than several hundred nanoseconds at every scanning speed. Moreover, the stored image data are constantly read out and displayed on the monitor. The real-time image is obtained only after the 150 μs delay from the scanning. However, all output signals of the Mott detector, which are not displayed on the monitor in real time, are transferred to the frame memories after each line scan. Approximately 10 ms is required to transfer these outputs. For instance, it takes 21 s to get an image at the 512 x 512 pixel scanning of 50 μs/pixel.

4.3 Apparatus

Our Mott detector consists of a secondary electron collector, a transport optics, a 100 kV accelerator, a Au foil target, and four electron detectors (Si surface barrier detectors) placed at four symmetrical positions around the secondary electron path (see Chapter 2). One electron striking the electron detector produces an electric pulse signal which is transmitted to the DAD system.

The schematic diagram of the DAD system is illustrated in Fig. 4.1. The DAD system is divided into two units, the input/output (I/O) unit and the image processing unit. The I/O unit consists of 12 pulse counters (16 bit) for the output signals of the Mott detector, an analog-to-digital (AD) converter (8 bit) for the absorbed current, I_s, and a scan controller including two digital-to-analog (DA) converters (12 bit). We used a modified NIRECO Luzex III as the image processing unit. It consists of a personal computer having a 16-bit central processing unit with a 20 MB hard disk, two 1 MB floppy disks, and a 594 MB magneto-optical disk; an image processor containing two digital signal processors (DSPs) for high-speed calculation; 32 frame memories of 512 x 512 x 16 bit ; an printer; and a 19 inch color monitor (1280 x 1024 pixels). All except the monitor and the image printer are connected to frame memories.

A user can control all processes from scanning to image display and data storage by using the computer. To reduce the observer's burden, most operation can be done using computer mouse with pull down menu.

I/O unit

The I/O unit controls the scanning and acquires output signals from the Mott detector. The scan controller sends voltage signals from DA converters to two analog circuits. These circuits in the commercial SEM display supply current to deflection coils of an electron gun for the scanning of x and y directions. In order to obtain a 512 x 512 pixel image at up to 8 times magnification of the part of the prescanning 512 x 512 pixel area, the output-voltage resolution of the DA converter must be 8 times larger than 512, i.e., 4096 (12 bit). Output-voltage response time also must be much less than one pixel time (minimum 50 μs), and is actually about 0.8 μs, which is 1.6 % of 50 μs. To avoid electric interference between the DAD system and the analog circuits (since the analog circuit generates very small current with high precision), an optical-isolation amplifier is attached to each DA converter.

The number of output pulses from the Mott detector during each pixel time are added up with four pulse counters, whose counts are outputted to the system bus as 16-bit digital signals at the end of every pixel time. Although four counters are sufficient to detect P_x and P_y components, we have prepared a pair of counters for another component P_z, as well as an additional three pairs of counters for the use of real-time offset collection for use in the near future. The P_z component would be measured by a second Mott scattering system with 100 kV spin rotation equipment placed beyond the first system for P_x and P_y. This would be possible because in the Mott detector, secondary electrons accelerated to 100 keV almost pass through the Au foil target, conserving their spin state. Real-time offset correction would be able to use forward scattered electrons in the detector.[10] The electron polarization does not affect the forward scattering intensity around ±45° from the incident electron direction. Therefore, the detected asymmetry in this geometry is due to instrumental asymmetry, which could be used for the correction.

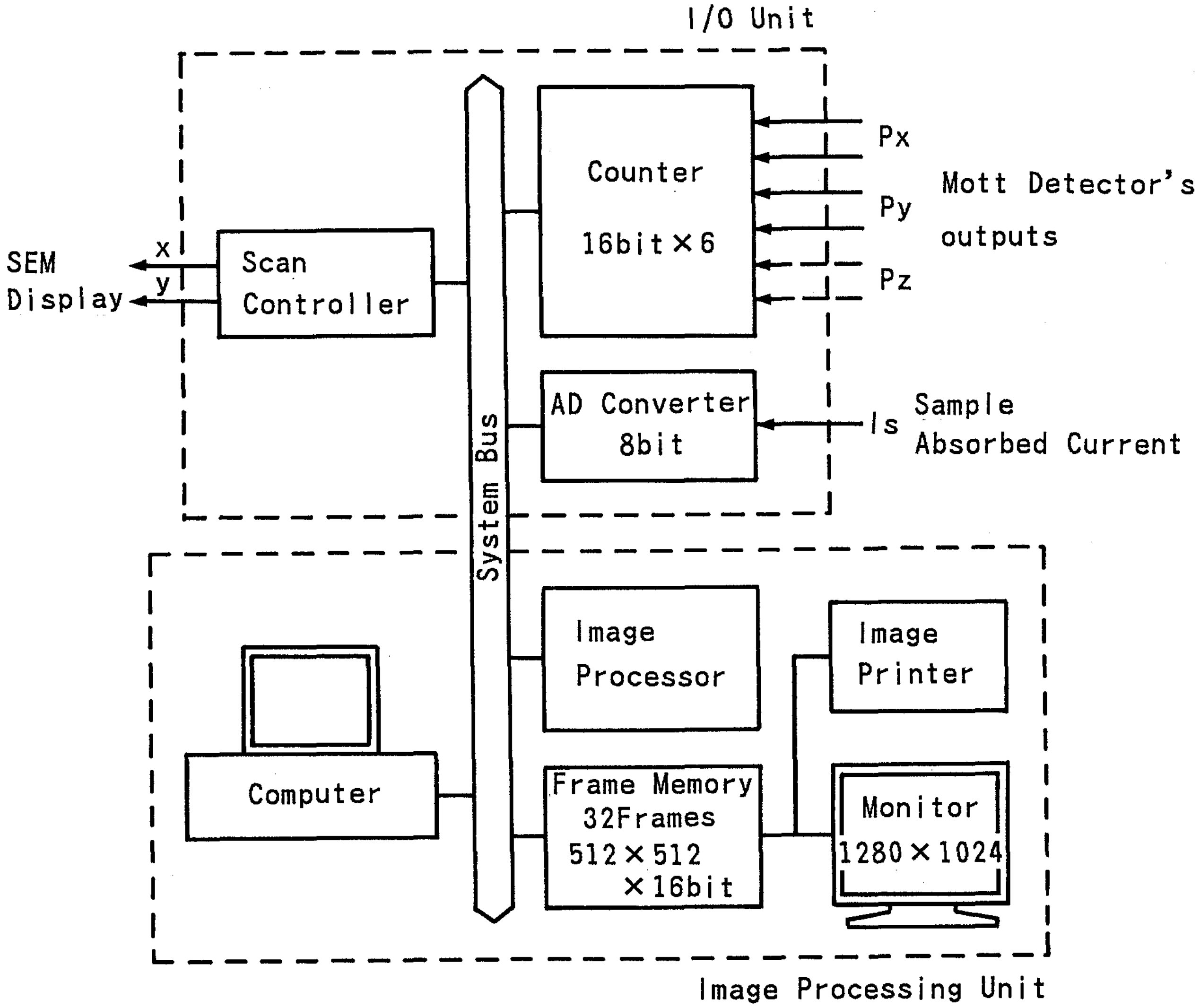

Fig. 4.1. Block diagram of a data-acquisition and display system.[8]

Image processing unit

The resister length of the counter is 16 bits. This digital data is easy handled by the computer, and the statistical uncertainty of a polarization can be reduced to less than a few percent. Each counter can go up to 2^{16} (65536), and the polarization component is computed as a 16 bit digital signal by the DSP. Inside the DSP the polarization is computed to expand the 16 bit data into 32 bit data to maintain the data accuracy. The minimum uncertainty of polarization is less than 1% using our Mott detector. With the AD converter, a sample absorbed current, I_s, is converted to an 8 bit (256) digital signal, which is outputted to the system bus. We determined the bit length of the AD converter from the 256 gray scale.

Polarization components of P_x and P_y are calculated from two pairs of counter outputs within 50 μs by one DSP, then outputted to another DSP. P_x, P_y, I_s, and the sum N of four counters' outputs, which is proportional to secondary electron intensity, are stored in the frame memories. Images of P_x, P_y, and I_s (or N) are simultaneously displayed on the 1280 x 1024 pixel monitor within 50 μs by using another DSP. In the multiscanning mode, the averaging between each component obtained by the present scanning and corresponding stored component obtained by the last scanning is also performed with the former DSP.

The DAD system also has general image processing functions such as smoothing, addition and subtraction between the images, many kinds of filtering, magnification, rotation, and fast Fourier transformation.

4.4 Results and Discussion

The following domain observations were made under a base pressure of 3×10^{-10} Torr after sample surface cleaning by Ar-ion bombardment (2 kV, 12 μA) for 10 min. A thermal assisted field-emission electron gun operated at a probe energy of 4 ~ 5 keV and a typical probe current of 3 nA. In this case, the probe diameter was less than 0.1 μm. The incident angle of the probe was 60° from sample surface normal.

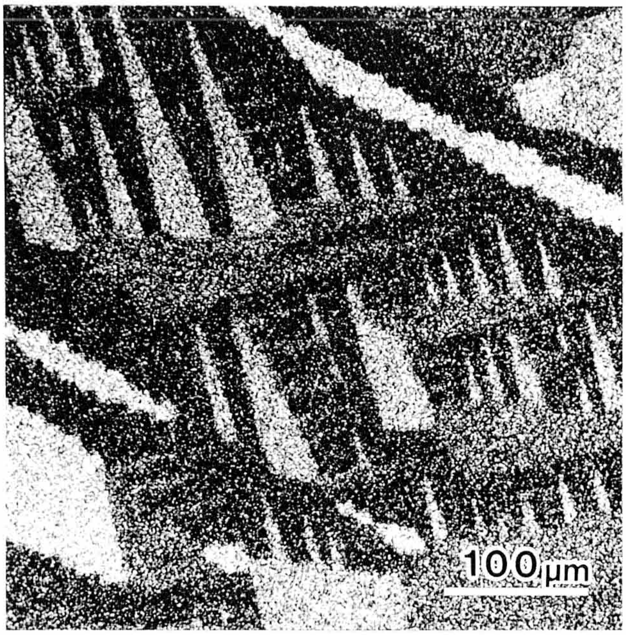

Fig. 4.2. Domain image of an Fe(001) surface obtained at high-speed scanning of 21 s/512 x 512 pixel image.[8]

High-speed scanning

Figure 4.2 shows a domain image of Fe(001) surface obtained at high-speed scanning. It took 21 s to form the 512 x 512 pixel image. Although the *S/N* of the image is not sufficiently high, the domain structure is roughly realized. It can be seen that this scanning mode can be used for rapid viewing.

Different pixel number image

The comparison among different pixel number images was made under high-speed scanning conditions. Here, 50 µs/pixel multiscanning was used to obtain images of an Fe(001) surface with the same net image-acquisition time of 13 s, i.e., at a repetition of 64 times for 64 x 64, 16 times for 128 x 128, 4 times for 256 x 256, and once for 512 x 512. These images are shown in Fig. 4.3(a)~(d). by increasing the pixel number, the outline of the domain structure gradually becomes visible, and the domain boundary of each image gradually become sharper. Although general conclusions cannot be derived using only these results, for images having few gradations, the larger pixel-number image seems to be more informative than the fewer pixel-number images if the net image-acquisition time is the same.

Multiscanning

Figure 4.4(a)~(e) shows domain images of polycrystalline Fe obtained with 1, 3, 10, 30, and 100 repetition multiscanning of the same area. Each scan speed is 50 µs/pixel, and requires 21 s/image, 63 s/image, 4.5 min/image, 10.5 min/image, and 35 min/image, respectively. A surface topographic image is shown in Fig. 4.4(f), in which grain and scratch contrast appears. In Fig. 4.4(a), we can roughly see three large domains in the right part of the image but can hardly identify existing fine domains in the left part because of low *S/N* image. With increasing scanning repetition, details of fine domain structure in the left part of the image are gradually visible. At first glance, Figs. 4.4(d) and 4.4(e) are the same. However, close inspection shows Fig. 4.4(e) has less noise and the domain structure, especially in the left half region, is more clearly visible than Fig. 4.4(d). The image quality of Fig. 4.4(d) is good enough to quantitatively analyze the domain structure. However, a better quality image of Fig. 4.4(e) might be necessary for quantitative analysis. The multiscanning mode enables the operator to

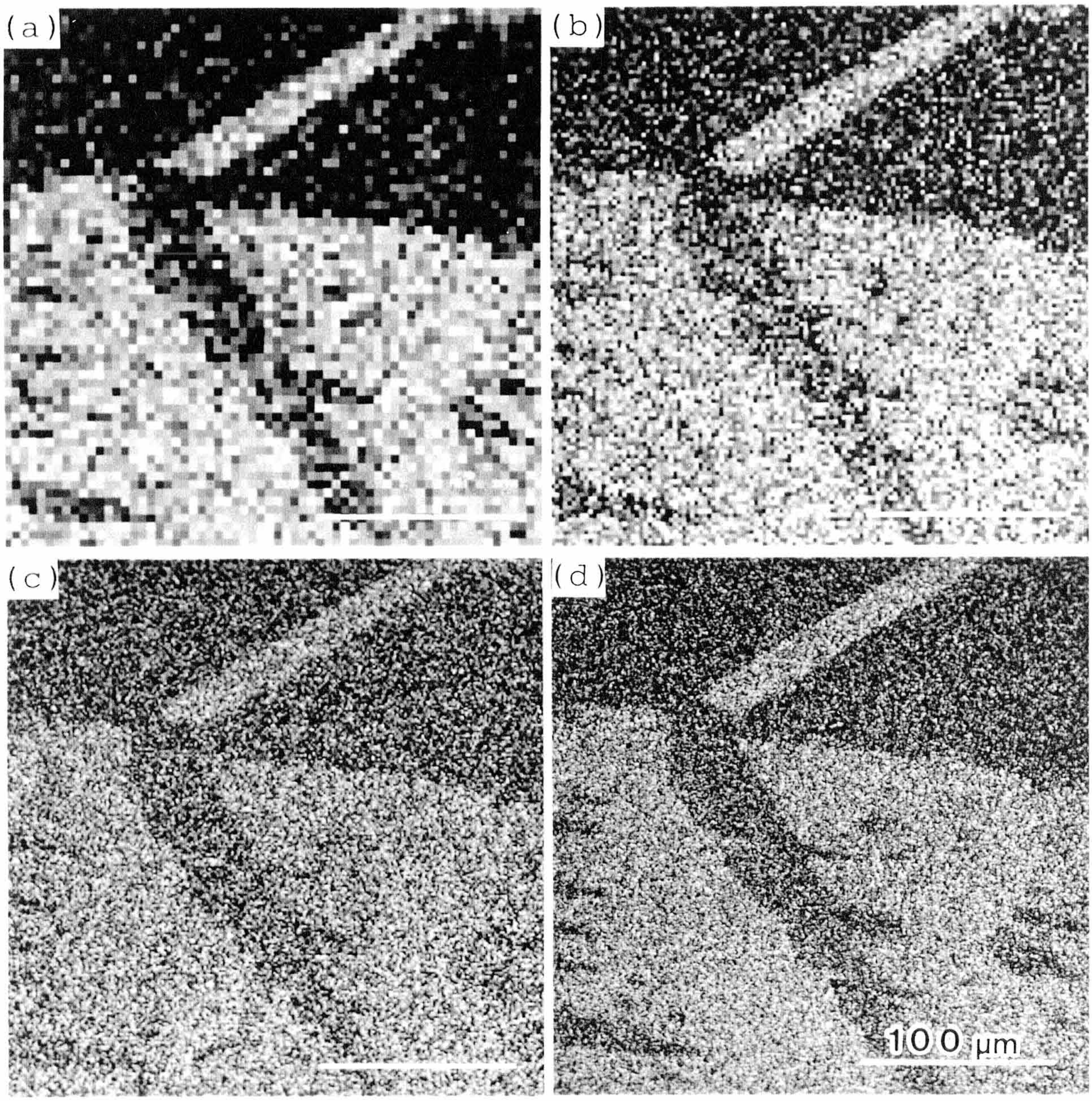

Fig. 4.3. Comparison among different-pixel number images: (a) 64 x 64, (b) 128 x 128, (c) 256 x 256, (d) 512 x 512.[8]

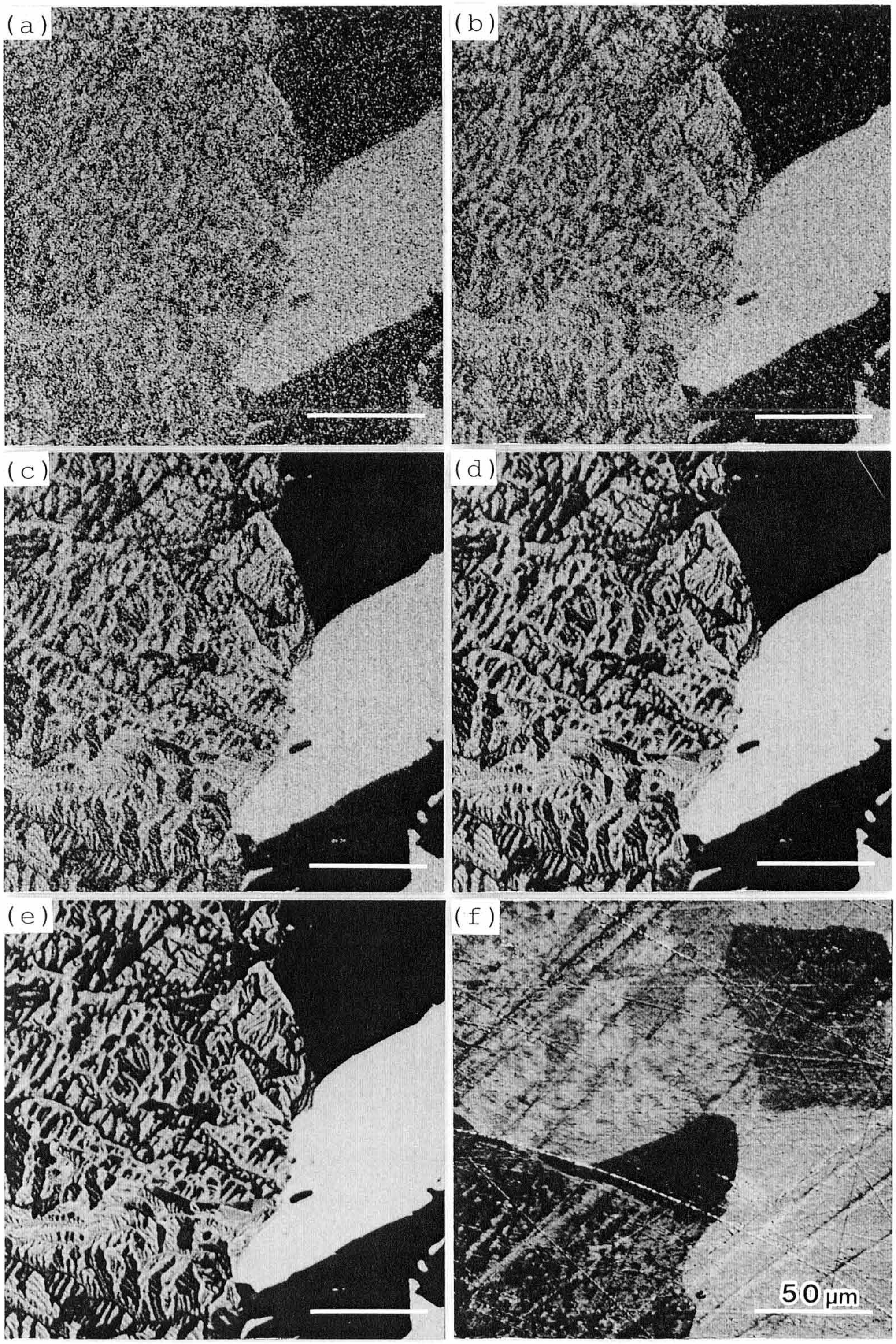

Fig. 4.4. Domain images (a)~(e) and a morphology image (f) of Fe polycrystal obtained by multiscanning. The number of repetitions: (a) 1, (b) 3, (c) 10, (d) 30, (e) 100.[8]

monitor noise reductions and stop scanning when the image quality matches the observation purpose.

Rescanning

A result of the magnified scanning is shown in Figs. 4.5(a) ~ 4.5(d). Figures 4.5(a) and 4.5(b) are polycrystalline Fe domain images obtained from P_x and P_y, respectively, at 512 x 512 pixel scanning of 8 ms/pixel. Figures 4.5(c) and 4.5(d) are domain images obtained by 512 x 512 pixel magnified scanning of 8 ms/pixel, magnifying the area surrounded by the square frame in (a) and (b), respectively. The frame size can be selected from 1/2, 1/4, and 1/8 of the initial image and its position can be moved anywhere with the mouse. The fine domain structures that are not visible in (a) and (b) are visible in both (c) and (d), since the domains in the area are much smaller than pixel size in (a) and (b).

Variable speed scanning

Figures 4.6(a) and 4.6(b) show the domain images of the same area of an Fe single crystal obtained in constant speed and variable speed scanning. The area includes two surface planes having different inclinations. Figure 4.6(c) shows a schematic diagram of the sample arrangement against the Mott detector. It took about the same time of 10 min to obtain each image. The secondary electron intensity of the side plane of the sample decreases compared to that of the area facing the Mott detector. As a result, the image of the side area is not as clear as that of the other area as can be seen in Fig. 4.6(a). The image of the side plane in Fig. 4.6(b), however, is improved, and the noise of the image (b) is nearly constant over the whole area. Thus the variable speed scanning is very useful to observe samples that have an area where secondary electron intensity extremely decreases.

The application of the scanning to the observation of a magnetic recording head is shown in Fig. 4.7. The sample is an amorphous Co alloy film deposited on a three-dimensional Mn-Zn ferrite single crystal by sputtering method. A schematic diagram of a sample arrangement is illustrated above the domain image. A fine domain structure of Co film having different gradient can be seen clearly on all four surfaces, and the fine domain structure of the ferrite can also be seen on the lower part of the image. The simultaneous observation of different surfaces is a

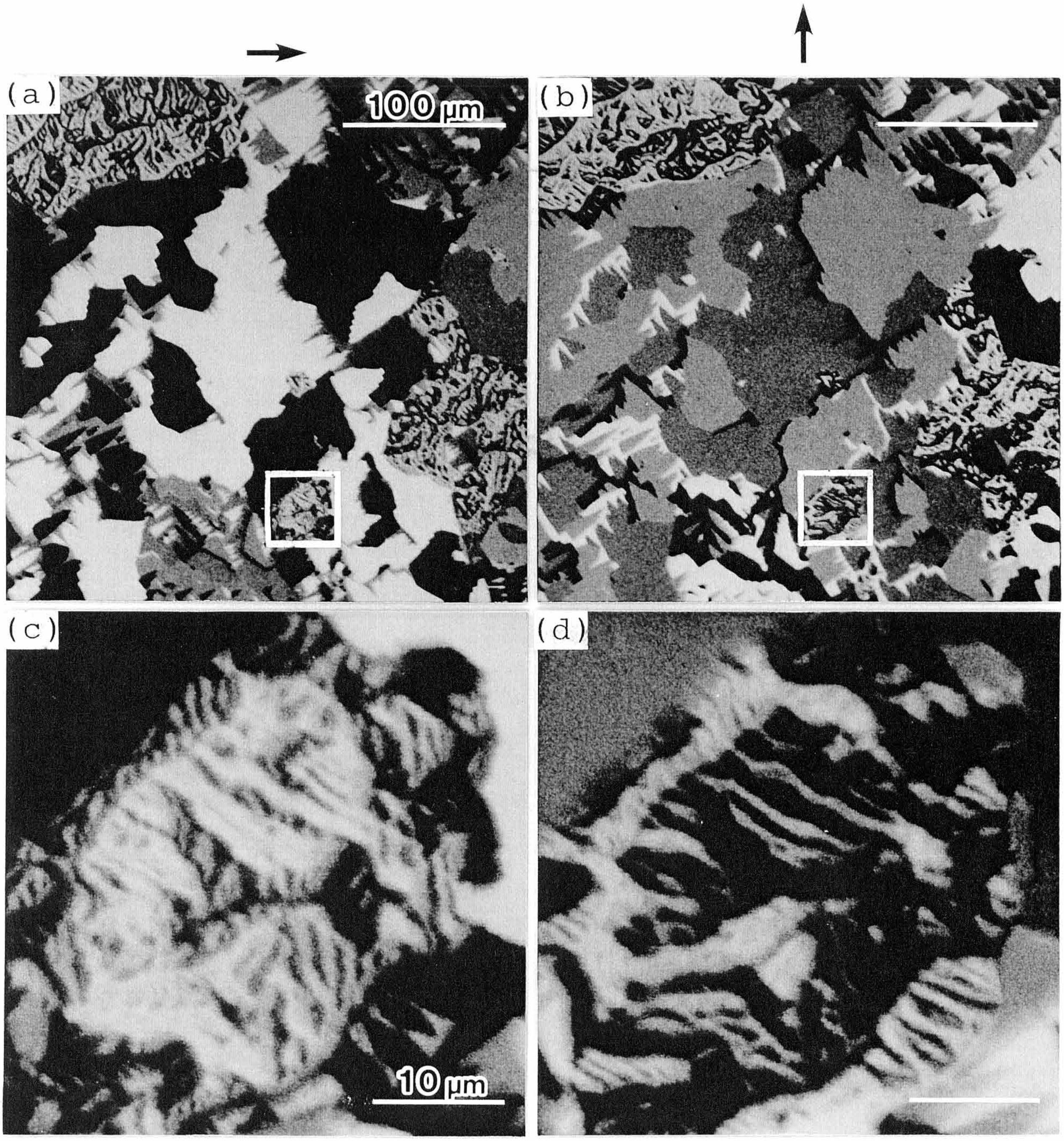

Fig. 4.5. Domain images (a) and (b) of Fe polycrystal. Detection directions are indicated by arrows on the top of each image. Domain images (c) and (d) obtained by rescanning applied to the area indicated by the squares in (a) and (b).[8]

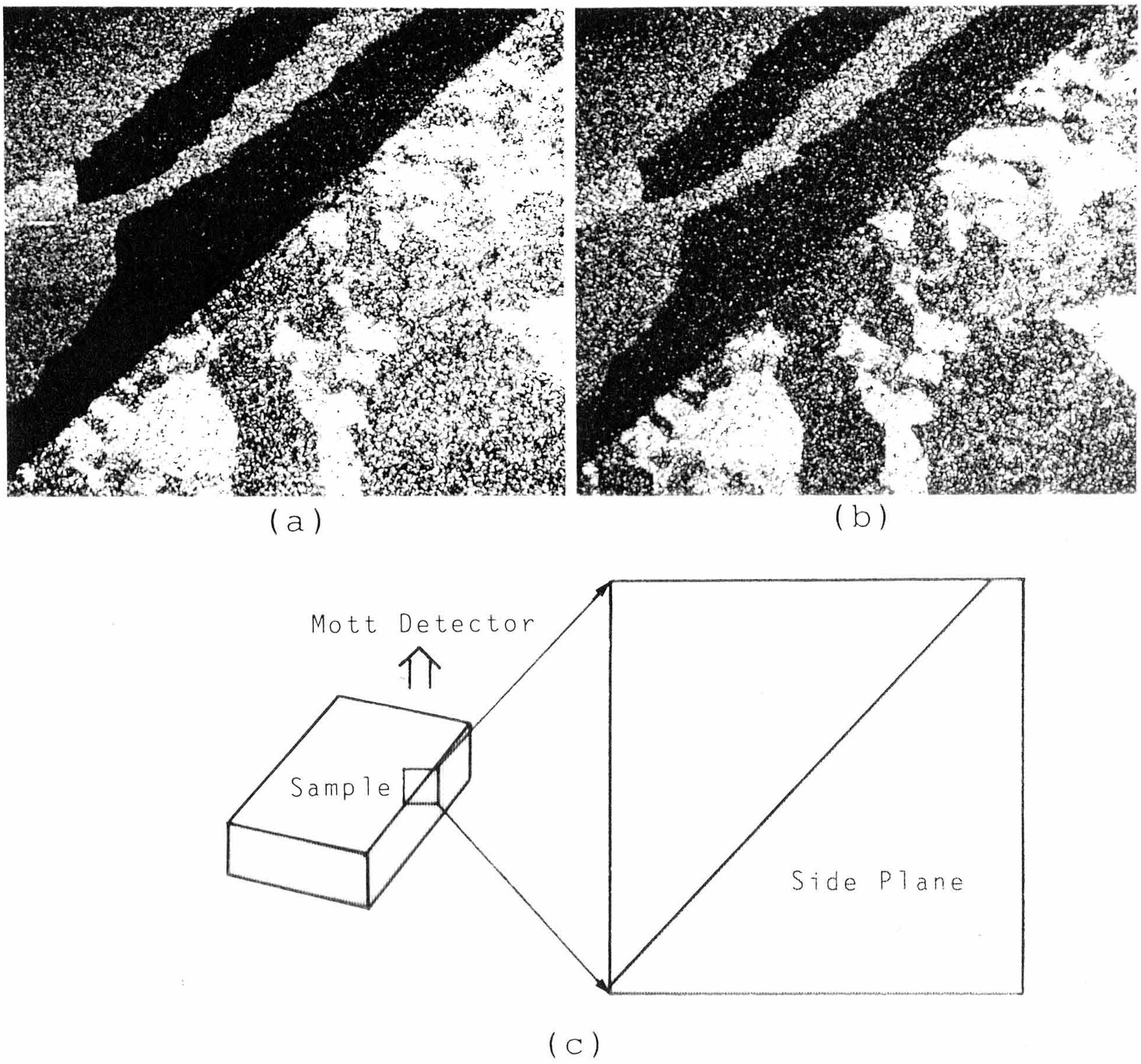

Fig. 4.6. Domain images (a) and (b) of an Fe(001) surface obtained at constant speed and variable speed scanning, respectively, and schematic arrangement (c) of a sample.[8]

unique capability of the spin SEM which is not obtainable by conventional methods.

High-speed reproduction of the image

Figure 4.8 shows an example of the high-speed reproduction of domain images by using arbitrary polarization component. Figures 4.8(a) and 4.8(b) are domain images of Fe polycrystal and were obtained in 35 min from P_x and P_y. Figures 4.8(c) and 4.8(d) were obtained in 8 s by calculating from P_x image (a) and P_y image (b). The arrows at the upper left of each image show the direction, along which a magnetization vector component is used as the image signal. The direction in (c) is selected to emphasize the surface 180° Néel wall[7,11,12] as black or white lines, indicated by arrows in the figure. In Fig. 4.8(d), a smaller wall contrast appears as indicated by the arrows in the image. However, the wall is out of the straight and the width of the wall is thicker than the 180° Néel wall in (c). Since the black and white contrast between the domains on both sides of the wall in (a) or (b) disappears, leaving the black or white wall in (d), the magnetization vectors in these domains are antiparallel to each other and perpendicular to the wall. The magnetization seems to rotate on the surface by a 180° degree angle like the surface Néel wall, or it might be a small part of domain located under the surface. At a glance, the magnetic structure in the left lower part of the images P_x (a) and P_y (b) seems very complex. However, the above analysis shows it has such a simple structure that the magnetization of each domains are almost antiparallel to each other.

Quantitative analysis -vector mapping and angle representation-

A domain image of an Fe(001) surface obtained by a 10 ms/pixel scanning is shown in Fig. 4.9(a). It had been verified that the instrumental asymmetries, i.e., offset polarization are constant all over the observation area by observing a nonmagnetic copper sample beforehand. The measured polarization components P_x and P_y, including the offsets on a line $\overline{pq}$ in (a), are shown in Fig. 4.9(b). They are constant within statistical error in the same domains indicated by i, j, k in (a) and (b) because of the constant offset. On the assumption that all magnetization vectors lie in the surface plane, which is the case for Fe (001), the offsets were corrected so that all polarization vectors had the same magnitude. The magnetization vectors are represented as the arrows on the domain image in Fig. 4.10. As can be expected from the theory, four

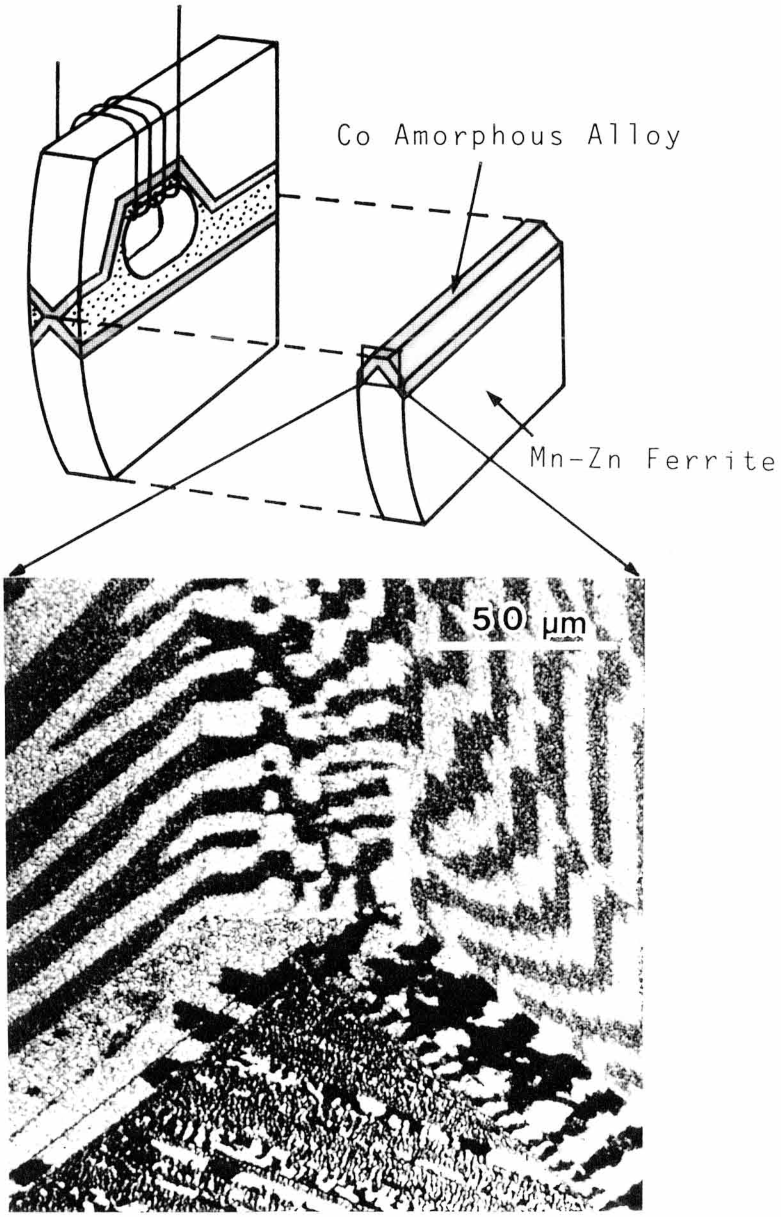

Fig. 4.7. Domain image of a three-dimensional-shaped magnetic recording headcomposed of amorphous Co alloy film deposited on a Mn-Zn ferrite single crystal, and schematic arrangement of the sample in the top of the image.[8]

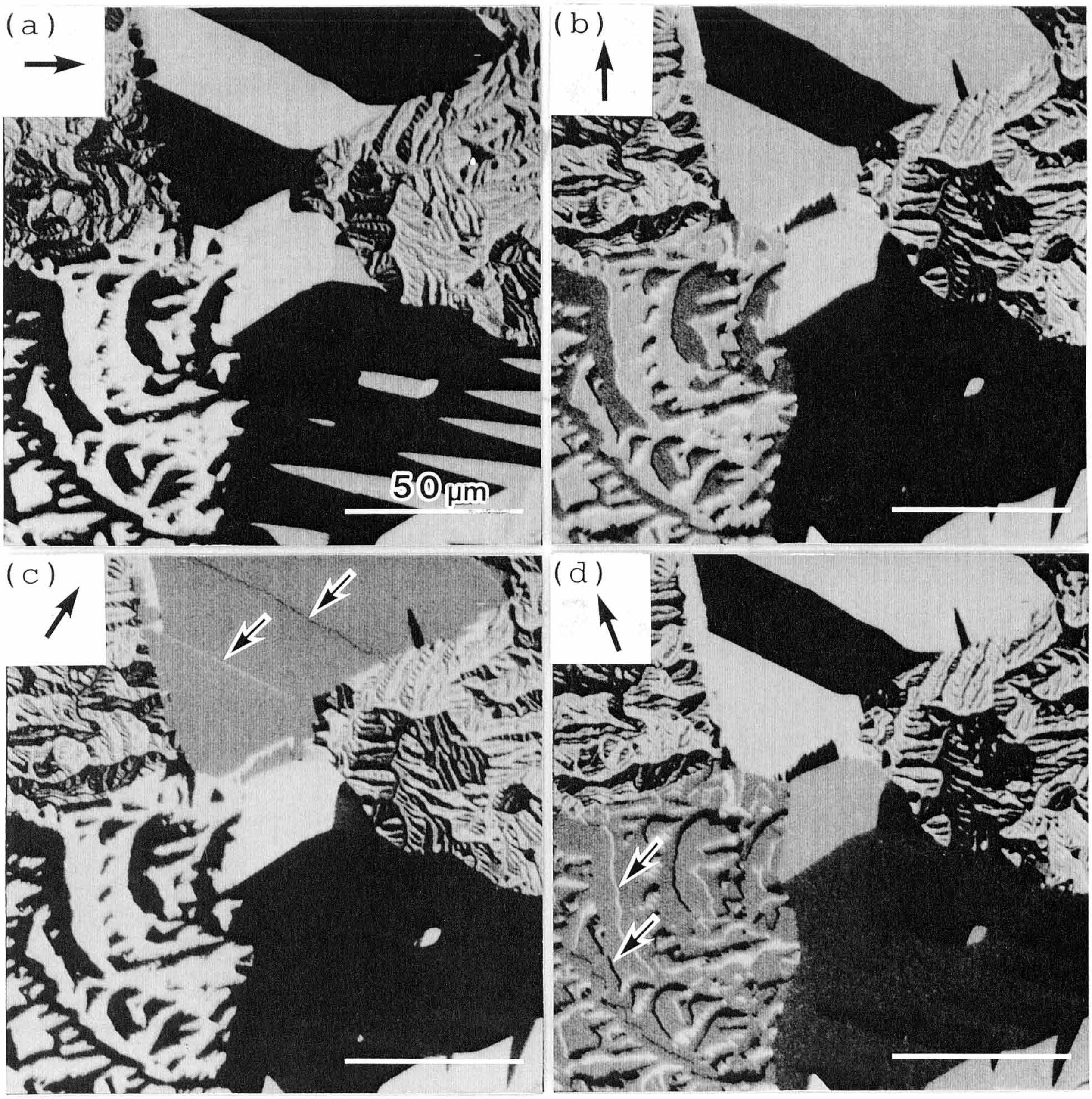

Fig. 4.8. High-speed reproduction of Fe polycrystal domain image. The images (c) and (d) are computed from (a) P_x image and (b) P_y image in 8 s/512 x 512 pixel image. The detection direction of each image is shown as an arrow at upper left of the image. These directions of (c) and (d) are selected to show domain boundary contrast indicated by arrows.[8]

magnetization directions which are perpendicular to each other can be recognized. Magnetization in every domain fluctuates more or less in both direction and magnitude due to statistical uncertainty. Vector calculation was performed using only point data, i.e., without averaging. Regarding preciseness, this method might best represent magnetization directions. However, if there are so many domains that the domain size is smaller than the arrow length, this representation causes confusion. Figure 4.11 shows such an example of Fe (001).

In this case, it is preferable to use the vector angle as a brightness signal of the image. Figure 4.12(a) shows this example. The image data is the same as Fig. 4.11. The gray level of the image is correlated with the magnetization direction through the gray-scale wheel shown in Fig. 4.12(b). Since every pixel point can show its magnetization direction within its own pixel area, no confusion appears even for images having many small domains. One of the problems of this representation is that it is not very easy to accurately understand magnetization directions only from the gray level. This is because eyesight is illusive and does not have ability to precisely detect absolute gray levels. Another problem is there is a discontinuity at the left middle part of the gray-scale wheel. This causes noisy areas that can result in incorrect interpretation of the domain structure. Figure 4.12(c) shows such an example, where the image data is the same as Fig. 4.9(a). The magnetization vector in the areas shown by arrows lies in the direction of the discontinuity in the gray-scale wheel of Fig. 4.12(b). Because of statistical noise, the detected magnetization vector usually fluctuates against this direction causing the noisy areas. The areas look as though many small domains were there. Using color domain representation solves this problem.

Figure 4.13(a) is obtained by replacing the gray scale of Fig. 4.12(c) with colors. Each color is correlated with magnetization directions through the color-wheel shown in Fig. 4.13(b). Since there is no discontinuity for any direction, no appreciable noise is seen.

Figure 4.13(c) shows the color representation of Fig. 4.8. The bluish green and orange domains in the upper middle of the image indicate their magnetization directions are parallel to the wall between them and antiparallel to each other. The greenish yellow and purple walls indicate their magnetization directions are perpendicular to the domain walls and antiparallel to each other. The red and green domains in the lower left of the image indicate their magnetization directions are perpendicular to the walls and antiparallel to each other. The yellow and blue walls between them indicate their magnetization directions are almost parallel to the walls but antiparallel to each other. These results confirm the previous analysis discussion regarding Fig. 4.8. By the color representation, we can understand the magnetization direction not only in the larger domains but also in the fine domains. The fine domain areas in upper left and middle right part of the image can be divided into subareas with predominant colors of yellow, green, and purple. This analysis is very difficult only with domain images where image signals are magnetization vector components such as in Fig. 4.8.

Figure 4.14 shows an example of (a) the color representation and (b) the vector mapping applied to a 3-D sample. The sample is a four-layered magnetic film that has been studied for use as a thin magnetic layer (0.5 μm thick) consisting of ten Fe-C/Ni-Fe sublayers (45 nm/5 nm thick), which are piled up on an amorphous-Si substrate with 10-nm-thick boron nitride spacers in between. In Fig. 4.14(a), we can identify four magnetic layers by alternate arrangement of yellow and blue bands on the right-side plane, corresponding to upward and downward magnetization-direction areas, respectively. We can see two magnetic domains on the topmost layer, with a well-known edge curling wall on the areas near both the left and right edges. For this kind of multilayered film, layer dependency of the magnetization direction is predicted to be alternate by Slonczewski, Petek, and Argyle.[13] This prediction can be confirmed by analyzing the domain structure on the side plane which includes the easy axis of the magnetization, due to the film's presence (refer to Chapter 5). For the sample in Fig. 4.14, we thought the easy axis was in the horizontal direction, i.e., parallel to the lower side plane, because the magnetic field in this direction had been applied to the sample during production. Observation on the lower side plane shows the magnetization direction of the top-most layer points to the right. This result does not agree with Slonczewski's prediction of the alternate arrangement of magnetization directions. Although we have observed many strips not only on the same substrate but also on other substrates, the predicted arrangement is very rare. Various reasons may explain the discrepancy, but currently it remains unknown.

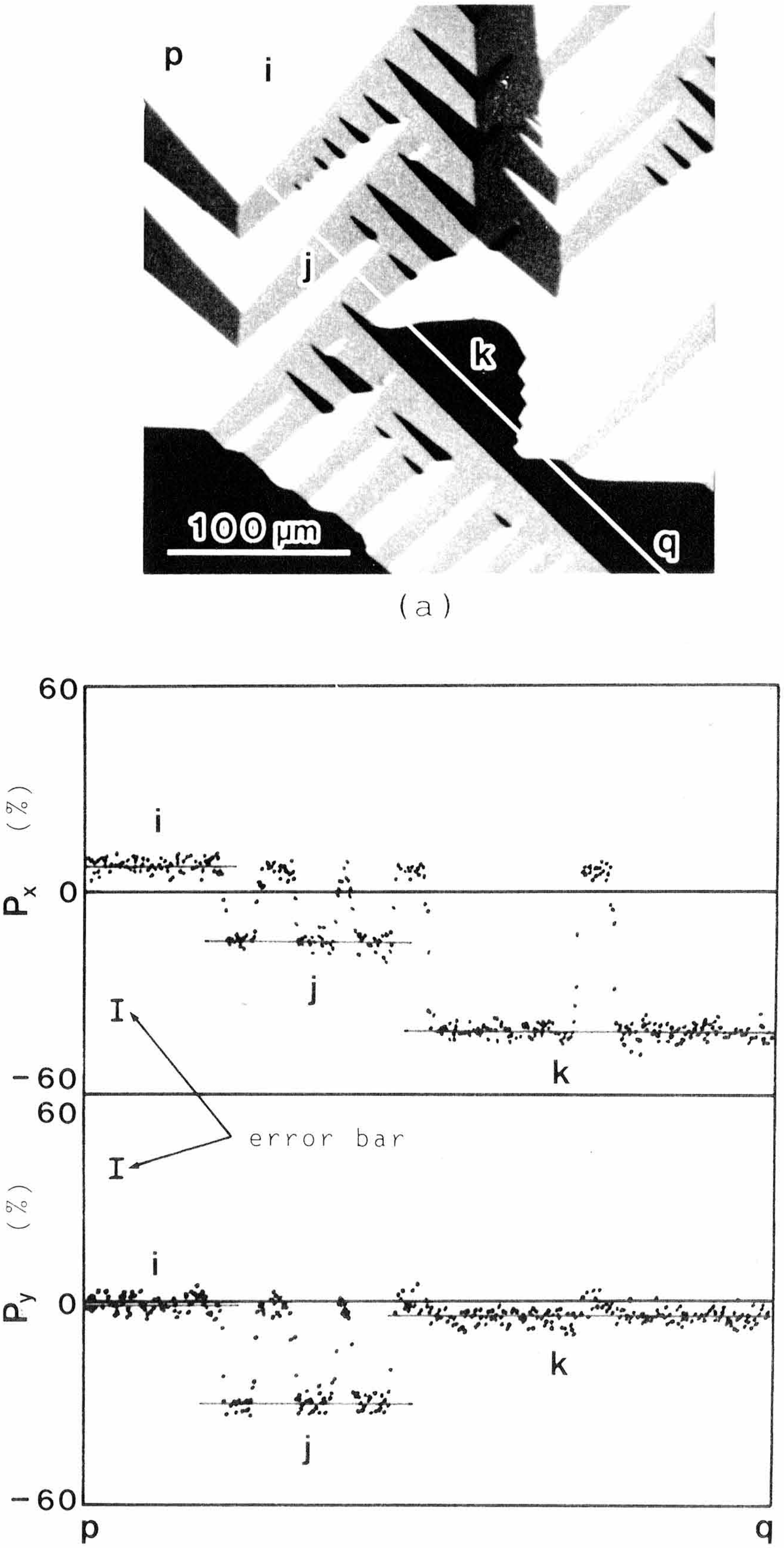

(a)

(b)

Fig. 4.9. Domain image (a) of an Fe (001) surface and polarization components P_x and P_y (b) on a straight line pq.[8]

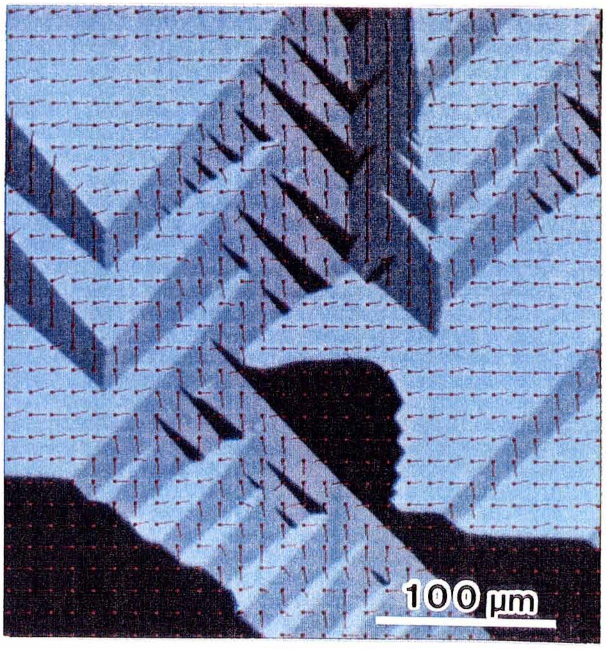

Fig. 4.10. Vector mapping of magnetic microstructure superimposed on the domain image of Fig. 4.9(a).[8]

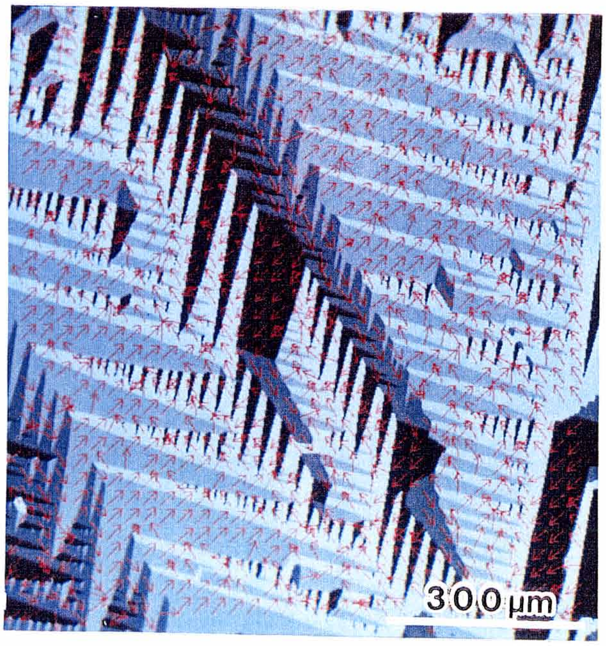

Fig. 4.11. Vector mapping of the magnetization directions on an Fe (001) surface.[8]

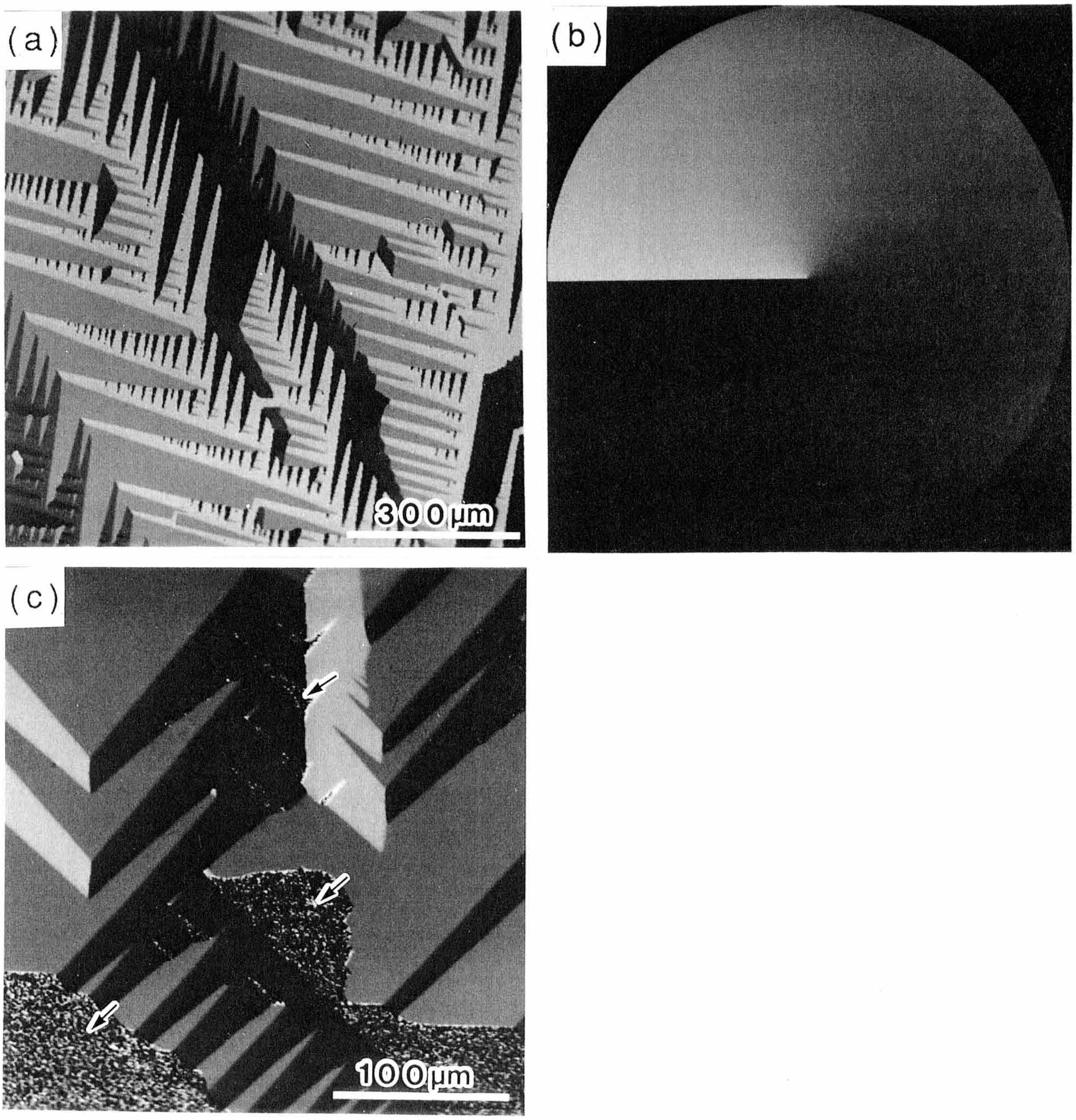

Fig. 4.12. Angle representation of the magnetization direction. (a): angle image of an Fe (001) calculated from the polarizations P_x and P_y of Fig. 4.11. (b): gray scale wheel. (c): angle image of an Fe (001) calculated from the polarizations P_x and P_y of Fig. 4.9(a).[8]

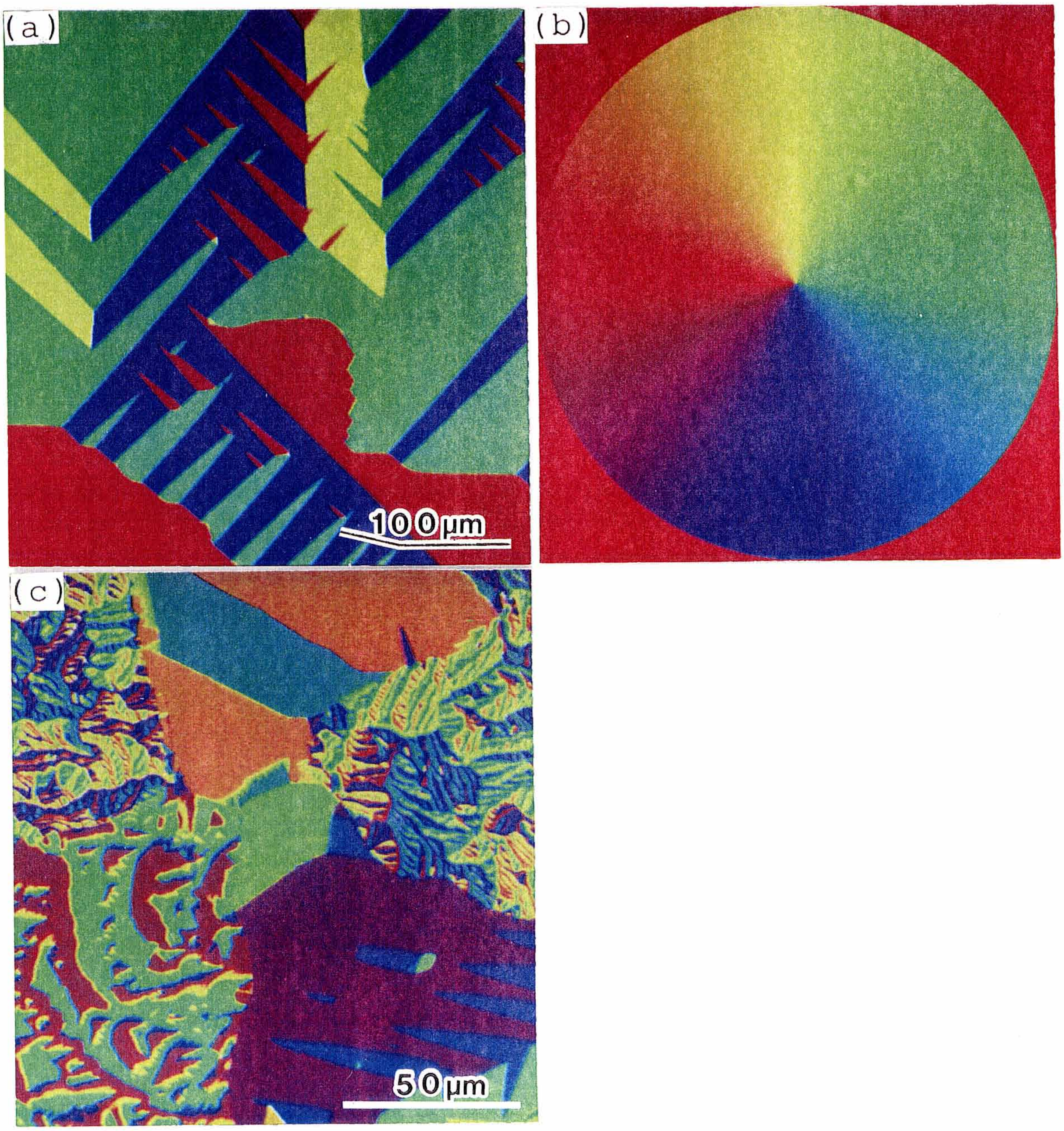

Fig. 4.13. Color representation of the magnetization direction. (a): color image of an Fe (001) calculated from P_x and P_y of Fig. 4.12(c). (b): color wheel. (c): color image of Fe polycrystal calculated from P_x and P_y of Fig. 4.8.[8]

Figure 4.14(b), where the arrows indicate magnetization directions more quantitatively than the colors in Fig. 4.14(a), shows that the magnetization direction in the middle part of the domains inclines against the lower edge line by some 30°. This means the easy axis also inclines by some 30°, which differs from our initial expectation mentioned above. It is unknown if this difference caused the discrepancy mentioned above. Figure 4.14(b) also shows that the magnetization directions on the left and lower side planes are precisely parallel to their respective planes, although the easy axis inclines against these planes. This result is reasonable because a soft magnetic material tends to have magnetic structures that minimize magnetic charges on its surface. The magnetization direction on the right side plane is probably also parallel to the plane, although the shorter length arrows do not show this clearly. The short arrow length was obtained because the sampling points for vector mapping were accidentally on the boundary of two layers having opposite magnetization directions. The probe beam hitting these points stretches over these two layers, because of the oblique incidence against this plane, producing apparently smaller magnetization.

4.5 Conclusions

A data-acquisition and display (DAD) system for the spin SEM has been developed. This system enables high-speed scanning, computing, recording of P_x and P_y, multi and magnified scanning for ease of operation, obtaining a constant-noise image even when secondary-electron intensity varies due to surface orientation, image formation for an arbitrary component, vector mapping of the magnetization distribution, and angle image of the magnetization direction in both black and white and color representation. It has been confirmed that the spin SEM with the DAD system is a powerful tool for the study of magnetic microstructures for industrial applications, especially magnetic recording, and also for basic research.

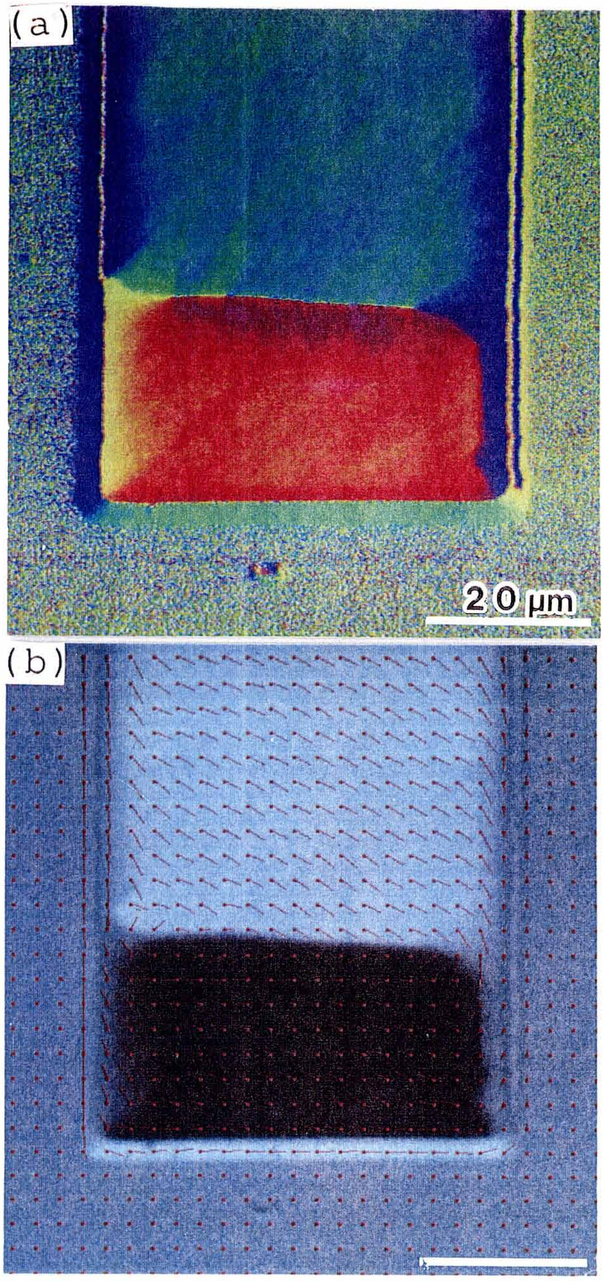

Fig. 4.14. Color representation (a) of a Fe-C/Ni-Fe/BN multilayer strip on an amorphous-Si substrate for a magnetic recording head. Vector mapping (b) on the same area of (a).[8]

References

1. W. Rave, R. Schafer, and A. Hubert, J. Magn. Magn. Mater. **65**, 7 (1987).

2. K. Koike and K. Hayakawa, Jpn. J. Appl. Phys. **23**, L187 (1984).

3. J. Unguris, G. G. Hembree, R. J. Celotta, and D. T. Pierce, J. Microsc. **139**, RP1 (1985).

4. J. Kirschner and R. Feder, Phys. Rev. Lett. **42**, 1008 (1979).

5. K. Koike and K. Hayakawa, Appl. Phys. Lett. **45**, 585 (1984).

6. K. Koike, H. Matsuyama, and K. Hayakawa, Scanning Microsc. Suppl. **1**, 241 (1987).

7. G. G. Hembree, J. Unguris, R. J. Celotta, and D. T. Pierce, Scanning Microsc. Suppl. **1**, 229 (1987).

8. H. Matsuyama and K. Koike, Rev. Sci. Instrum. **62**, 970 (1991).

9. J. Unguris, M. R. Scheinfein, R. J. Celotta, and D. T. Pierce, Appl. Phys. Lett. **55**, 2553 (1990).

10. J. van Klinken, Nucl. Phys. **75**, 161 (1966).

11. H. P. Oepen and J. Kirschner, Phys. Rev. Lett. **62**, 819 (1989).

12. K. Koike, H. Matsuyama, K. Hayakawa, K. Mitsuoka, S. Narishige, S. Sudo, Y. Sugita, K. Shiiki, and C. Saka, Appl. Phys. Lett. **49**, 980 (1986).

13. J. C. Slonczewski, B. Petek, and B. E. Argyle, IEEE Trans. Magn. **MAG-24**, 2045 (1988).

5. Application of DAD System

—Side Plane Domain Observation of Fe-C/Ni-Fe/BN Multilayers—

5.1 Introduction

Laminating of soft-magnetic films separated by nonmagnetic layers in a thin-film recording head has been reported to enable high-frequency response due to the elimination of domain walls.[1] Recently, in order to clarify the mechanism of this elimination, Slonczewski calculated the magnetization distribution of multilayers, and proposed an edge curling wall (ECW).[2] The ECW decreases the magnetic energy of the film by allowing the magnetic flux to close at the edge of the film. As a result, each coupled layer from the top (or bottom) in the multilayers has an antiparallel magnetization structure.

The ECW of the top layer was confirmed experimentally using Kerr microscopy[2] and spin SEM.[3] Recently, domain observation in both the top and bottom layers of four and two laminated films was made.[4] However, magnetization distribution in the intermediate layers has not yet been observed, because there is now no possible observation method. It is thought to be possible to infer the distribution of the intermediate layers from distribution on the end plane parallel to the easy axis (easy side). This is because the presence of the easy side does not affect the magnetic structure inside the film, since, in this case, no magnetic charge appears on this surface. However, it is quite difficult to perform end plane observation with conventional methods such as Kerr, Bitter, and SEM (Type I and II).

Spin SEM has some excellent capabilities: morphology-independent detection of the magnetization, quantitative detection of the magnetization direction, high spatial resolution. These capabilities make it possible to observe the magnetization distribution on the sides of the film with high spatial resolution. The first observation of the magnetization distribution on the side planes of multilayers using spin-SEM[5] will be given in this Chapter.

5.2 Experimental

Four magnetic layers (0.5 µm/layer), separated by boron-nitride nonmagnetic spacers, were prepared by ion beam sputtering.[6] In order to avoid the charge buildup phenomenon during SEM observation, polycrystalline-Cu and amorphous-Si substrates were used, although the films must be deposited on a nonconductive material for use in a commercial recording head. The thickness of the spacers was 10 nm for the Cu substrate and 15 nm for the amorphous-Si substrate. Each magnetic layer (0.5 µm) consists of ten Fe-C/Ni-Fe sublayers (45/5 nm). The sputtering was performed in the following conditions: 1.9×10^{-5} Torr Ar pressure, 0.2~0.3 nm/s deposition rate. After deposition, the films were annealed at 400 °C for 1 h in an Ar atmosphere. The saturation magnetic flux density, $B_{s,}$ of each film was measured with a vibrating sample magnetometer while applying a magnetic field of 8×10^5 A/m. The films were formed into rectangle-shaped strips (300×50 µm^2) by ion milling, where the easy axis of the sample was parallel to the short edge (50 µm) of the strip. The coercive force, *Hc*, of the strip on the amorphous-Si was measured with a B-H curve tracer at a frequency of 40 Hz. Measured values are $B_s = 1.9$ T and $H_c = 110$ A/m. All films were demagnetized by applying an alternating magnetic field of 8×10^5 A/m along the hard axis, then decreasing its amplitude gradually to zero.

5.3 Domain Observations

Domain observations were made under a base pressure of 3×10^{-10} Torr after sample-surface cleaning by Ar-ion bombardment (2 kV, 12 µA) for 10 min. The probe beam energy was 4 keV and the incident angle was 60° from the sample-surface normal. Therefore, the domain image of the side was obtained without tilting the sample. 36 min were required to produce three 512 x 512 pixel images composed of the *x, y* components of magnetization and a sample-absorbed current. For a quantitative representation, the magnitude and the angle of magnetization were calculated from the *x*, *y* components and were displayed as an arrow in a domain image.

The following results were obtained. Since similar magnetic patterns were observed for the strips on both Cu and Si substrates, two typical patterns for each substrate are shown in Figs. 5.1 and 5.2.

Domain images of Fe-C/Ni-Fe/BN multilayer strips on the Cu-substrate are shown in Fig. 5.1. Figures 5.1(a) and 5.1(b) are obtained from a single strip but using different magnetization components represented by the arrows at the top of each image. Figures 5.1(c) and 5.1(d) are from another strip. The ECWs can be clearly seen in Figs. 5.1(b) and 5.1(d) along both the right and left hard-axis edges with gradual change in their brightness from the edges. Moreover, 180° domain walls, which are accompanied with closure domains at the edges, can also be seen in Figs. 5.1(b) and 5.1(d). In Fig. 5.1(a), the magnetizations of the easy side are alternately aligned layer by layer, consistent with Slonczewski's prediction, but unexpected small domains near the corner can be seen which will be discussed later. On the other hand, the magnetizations of the easy side in Fig. 5.1(c) have a higher magnetic energy than that of Fig. 5.1(a). This kind of nonalternately aligned distribution was observed in many other strips. One interpretation is that the multidomain structure seen in the top layer of Fig. 5.1(c), which seems to have no correlation between the neighboring layers, destroys the calculated layer dependency. In fact, we can see corroboration of the multidomains in these images. One is the fine structure on the hard-axis sides which seems to be caused by the closure domain. Another is a quasi-wall coupled to a 180° wall in the underlayer which can be found as the weak dark contrasts indicated by arrows on the top layer of Fig. 5.1(d). This multidomain structure is thought to be caused by the surface roughness of the Cu substrate, resulting from mechanical polishing with about 1-µm-diameter polishing particles. To remove the influence of surface roughness, we prepared an amorphous-Si substrate, the surface roughness of which was less than 10 nm.

Domain images of Fe-C/Ni-Fe/BN multilayer strips on this amorphous-Si substrate are shown in Fig. 5.2. Figures 5.2(a) and 5.2(b) are obtained from a single strip but using different

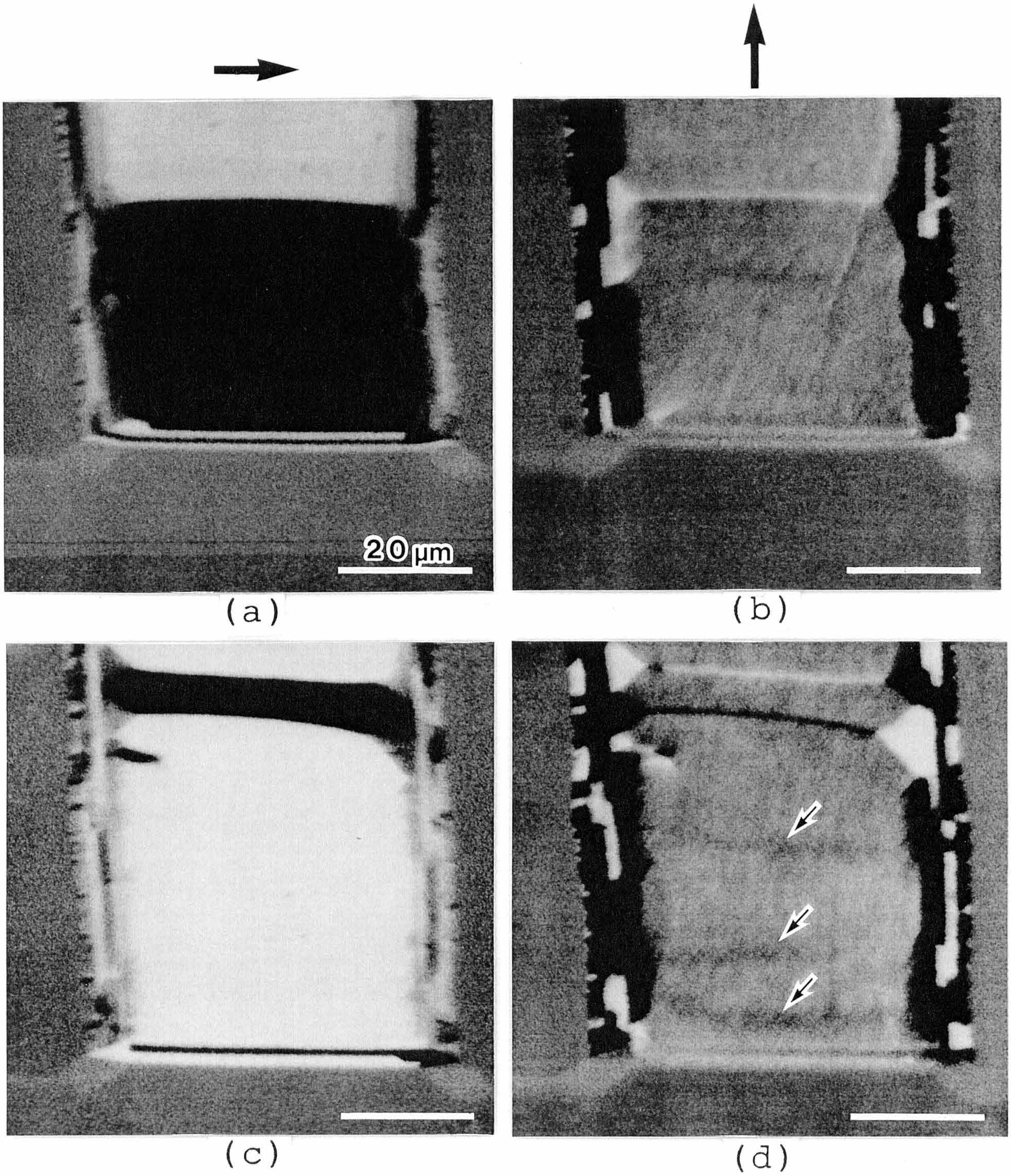

(a) (b)

(c) (d)

Fig. 5.1. Domain images of Fe-C/Ni-Fe/BN multilayer strips on a Cu substrate. (a) and (b) are obtained from a single strip but using different magnetization components represented by the arrows at the top of each image. (c) and (d) are those of a second strip.[5]

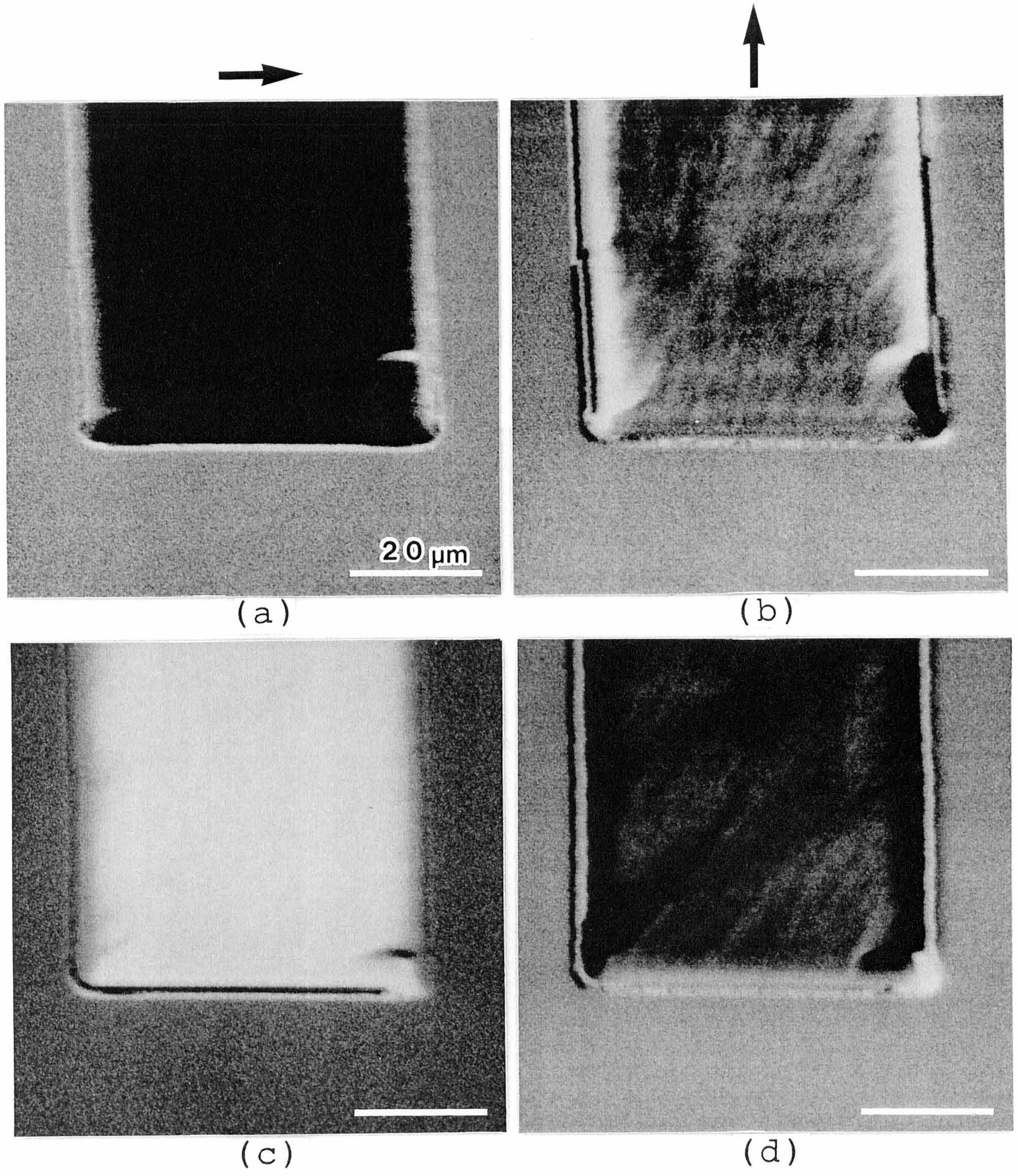

Fig. 5.2. Domain images of Fe-C/Ni-Fe/BN multilayer strips on an amorphous-Si substrate. (a) and (b) are obtained from a single strip but using different magnetization components represented by the arrows at the top of each image. (c) and (d) are those of a second strip.[5]

magnetization components in the same way as in Fig. 5.1. Figures 5.2(c) and 5.2(d) are those of another strip. On the top surface of both strips, Figs. 5.2(b) and 5.2(d), single domain structures with simple ECWs on both hard sides are observed. No fine magnetic structures on the hard sides and no quasi-wall contrast are observed different from the case in Fig. 5.1. This suggests that the cause of the multidomain structure is the surface roughness of the Cu substrate. However, magnetizations are again aligned in a high-energy -like state on the easy side of both strips, and similar distributions were observed in many other strips on the same substrate. The cause of this high-energy-like state might be the following: a small magnetic-energy difference between the structure of Fig. 5.1(a) and that of the others, and local energy-minimum of the latter; exchange interaction through the defects in the nonmagnetic spacer, which tends to align the magnetization of interacting layers in the same direction. Too much exchange interaction through the defects would probably simply make the sample act as a single layer. However, it is unknown at present which cause is dominant or if any other exists.

Finally, we must consider the unexpected small domain structure near the bottom left corner of the easy side in Fig. 5.1(a), where the magnetization direction appears to be opposite to the rest of the area of the same layer. For this purpose, observation of the strip in Fig. 5.1(a) was made at a higher magnification, and the magnetization directions were calculated from x and y components of the detected magnetization vectors. The vector mapping, superimposed on the domain image which is the magnetization of Fig. 5.1(a), is shown in Fig. 5.3, in which we can see that the magnetizations of the top surface rotate near the bottom left corner. The similar vortex structure of the magnetization was also observed on the corner and the edge of the double-layer permalloy films by using Kerr microscopy.[7,8] This magnetic structure results from the fact that the magnetic charge on both the hard and easy sides is minimized and so is the magnetostatic energy.

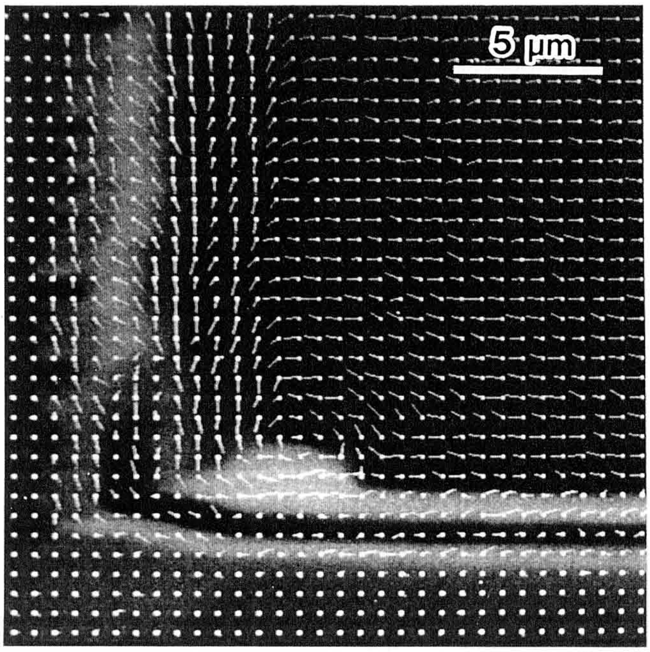

Fig. 5.3. Vector representation of the magnetization distribution of a section of the strip on the Cu substrate.[5]

5.4 Conclusions

By using spin SEM, the first domain observations of the top and side planes of rectangular four Fe-C/Ni-Fe/BN multilayers laminated on Cu and amorphous-Si substrates have been made. From the domain images of the side planes, it was found that the films do not always show the predicted energy minimum structure where the magnetization direction alternates layer by layer. Two possible causes for these results are suggested, however further study is necessary to clarify the details.

References

1. J. P. Lazzari and I. Melnick, IEEE Trans. Magn. **MAG-7**, 146 (1971).

2. J. C. Slonczewski, B. Petek, and B. E. Argyle, IEEE Trans. Magn. **MAG-24**, 2045 (1988).

3. K. Mitsuoka, S. Sudo, S. Narishige, M. Hanazono, Y. Sugita, K. Koike, H. Matsuyama, and K. Hayakawa, IEEE Trans. Magn. **MAG-23**, 2155 (1987).

4. D. A. Herman Jr., B. E. Argyle, P. L. Trouilloud, B. Petek, L. T. Romankiw, P. C. Andricacos, S. Krongelb, D. L. Rath, D. F. Canaperi, and M. L. Komsa, J. Appl. Phys. **63**, 4036 (1988).

5. H. Matsuyama and K. Koike, Appl. Phys. Lett. **57**, 2028 (1990).

6. R. Nakatani and T. Kobayashi, J. Appl. Phys. **67**, 1449 (1990).

7. D. A. Herman Jr., P. L. Trouiloud, B. E. Argyle, B. Petek, L. T. Romankiw, J. S. Bezama, D. L. Rath, D. F. Canaperi, and M. L. Komsa, IEEE Trans. Magn. **MAG-24**, 3066 (1988).

8. M. Ruhring, W. Rave, and A. Hubert, J. Magn. Magn. Mater. **84**, 102 (1990).

6. 20-nm Resolution Spin SEM

6.1 Introduction

Magnetic-domain observation is very important not only in such basic fields as the study of wall structures but also in industrial applications such as magnetic recording and permanent magnets. To improve the recording properties of recording media and heads, domain observation should be done with high spatial resolution.

Recording density is increasing rapidly, and the bit length in current products has reached 250 nm, a value corresponding to 100 k-flux changes per inch (FCI). To further increase the recording density by reducing the medium noise, it is necessary to control the shape of the recorded bit, since the medium noise is determined by the bit structures. To find the optimum conditions for medium preparation, recording, etc., we want to observe the detailed bit structure at a resolution smaller than the bit length. Among such domain-observing methods as Lorentz microscopy,[1] electron holography,[2] optical microscopy,[3] spin SEM, and magnetic force microscopy,[4] only the first and second (which are capable of 10-nm resolution) meet this resolution requirement.

Up to now, however, there have been no reports on the observation of bit structures, whose length is less than 250 nm. There are two reasons such reports have not appeared. The first is that the magnetic contrast obtained is too weak. This is because the amount of net magnetic flux, which is integrated through the whole electron path both inside and outside the medium, is generally canceled out because the magnetic flux inside and outside the bits runs in opposite directions. The second reason is that it is very difficult to remove the medium from the substrate.

In spin SEM, the magnetic contrast obtained is hardly affected by leakage magnetic flux from a sample and is independent of surface morphology. It is not necessary to thin the sample (i.e., to remove the medium from a substrate). Here, the spatial resolution of this method is expected to be less than 10 nm. Therefore, spin SEM is, in principle, suitable for observing the bit structures of the media. The highest resolution to date is only about 50 nm, which was achieved in both NIST[5] and Kernforschungsanlage.[6] This is not high enough to observe the bit structures of future-generation recording systems. In this Chapter, a newly developed spin SEM with a resolution of 20 nm[7] will be described.

6.2 System Design for High Spatial Resolution

6.2.1 Necessary Conditions

Roughly speaking, the domain resolution of a spin SEM is mainly determined by the probe diameter. A smaller beam diameter, however, results in lower probe current, thus increasing the statistical noise of the image. This issue is especially serious for the spin SEM since the efficiency of the spin detector is three to four orders of magnitude lower than that of the secondary electron detector used in an ordinary SEM. Thus, to get a resolution of less than 20 nm in an image, with a reasonable signal-to-noise ratio (*S/N*), a higher efficiency in the spin detector or higher probe current, or both, are required. The probe current required depends on the efficiency of the spin detector. In the spin SEM previously developed in our laboratory, it typically takes 30 minutes to obtain a high-*S/N* image even with a 2-nA probe current. In the new spin SEM, we have aimed to attain a resolution of less than 20 nm, with the same scanning time, in addition to obtaining an image with an *S/N* almost the same as that obtained with the previous one.

In the spin SEM, the *S/N* of a domain image is given by

$$\frac{S}{N} = \frac{\Delta P}{\delta P}, \qquad (6.1)$$

where ΔP is the polarization difference for domains to be distinguished, and δP is the statistical error of the polarization. Using Eq. (2.4) of Section 2.4, Eq. (6.1) becomes

$$\frac{S}{N} = \Delta P\sqrt{\xi S^2 N_o}\,. \tag{6.2}$$

N_o in Eq. (6.2) can be expressed using probe current I_p as

$$N_o = \frac{t\cdot\eta\cdot\zeta\cdot I_p}{e}, \tag{6.3}$$

where t is the time for one pixel, η is the secondary electron yield, ζ is the transmission rate of secondary electrons going through the secondary electron collector and transport optics, and e is the charge on one electron. From Eqs (6.2) and (6.3), S/N can be written as

$$\frac{S}{N} = \Delta P\sqrt{\frac{F\cdot\eta\cdot\zeta\cdot t\cdot I_p}{e}}\,. \tag{6.4}$$

Using Eq. (6.4), we can write the S/N ratio for both the previous and the new spin SEMs with the same polarization difference ΔP and the same pixel time t as

$$\frac{(S/N)_n}{(S/N)_p} = \sqrt{\frac{F_n\cdot\eta_n\cdot\zeta_n\cdot I_n}{F_p\cdot\eta_p\cdot\zeta_p\cdot I_p}}, \tag{6.5}$$

where the suffixes p and n denote the previous and the new spin SEMs. When the measured values F_p=6 x 10^{-6}, $\eta_p\cdot\zeta_p$=0.4, and I_p=2 nA are substituted into Eq. (6.5), we get

$$\frac{(S/N)_n}{(S/N)_p} = \sqrt{\frac{F_n\cdot\eta_n\cdot\zeta_n\cdot I_n}{4.8\times10^{-15}}}\,. \tag{6.5$'$}$$

This equation shows that the images obtained with both the previous and the new spin SEM have the same S/N if $F_n\cdot\eta_n\cdot\zeta_n\cdot I_n$ is 4.8 x 10^{-15} nA.

6.2.2 Electron Gun

To obtain a large probe current, we used a thermal-assisted field emission electron source. The gun column for a commercial scanning electron microscope with a field emission electron source, the Hitachi S800, was used. A power supply system with a high-voltage cable was modified so that a dc heating current of 3 A (maximum) can be applied to the cathode. Although the typical emission current for the S800 is 10 μA, a stable emission current of 100 μA was obtained with a heating current of 2.5 A. The accelerating voltage of the probe can be varied from 500 V to 25 kV.

The electron gun is attached to the sample chamber whose optical axis is along vertical direction. The Mott detector is attached to the chamber whose optical axis is at a 60° angle from the axis of the electron gun. The relation of the arrangement between the gun and the Mott detector is reverse to that of the previous spin SEM (see Fig. 2.3). The Hitachi S800 electron gun is designed to be operated in general in the vertical position, and has not been operated yet at its slant position. Thus, the electron gun was placed vertically, and as a result the Mott detector was converted from vertical position to slanted position.

6.2.3 Objective Lens

Obtaining a smaller probe-diameter requires a low-aberration objective lens. The spherical and chromatic aberration coefficients *Cs* and *Cc* are determined by the shape of the pole pieces and the magnitude of the lens excitation, which is related to focal length. Both aberration coefficients generally decrease with decreasing focal length. Thus, a shorter working distance (WD), which is defined as the distance between the edge of the objective lens and the sample, is preferable for a smaller beam diameter. Furthermore, the secondary electron collector needs to be placed close to the sample to collect most of the secondary electrons (to compensate for the low efficiency of the spin detector).

These two requirements imposed on both the objective lens and the secondary electron collector cause spatial interference between the two. Thus, compromise is necessary. The final shape of the objective lens was determined by trial and error so as to find the optimum *Cs* and *Cc* pair enabling the probe diameter to be less than 20 nm with a large probe current.

Figure 6.1 is a cross sectional drawing of the objective lens and the secondary electron collector. To reduce the WD and prevent interference between the two, the objective lens is given a conical shape. The secondary electron collector and transport optics are placed along the taper of the lens at an angle of 60° from the optical axis of the gun (vertical direction in Fig. 6.1). Thus, a WD of 20 mm is achieved without spatial interference between the lens and the collector. The calculated spherical and chromatic aberration coefficients are 251 and 33.1 mm, respectively when the probe energy is 24 keV and the WD is 20 mm.

The probe diameter is generally calculated from the square root of the squared summation of spherical aberration, chromatic aberration, etc. In this calculation, the electron-intensity distribution within the beam cross-section is assumed to always be a Gaussian distribution. This assumption is not correct, however, and the calculated diameter is not strictly consistent with the resolution.

Recently, however, Sato and Orloff have developed an SEM-resolution calculation method in which the resolution is calculated from an electron-intensity distribution that is not generally a Gaussian distribution.[8] Using their method, we calculated the SEM resolution as a function of the probe current, assuming that the electron-source diameter, the FWHM of the probe energy distribution, and the emission current density are 6 nm, 0.5 eV, and 100 μA per 1.5 sr, respectively. As shown in Fig. 6.2, a minimum resolution of 2.1 nm is obtained at a probe current of 0.75 nA. Since we use a commercially available aperture 0.2 mm in diameter, the SEM resolution and the probe current are 2.5 nm and 1.1 nA. It is difficult for the domain resolution to reach the SEM resolution because the *S/N* of the domain image is lower than that of the SEM image even when the probe current is 1.1 nA. However, this is expected to improve the domain resolution, bringing it close to the calculated SEM resolution of 2.5 nm.

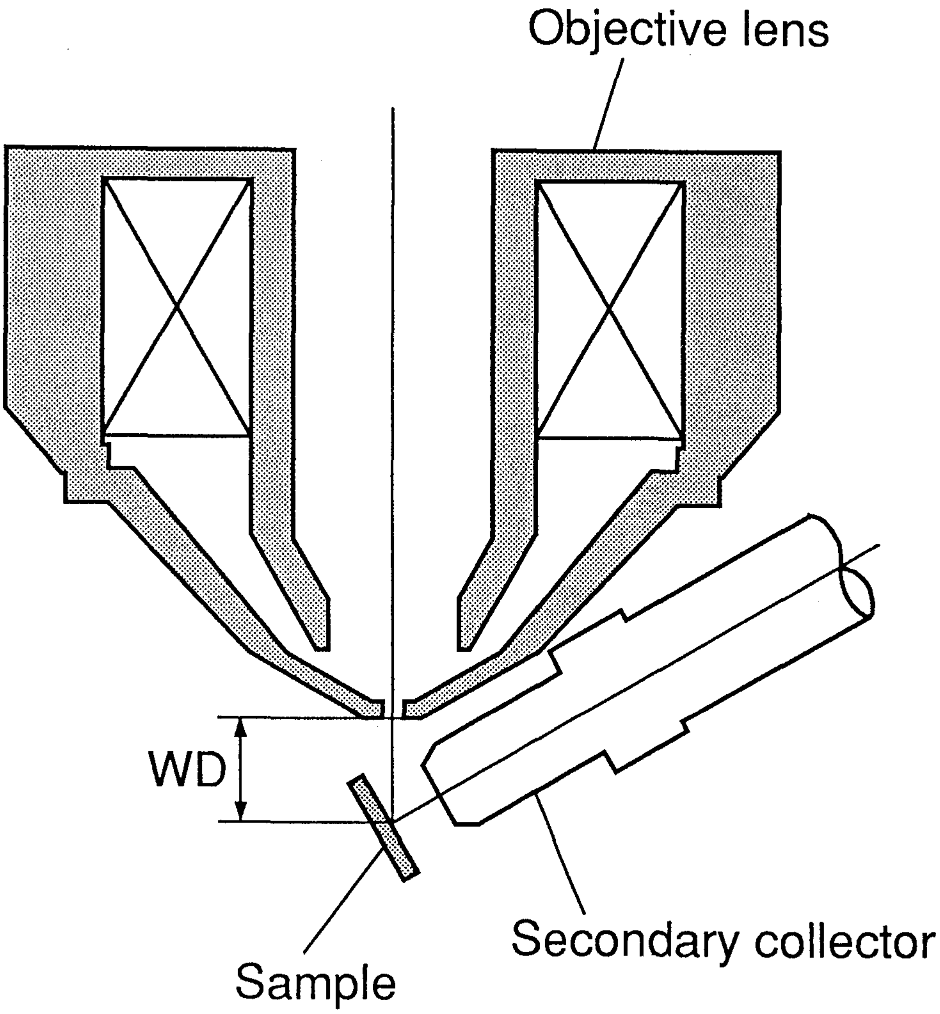

Fig. 6.1. Cross section of the objective lens and the secondary electron collector.[7]

6.2.4 Mott Detector

The figure of merit of the Mott detector is expressed by Eq. (2.5) in Section 2.3. This equation shows that the efficiency of the Mott detector can be increased by increasing $\xi=N/N_o$ (N: the number of electrons detected by a pair of electron detectors, N_o: total number of electrons injected into the Au foil target); that is, by increasing the acceptance angle α of the electron detector (see the inset of Fig. 6.3). The Sherman function, however, decreases with an increasing acceptance angle. Thus, we have evaluated the figure of merit as a function of the acceptance angle by using the calculated scattering-angle dependence of S and N/No,[9] assuming that only elastic scattering occurs at the target. Figure 6.3 shows that the figure of merit F increases monotonically as acceptance angle α increases.

Any increase in the acceptance angle, however, is limited by the spatial interference between neighboring electron detectors, which are placed at four symmetrical positions about the incident beam. Since we use commercially available electron detectors, the diameter of the cylindrical detector is much larger than that of the electron-sensitive area. The maximum attainable acceptance angle α is 28°, which is 1.7 times larger than the 16.2° acceptance angle used in the previous scattering geometry. Both conditions are shown by the dashed lines in Fig. 6.3. Since the ratio F_n/F_p is 2.7 (Fig. 6.3), we get F_n=1.6 x 10^{-5}, when using the measured value of F_p=6 x 10^{-6}.

The previous Mott, whose size is 800 mm in length and 370 mm in diameter, is too large and heavy to be placed with its axis slanted. We have reduced the Mott-detector size to 460 mm in length and 256 mm in diameter, whose volume is a quarter of that of the previous one. In this novel Mott detector, we have adopted an accelerating tube 189 mm in length which is half as long as that of the previous one.

6.2.5 Secondary Electron Collector and Transport Optics

The design of the secondary electron collector is more important than that of the transport

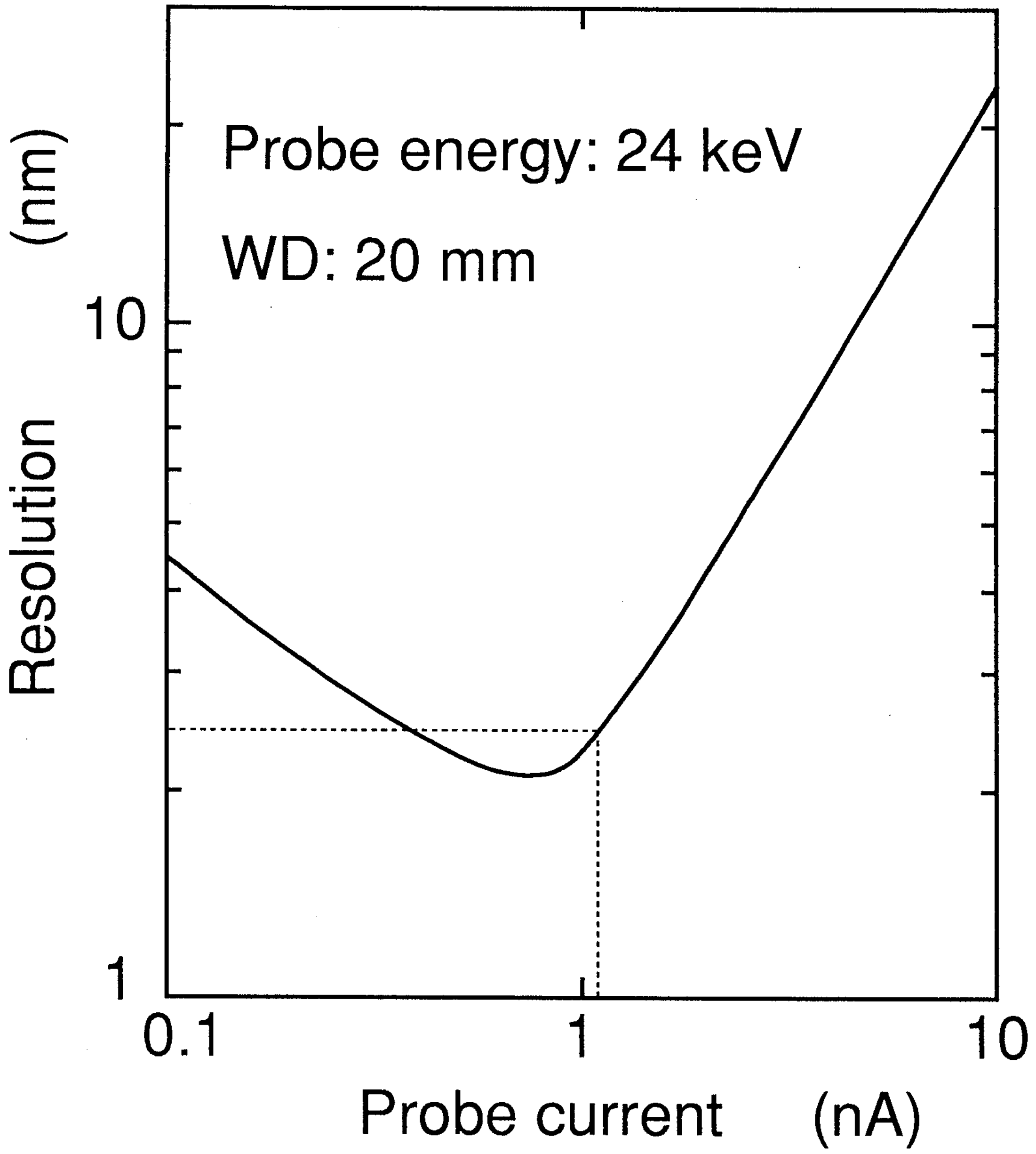

Fig. 6.2. Calculated SEM resolution as a function of the probe current. The dashed lines show the operating condition determined by the diameter of the aperture.[7]

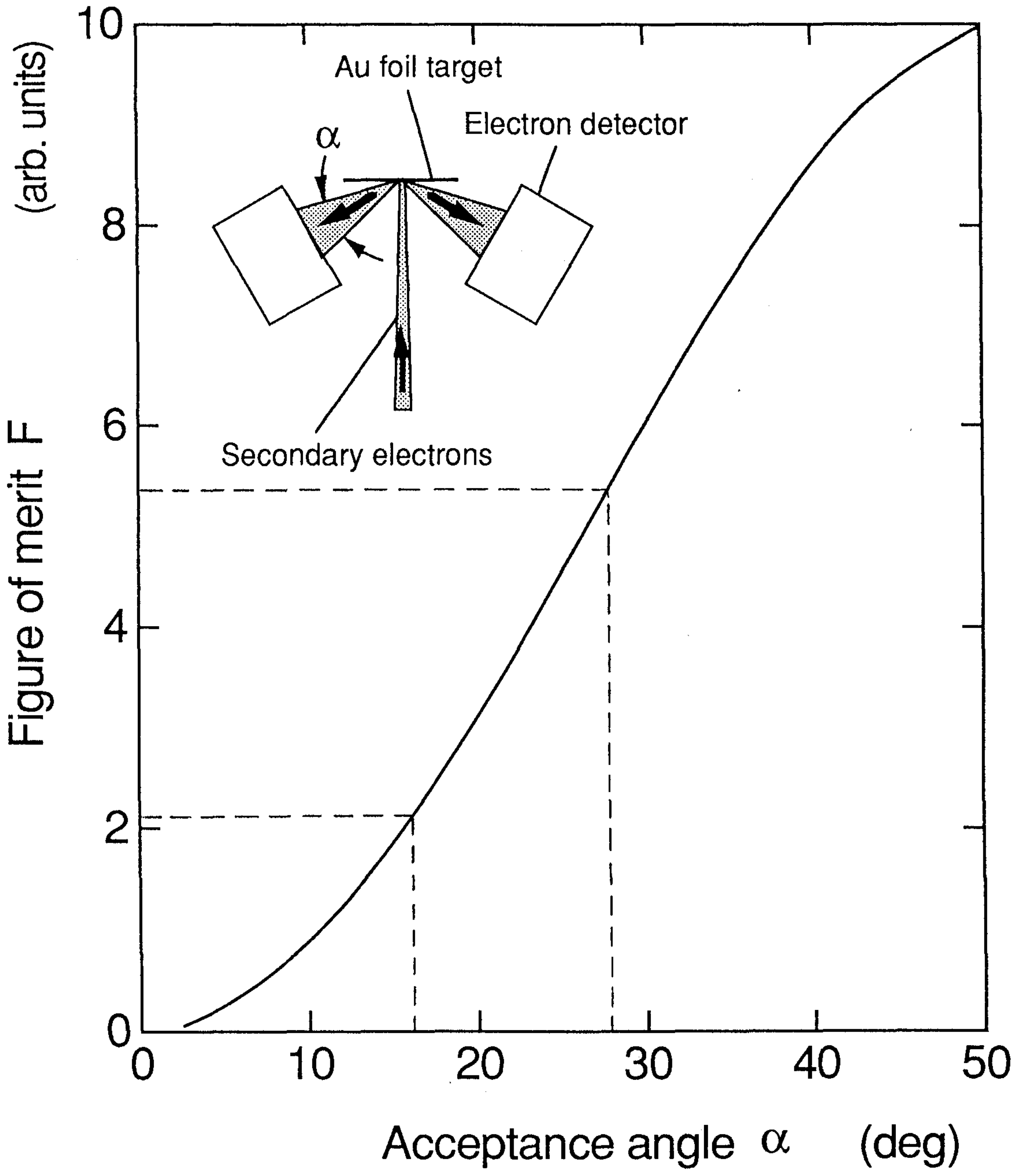

Fig. 6.3. Figure of merit *F* of the Mott detector as a function of the acceptance angle α of electron detector. The inset shows the scattering system of the Mott detector.[7]

optics. The diameter of the cylindrical secondary electron collector is restricted by interference from the objective lens. In addition, secondary electrons just emitted from a sample have a wide angular distribution. Therefore, it is most likely that some of the secondary electrons are lost at the collector.

We have optimized the shape of all electron optical columns and their potential by computer simulation in order to collect and transfer most of secondary electrons. The final designs for the collector electrodes and part of the transport optics are shown in Fig. 6.4, together with the electron trajectories. During the simulation, we assumed that the secondary electrons are emitted from a 0.5-mm-diameter area on the sample at an initial energy of 2 eV and an initial angle of from -80° to +80° from the surface normal. The optics shown here have three lenses: cathode lens L1, bipotential lens L2, and einzel lens L3. The potential of each electrode is shown in Fig. 6.4. All the electrons are collected and then transferred to the optics without colliding with the walls of the electrodes. After these optics, there are two einzel lenses and an accelerating tube for accelerating the electrons to 100 keV. These elements are also designed to be free of electron loss.

6.3 *S/N* of the Image

We used a secondary electron yield η_p of 0.2, the value obtained in copper when a 25-keV probe impinges at a tilt angle 60° from surface normal. [10] By substituting η_p=0.2 and the values of F_n=1.6 x 10^{-5}, ζ_p=1, and I_p =1 nA (calculated in the previous section) into Eq. (6.5)', we obtain

$$\frac{(S/N)_n}{(S/N)_p} \approx 0.8.$$

The *S/N* in the new spin SEM is smaller than that in the previous one, but only by about 20%.

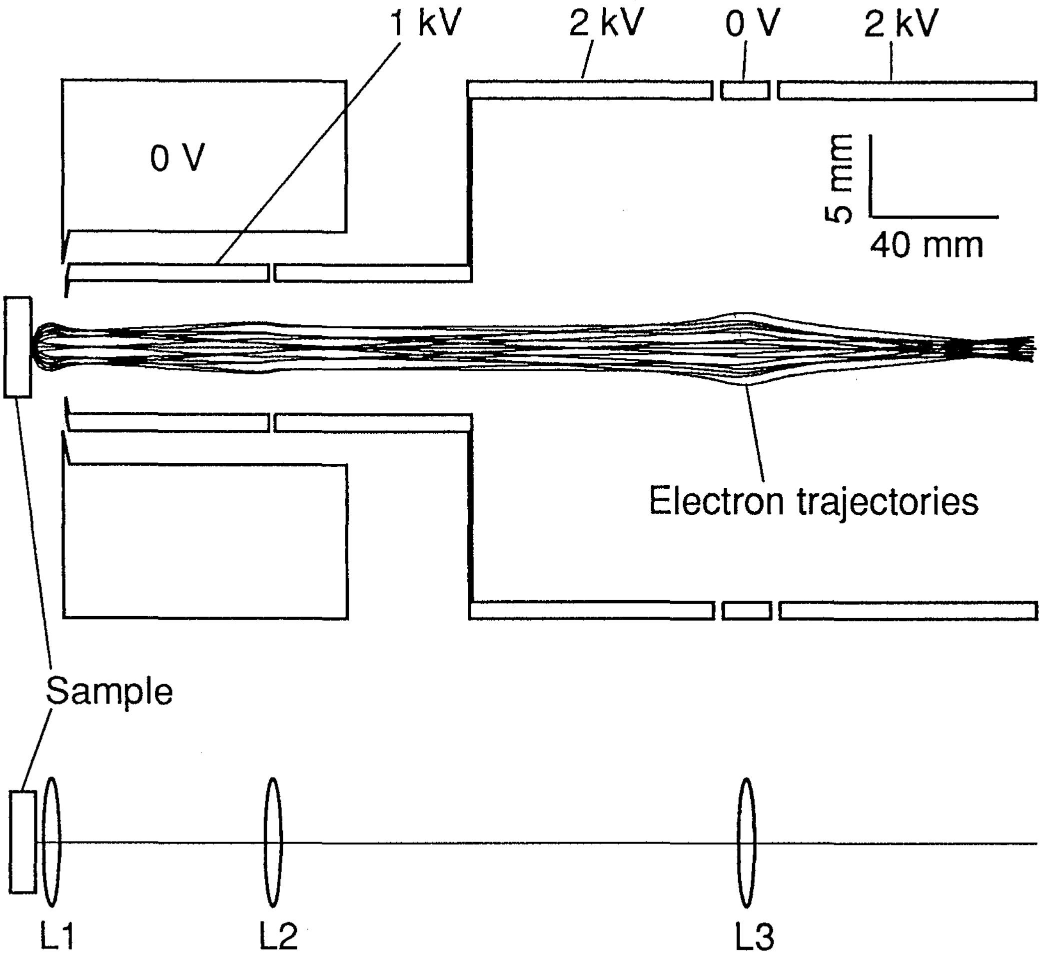

Fig. 6.4. Cross section of secondary electron collector and transport optics, with calculated electron trajectories (electrons emitted from a 0.5-mm-diameter area on the sample, with an initial energy of 2 eV and an initial angle between -80° and +80° with respect to the surface normal). L1, L2, and L3 are electrostatic lenses.[7]

6.4 System

Figure 6.5 is a schematic diagram of the new spin SEM. The sample chamber is usually pumped out to maintain an ultra-high-vacuum pressure of about 10^{-10} Torr by an ion pump (400 l/s) and a titanium sublimation pump (about 2800 l/s). A turbo molecular pump (300 l/s) is used for pumping air out of the chamber from the atmospheric pressure to high-vacuum pressure. The chamber, with the attached electron gun, Mott detector, and vacuum pumps, are set on an antivibration stage so as to prevent the vibration of the base floor from being transmitted into the chamber.

6.5 Experimental Procedure

To check the domain resolution of the present spin SEM, we prepared a CoCrTa thin-film medium recorded at the densities ranging from 20 k to 240 kFCI, for which the repetitive bit lengths are 1270 to 106 nm, respectively. Although the minimum bit length of 106 nm is about five times larger at a spatial resolution of 20 nm, fine structures can be expected in the recorded bit boundaries in the in-plane recording medium, as predicted from the computer simulation results.[11]

The thin-film medium was prepared by dc-sputtering on textured NiP-plated Al-substrate, and magnetic recording was done with a thin-film head. The recorded disk was cut into a piece roughly 10 x 10 x 1.5-mm^3 and the carbon protective film on the medium was removed by plasma ashing using oxygen. The domains were observed at a base pressure of about 10^{-10} Torr after sample surface cleaning by Ar-ion sputtering. The thermal-assisted field emission gun was operated at an accelerating voltage of 25 kV and an emission current of 100 μA. The measured probe current was typically 1 nA. It took about one hour to produce a domain image.

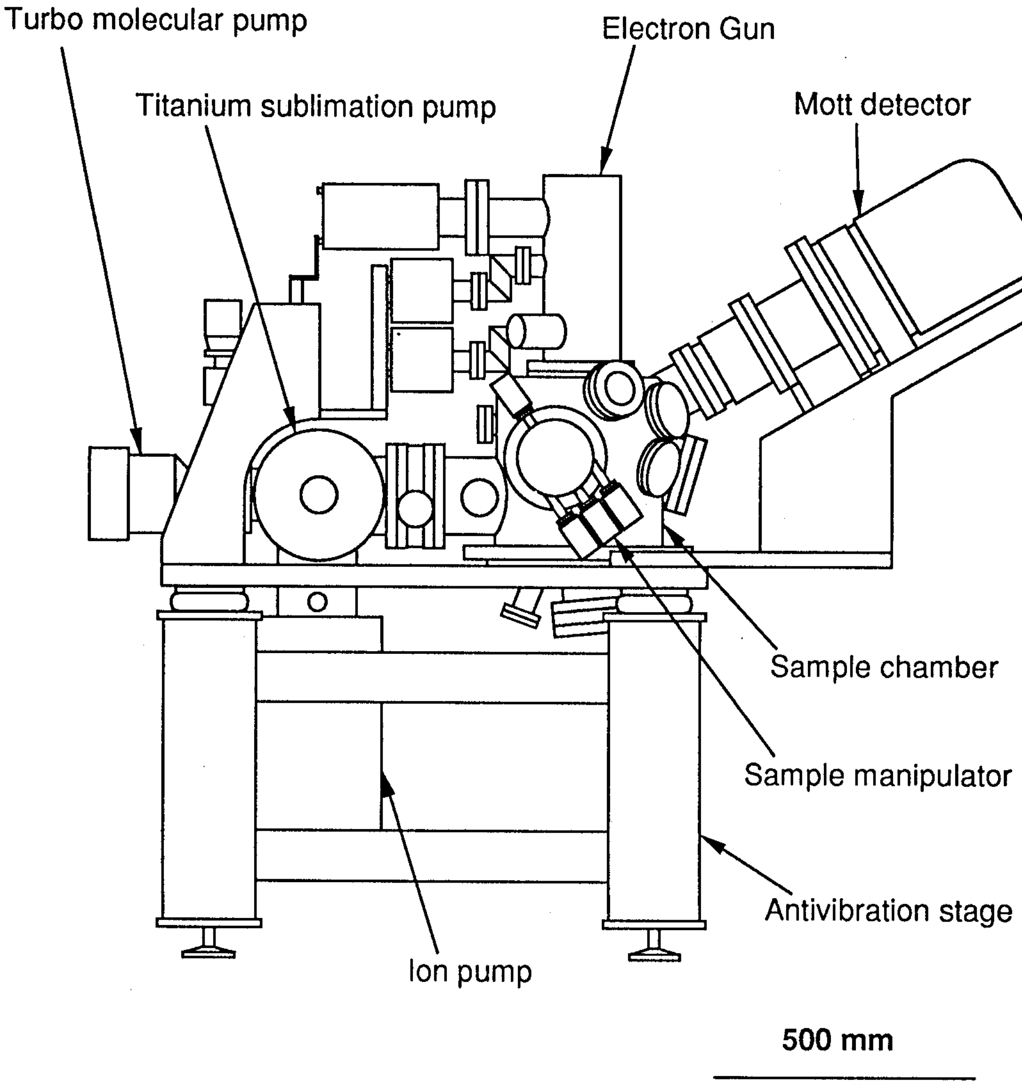

Fig. 6.5. Schematic diagram of the spin SEM.

6.6 Results and Discussion

Figure 6.6 shows recorded bit images, each of which is composed of the magnetization component along the horizontal direction (track direction). The 10-μm-wide bands running from left to right are recorded tracks. The vertical stripes in the tracks of 20 k to 80 kFCI indicate recorded bits with bit lengths of 1270 and 318 nm, respectively. However, those in the tracks of more than 100 kFCI cannot be observed at this magnification.

Figures 6.7(a) and (b) show the magnified bit images of the 100- and 240-kFCI tracks shown in Fig. 6.6. The respective bit lengths are 254 and 106 nm. In Fig. 6.7(a) a black and white bit pattern is clearly visible. The domains bridging neighboring bits appear here and there, and the bit boundaries fluctuate in a zigzag fashion. In Fig. 6.7(b) the bit pattern cannot be recognized in the track. Although the configuration of the domain is, on the whole, long and slender along the track direction, there are domains of various-sized particularly fine domains. These fine domains are better for checking the spatial resolution of our spin SEM than are the bit boundaries shown in Fig. 6.7(a). Thus, we observed a magnified image of Fig. 6.7(b).

Judging from the smallest identifiable domain seen in Fig. 6.8, we have concluded that the spatial resolution of our spin SEM is 20 nm. Since the grain size of the same kind medium is found by TEM observation to be 10 nm, the 20-nm domain might be formed from a couple of grains whose magnetization directions are almost the same, which is consistent with the computer simulation results.[12]

We have not yet attained a domain resolution close to the calculated SEM resolution of 2.5 nm, although we got an SEM resolution of less than 10 nm in the SEM image produced by the sum of the electron counts at four electron detectors in the Mott detector. Our inability to reach this theoretical limit might be explained as follows: the probe did not focus down to 2.5 nm because the condition of the gun or of the objective lens, or both, was not optimum. In addition, the sample has no, or very few, magnetic structures smaller than 20 nm.

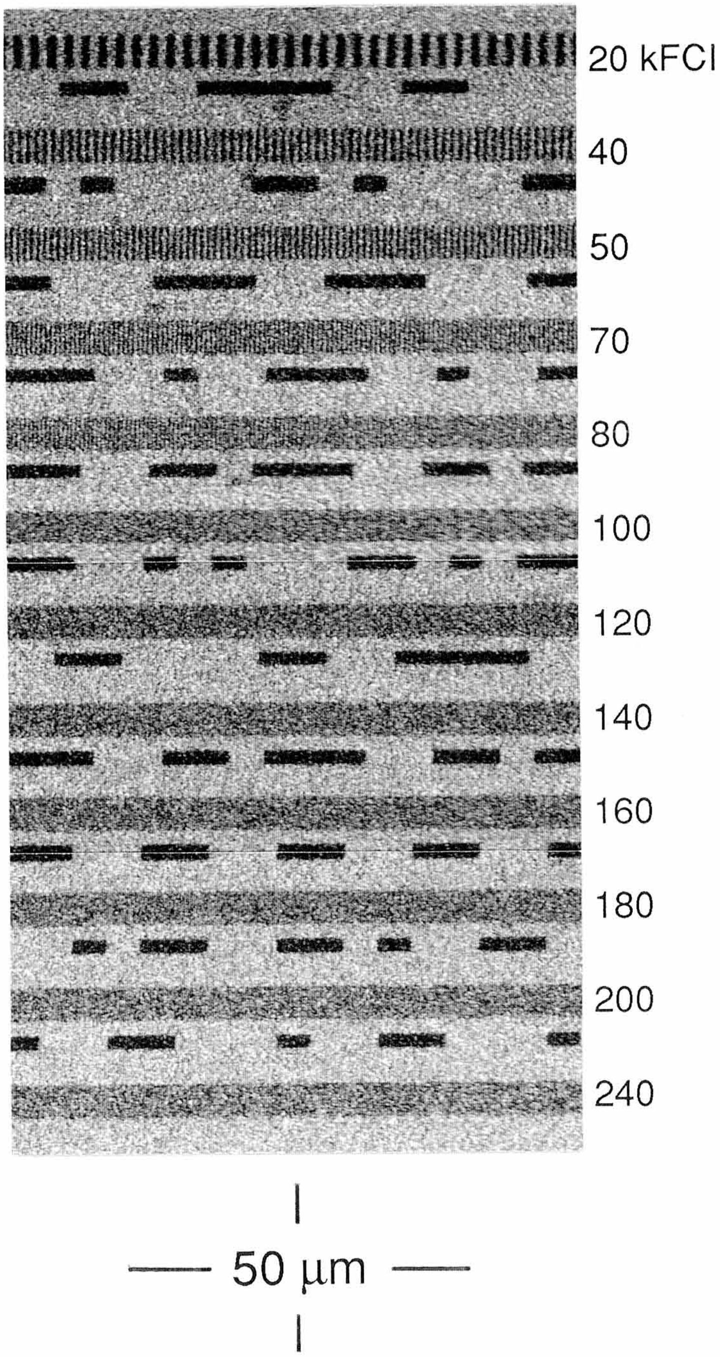

Fig. 6.6. Domain images of recorded bits with densities of from 20 k to 240 kFCI.[7]

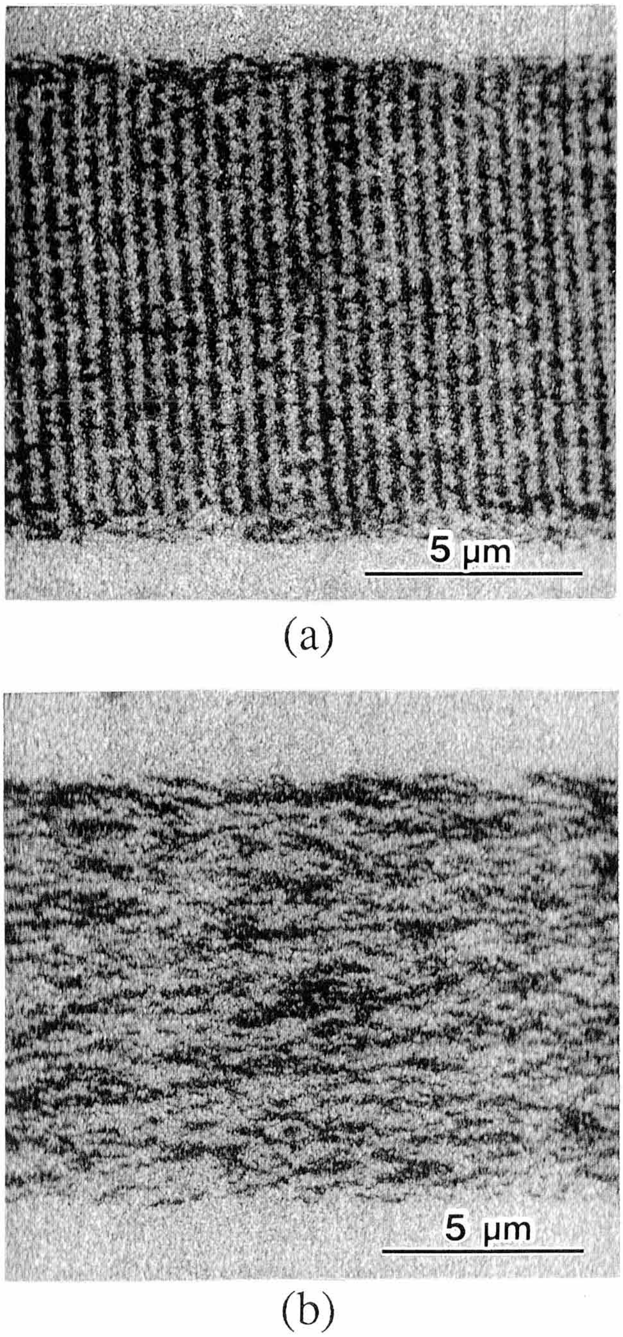

Fig. 6.7. Magnified bit images from Fig. 6.6: (a) 100 kFCI; (b) 240 kFCI.[7]

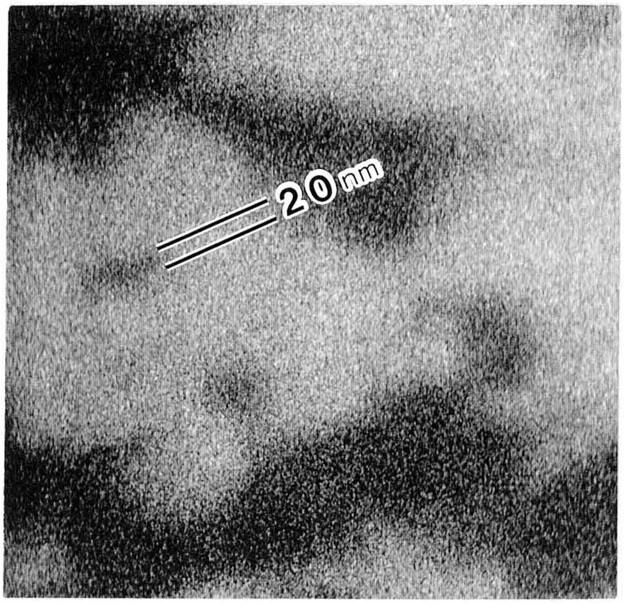

Fig. 6.8. Magnified domain image of Fig. 6.7(b).[7]

6.7 Conclusions

We have developed a high-resolution spin-SEM with a thermal-assisted field emission gun that enables a stable, high emission current of 100 μA. The objective lens in this SEM has spherical and chromatic aberration coefficients of 251 and 33.1 mm, respectively at a working distance of 20 mm. This working distance enables the secondary electron collector to be set close to the sample. We have also developed a Mott detector whose figure of merit is about three times that of our previous detector. The secondary electron collector and transport optics designed for this system allow most of the secondary electrons from the sample to go through to the Au target in the Mott detector. As a result, domain images with a 20-nm resolution have been obtained.

References

1. J. H. Judy, IEEE Trans. Magn. **MAG-29**, 209 (1993).

2. K. Yoshida, T. Okuwaki, N. Osakabe, H. Tanabe, Y. Horiuchi, T. Matsuda, K. Shinagawa, A. Tonomura, and H. Fujiwara, IEEE Trans. Magn. **MAG-19**, 1600 (1983).

3. W. Rave, R. Schafer, and A. Hubert, J. Magn. Magn. Mater. **65**, 7 (1987).

4. J. P. C. Bernards and A. J. den Boef, IEEE Trans. Magn. **MAG-26**, 1515 (1990).

5. G. G. Hembree, J. Unguris, R. J. Celotta, and D. T. Pierce, Scanning Microsc. Suppl. **1**, 229 (1987).

6. H. P. Oepen and J. Kirschner, Phys. Rev. Lett. **62**, 819 (1989).

7. H. Matsuyama and K. Koike, J. Electron Microsopy. to be submitted.

8. M. Sato and A. Orloff, Ultramicroscopy **41**, 181 (1992).

9. L. Lin Shin, Phys. Rev. **133**, A965 (1964).

10. L. Reimer, *Scanning electron microscopy*, (Springer, Berlin, Heidelberg 1985) 144.

11. J-G. Zhu, IEEE Trans. Magn. **MAG-29**, 195 (1993).

12. H. N. Bertram and R. Arias, J. Appl. Phys. **71**, 3439 (1992).

7. Application of 20-nm Resolution Spin SEM

— Domain Observation of Longitudinal Thin Film Media —

7.1 Introduction

It is very important to clarify the noise generating mechanism in longitudinal thin film media to reduce media noise and to attain high-density recording. It is generally accepted that the irregular transition region between recorded bits causes the media noise.[1] Until now, however, media noise characteristics have not been completely understood. Recently, it was demonstrated by computer simulation that media noise power, calculated from the irregular transition structure, increases according to the exchange interaction between grains and that noise power becomes more pronounced at high densities due to stress-induced anisotropy of the media.[2] Khan, et al., conducted domain observations of media composed of the different elements, CoNi and CoCrTa, at a density of 15 kFCI. They concluded that a greater degree of interparticle interaction including exchange and magnetostatic interaction results in cross-bit linkage.[3] However, they did not determine the main factor controlling the magnitude of the interparticle interaction. Moreover, the 15-kFCI bit density is much lower than that of the present recording system. There are few other direct microscopic-observations of bit structures which confirm the simulation results. Therefore, further observation of bit structures is highly desirable, particularly of densities higher than the 100 kFCI used in the present recording system.

The purpose of this Chapter is to clarify the relationship between media noise power and the detailed structure of recorded bits, now studied for the 100 kFCI range recordings, by using the 20-nm spin SEM.[4]

7.2 Experimental Procedure

Two kinds of C/$Co_{96-x}Cr_xTa_4$/Cr thin films, where x is 10 and 16 at%, were prepared by dc sputtering on textured NiP-plated Al-substrate. The magnetic properties of the sample were measured with a vibrating sample magnetometer (VSM). The saturation magnetization, remanent flux density thickness product value, and the coercive force are 610 emu/cm^3, 154 G μm, and 1.93 kOe, respectively for 10 at% Cr medium and 470 emu/cm^3, 168 G μm, and 1.90 kOe, respectively for 16 at% Cr medium. The film thickness is 25 nm for 10 at% Cr medium, and 36 nm for 16 at% Cr medium. Magnetic recordings at densities from 0 to 250 kFCI were made on the media using a thin film head with a gap length of 0.4 μm at a head-to-medium spacing of 0.12 μm. The readback signal voltage from a magnetoresistance head at a head-to-medium spacing of 0.12 μm was measured, and the media noise power was determined using a spectrum analyzer.

The recorded disks were cut into about 10 x 10 x 1.5-mm^3 pieces and the carbon films on the Co alloys were removed by plasma ashing using oxygen. Those pieces were put into the sample chamber in the spin SEM, and domain observation was made at the densities of 50, 100, 140 kFCI under a base pressure on the order of 10^{-10} Torr after sample-surface cleaning by Ar-ion bombardment. The probe beam energy was 25 keV and the typical probe current was about 1 nA. It took about one hour to simultaneously produce two images of the x and y magnetization components (sample surface in-plane components).

7.3 Results and Discussion

Figure 7.1 shows the normalized output signals and the noise powers of the media with 10 and 16 at% Cr as a function of recording density. Both media have almost the same D_{50} recording density, at which the output signal drops to half of that at low density, about 80 kFCI. Thus, it is thought that the transition amplitudes between the bits are almost the same in both media. Although the noise power of the 10 at% Cr medium is about twice as high as that of the 16 at% Cr medium below 180 kFCI, similar behavior is generally observed, i.e., the noise power increases linearly with recording density at less than 75 kFCI and rises at a supralinear rate from 75 kFCI to 180 kFCI.

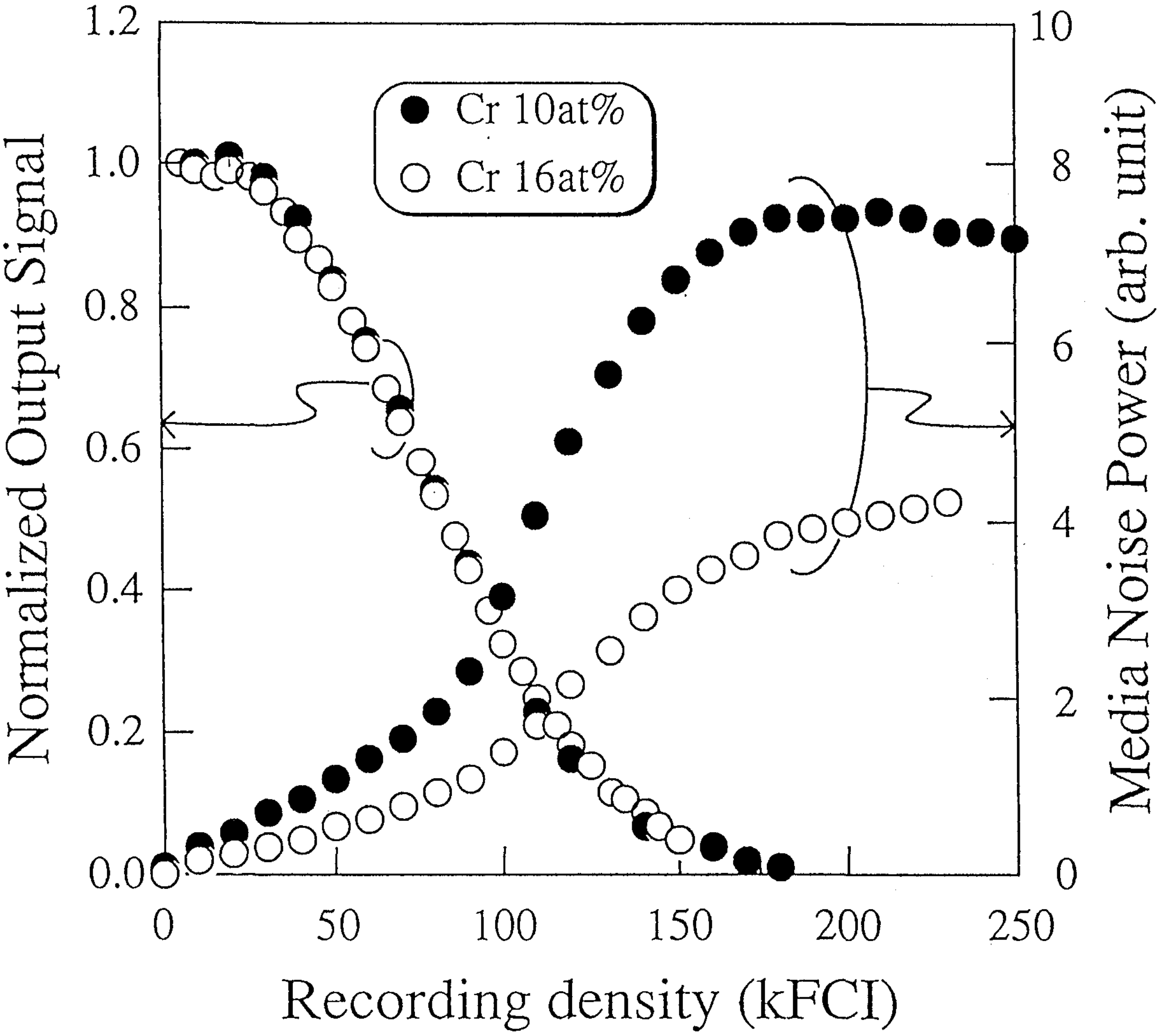

Fig. 7.1. Normalized output signals and media noise powers of 10 at% Cr-CoCrTa and 16 at% Cr-CoCrTa as a function of recording density; closed circles: 10 at% Cr medium; and open circles: 16 at% Cr medium.[4]

Figures 7.2(a), (c), and (e) show the bit images obtained from 50, 100, and 140 kFCI of the 10 at% Cr medium. Figures 7.2(b), (d), and (f) are from the same densities as the former images of the 16 at% Cr medium. The images are of the magnetization component along the track direction (vertical direction in the figure). The bit lengths are 0.50, 0.25, and 0.18 μm. In Figs. 7.2(a) and (b), the widths of the irregular zigzag boundaries of both images are almost equal, as is expected from the same D_{50} in Fig. 7.1, and the maximum values of each are about 0.25 μm. The zigzag wavelength of (a) is apparently longer than that of (b), on average, and the zigzag angle of the bit boundary of (a) is larger than that of (b). Thus, it can be seen that , in these samples, the difference in noise power comes mainly not from the transition boundary width but from the zigzag wavelength. Bertram, et al., introduced a cross-track correlation width of the magnetization and showed that the noise power is proportional to the cross-track correlation width not only in a uniformly magnetized medium but also in a recorded medium.[5,6] In a uniformly magnetized medium, the cross-track correlation width is equal to the average domain width. The cross-track correlation width in a recorded medium is defined at the transition center and qualitatively represents the average length of the irregular zigzag wave. Thus, longer irregular-zigzag wavelength results in longer cross-track correlation width. Therefore, this is qualitatively consistent with our results. The origin of the difference in the zigzag wavelength can be seen as follows. Since the zigzag transition width is almost equal in the two media, longer zigzag-wavelength corresponds to larger zigzag angle. The zigzag half-angle is given by Freiser [7] as

$$\theta = \pi \frac{\sqrt{\pi A}}{8 M_S D},$$

where θ is the zigzag half-angle, A the exchange constant, M_S the saturation magnetization, and D the film thickness. Since $\theta \sim 30°$ from Fig. 7.2(a), (M_S=610 emu/cm^3, D=25 nm) for the 10 at% Cr medium and $\theta \sim 20°$ from Fig. 7.2(b), (M_S=470 emu/cm^3, D=36 nm) for the 16 at% Cr medium, A= 1.3 x 10^{-6} erg/cm for the former and A= 0.7 x 10^{-6} erg/cm can be obtained for the latter. Thus, the larger exchange interaction causes the longer zigzag wavelength. This is also qualitatively consistent with the result obtained from the simulation by Bertram, et al., that the cross-track correlation width increases according to the exchange interaction.[6] As for the origin of the difference in exchange interaction, since the main difference between the two media is the Cr concentration, the above result seems to indicate that the Cr works to reduce the exchange interaction.

In Figs. 7.2(c) and (d), domain-bridging neighboring bits appear at several local areas. It is considered that the bridging occurs since the bit length of 0.25 μm is almost equal to the maximum width of the zigzag boundary obtained from (a) and (b). As is expected, considering the previous experiment at the low densities,[8] the bit bridging begins to increase in both media at the density at which the noise begins to increase supralinearly. The zigzag angle of (c) is larger than that of (d) with the same result as in (a) and (b). The zigzag wavelength in Fig. 7.2(c) is much longer than that of (d), on average, which in turn means that the cross-track correlation width of (c) is longer than that of (d).

The bit structure of Fig. 7.2(e) is much more broken up than that of (f). Thus, it is quite natural that the noise power of (e) is larger than that of (f). In (e) and (f), the bridging length is greater and extends along the track direction for several bit lengths. In particular, many domain islands are observed in (e), and the island widths along the cross-track direction, thought to be related to the zigzag wavelength in (a)-(d), is greater than that of (f), which is the same tendency as in the wavelengths of the previous images of 50 and 100 kFCI. These island widths will approximate the cross-track correlation widths (domain widths) of uniformly magnetized media because, according to the density increase, the medium is close to being in an ac-erased state, i.e., a uniformly nonmagnetized state. Although the medium at a density of 140 kFCI has not completely reached the ac-erased state. Thus, the cross-track correlation width of (e) is expected to be greater than that of (f), which is also thought to be due to the difference in the exchange interaction between the media.

Figure 7.3 shows domain images of cross-track direction magnetization components for the same areas as those in Fig. 7.2. To compare the magnetic contrast between the high- and

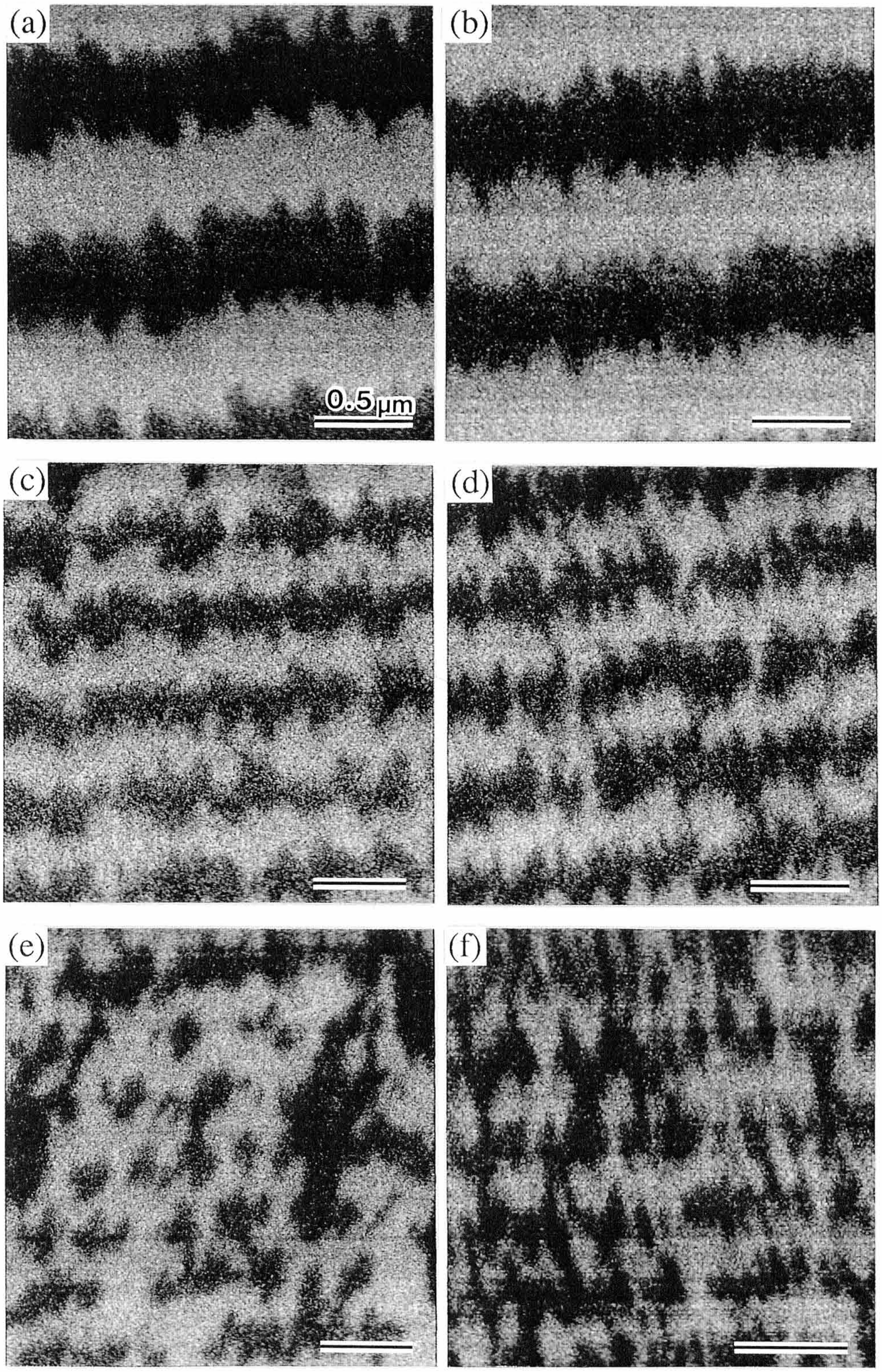

Fig. 7.2. Bit images are of the magnetization component along the track direction. Images (a), (c), and (e) are obtained from 10 at% Cr-CoCrTa, and correspond to 50, 100, and 140 kFCI. Images (b), (d), and (f) are from 16 at% Cr-CoCrTa and correspond to the same densities as the previous images.[4]

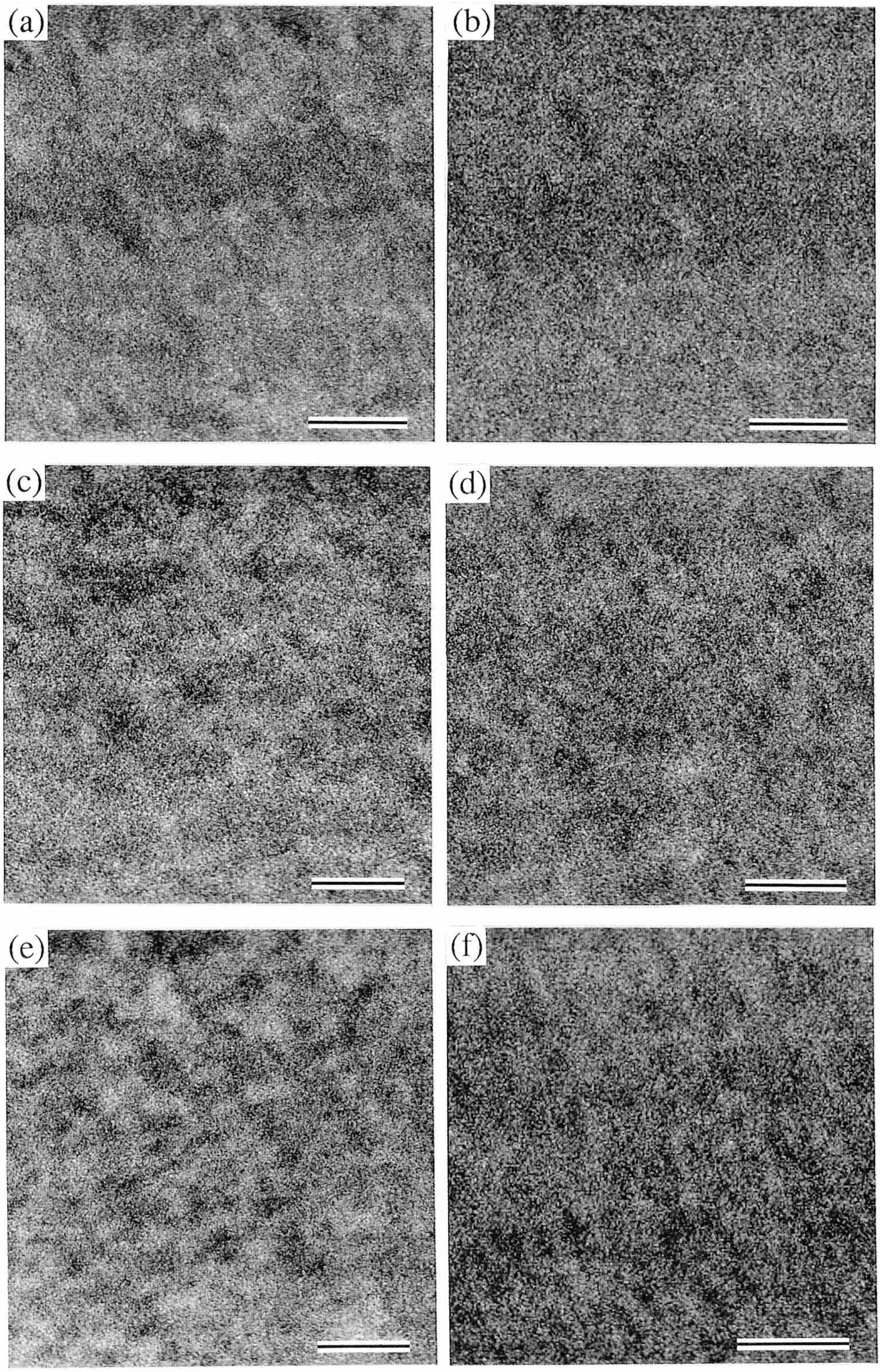

Fig. 7.3. Bit images at the same areas of Fig. 2 are of the magnetization component along the cross-track direction. Images (a), (c), and (e) are obtained from 10 at% Cr-CoCrTa, and correspond to 50, 100, and 140 kFCI. Images (b), (d), and (f) are from 16 at% Cr-CoCrTa and correspond to the same densities as the previous images.[4]

low-noise media bit images in Fig. 7.3, each domain contrast in Fig. 7.3 is normalized by the magnitude of each magnetization value. In Fig. 7.3(a), black and white contrast of small size domains appears at the transition regions as can be seen by comparing them with Fig. 7.2(a). On the contrary, magnetic contrast almost disappears in Fig. 7.3(b). This indicates that the magnetization angle-fluctuation in the transition region is somewhat larger in (a) than that in (b). The domain contrast in (c) is similar to that of (a). In (e), there are various sized domains extending over all of the area. The minimum domain size is around 30 nm, corresponding to the widths of several grains, judging from grain observations of the same kind of media using a transmission electron microscope. On the other hand, domain contrast in Figs. 7.3(d) and (f) is lower than in (c) and (e). As a result, the magnetization angle-fluctuation in high-noise media is greater than in low-noise media for all densities subject to the condition that the magnetization fluctuations below 30 nm are ignored due to SEM resolution limitations. Since the exchange interaction directs the magnetization of the neighboring grains toward the same direction, this is further evidence that the exchange interaction is greater in the low Cr concentration medium.

7.4 Conclusions

We have experimentally analyzed the noise generating mechanism in longitudinal thin film media. The media noise power is determined mainly by the zigzag wavelength of the bit boundary. Longer zigzag wavelength is deduced from greater exchange interaction between grains. These results are qualitatively consistent with the simulation, showing that the noise power is proportional to the cross-track correlation width. These results might be explained by the Cr element working to reduce the exchange interaction between grains.

References

1. R. A. Baugh, E. S. Murdock, and B. R. Natarajan, IEEE Trans. Magn. **MAG-19**, 1722 (1983).

2. J. G. Zhu, IEEE Trans. Magn. **MAG-29**, 195 (1993).

3. M. R. Khan, S. Y. Lee, S. L. Duan, J. L. Pressesky, N. Heiman, D. E. Speliotis, and M. R. Scheinfein, J. Appl. Phys. **69**, 4745 (1991).

4. H. Matsuyama, K. Koike, F. Tomiyama, Y. Shiroishi, A. Ishikawa, and H. Aoi, IEEE Trans. Magn. **MAG-30**, (1994). to be published.

5. H. N. Bertram and R. Arias, J. Appl. Phys. **71**, 3439 (1992).

6. H. N. Bertram, I. A. Beardsley, and X. Che, J. Appl. Phys. **73**, 5545 (1993).

7. M. J. Freiser, IEEE Trans. Magn. **MAG-23**, 330 (1979).

8. H. Aoi, R. Tsuchiya, Y. Shiroishi, and H. Matsuyama, IEEE Trans. Magn. **MAG-24**, 2715 (1988).

8. Summary

In this study, we have first observed surface Néel walls in thick permalloy-films using the spin-polarized scanning electron microscopy (spin SEM) developed by Koike et al. Moreover, we have developed a data acquisition and display (DAD) system for the spin SEM and built a totally new-designed spin SEM with the resolution of 20 nm. The DAD system has been applied to observe the side plane domains of Fe-C/Ni-Fe/BN multilayers, and the new spin SEM applied to observe the recorded bits of longitudinal thin film media. We summarize the main conclusions of the present work as follows.

[1] Néel walls have been observed on the surface of both 1-µm-thick CoTaZr amorphous film and 0.2, 1.4, and 2.0-µm-thick permalloy films. The magnetization rotation angle across the Néel wall was calculated from the in-plane polarization components P_x and P_y detected by the spin SEM, by which the Néel-wall widths were quantitatively determined. At all thickness ranges, these wall widths are larger than those calculated from the one-dimensional wall model. The wall widths of 0.2 and 1.4-µm-thick samples are comparatively consistent with the result of the two-dimensional wall model predicted by Hubert. However the width of the 2.0-µm-thick sample is much larger than that of the Hubert model.

[2] A data-acquisition and display system for the spin SEM has been developed. This DAD system enables high-speed scanning, computing, recording of Px and P_y, multi and magnified scanning for ease of operation, obtaining a constant-noise image even when secondary-electron intensity varies due to surface orientation, image formation for an arbitrary component, vector mapping of the magnetization distribution, and angle image of the magnetization direction in both black and white and color representation. It has been confirmed that the spin SEM with the DAD system is a powerful tool for the study of magnetic microstructures for industrial applications, especially magnetic recording, and for basic research.

[3] The first domain observations of the top and side planes of rectangular four Fe-C/Ni-Fe/BN multilayers laminated on Cu and amorphous-Si substrates have been made. From the domain images of the side planes, it was found that the films do not always show the predicted energy minimum structure where the magnetization direction alternates layer by layer. Two possible causes for these results are suggested, however further study is necessary to clarify the details.

[4] We have developed a high-resolution spin SEM with a thermal-assisted field emission gun that enables a stable and high emission current of 100 μA. We have developed an objective lens whose spherical and chromatic aberration coefficients are respectively 251 and 33.1 mm at the working distance of 20 mm. This working distance enables a secondary electron collector to be located close to the sample. We have also developed a Mott detector whose figure of merit is about three times that of our previous detector and a secondary collector and transport optics designed so that most of the secondary electrons from the sample go through to the Au target in the Mott detector. As a result, domain images with a 20 nm resolution have been produced.

[5] We have experimentally analyzed the noise generating mechanism in longitudinal thin film media. The media noise power is determined mainly by the zigzag wavelength of the bit boundary. Longer zigzag wavelength is deduced from greater exchange interaction between grains. These results are qualitatively consistent with the simulation, showing that the noise power is proportional to the cross-track correlation width. These results might be explained by the Cr element working to reduce the exchange interaction between grains.

Acknowledgments

The author expresses his most sincere gratitude to Prof. Yoshihito Miyako of Osaka University for critical reading of this manuscript and stimulating discussions.

This work reported here was carried out at Advanced Research Laboratory (ARL), Hitachi, Ltd. The author gives thanks to Drs. Eiichi Maruyama, former general-manager, Shojiro Asai, present general-manager, and Atsushi Suzuki, vice-general manager, of ARL, Hitachi, Ltd. for giving him the opportunity to conduct this research. He also thanks to Dr. Kazuyuki Koike (ARL, Hitachi, Ltd.) for his continuous stimulus and invaluable discussions on various aspects throughout the course of this work. He is very thankful to Dr. Akira Fukuhara (ARL, Hitachi, Ltd.) and Prof. Kazunobu Hayakawa (Hokkaido University) for their valuable advice and encouragement during the course of this study. Thanks are also due to Dr. Mitsugu Sato and Mr. Takao Kumada of Instrument Division, Hitachi, Ltd. for their advice in designing the objective lens. The author expresses his gratitude to Mr. Yoshimasa Kondo of Instrument Division, Hitachi, Ltd.; Mr. Masafumi Kanetomo, Mr. Kouji Kawaguchi, and Mr. Tokushichi Igarashi of Central Research Lab., Hitachi, Ltd.; Mr. Shigeo Kubota, Mr. Shokichi Matsunami, and Mr. Noboru Moriya of ARL, Hitachi, Ltd. for their technical support in designing and constructing the spin-SEM system. His thanks are also extended to his colleagues, Mr. Takashi Furukawa and Mr. Teruo Kohashi, in his group who helped directly and indirectly with his research.

The author appreciates Dr. John Bonevich of ARL, Hitachi, Ltd. for his assistance in the preparation of this manuscript. Finally, the author wishes to especially thank Mrs. Kimi Matsuyama of ARL, Hitachi, Ltd. for her support during the long term study of this work.

List of Publications

1. S. Chikazawa, H. Matsuyama, C. J. Sandberg, and Y. Miyako, "Comment on the field dependence of susceptibility in spin glass: $(T_{0.9}V_{0.1})_2O_3$," J. Phys. Soc. Jpn. **51**, 1037 (1982).

2. S. Chikazawa, S. Taniguchi, H. Matsuyama, and Y. Miyako, "The properties of nonlinear susceptibility in AuFe," J. Magn. Magn. Mater. **34**, 1355 (1983).

3. T. Taniguchi, H. Matsuyama, S. Chikazawa, and Y. Miyako, "Linear and non-linear susceptibilities in canonical spin glass AuFe (1.5 at.%Fe)," J. Phys. Soc. Jpn. **52**, 4323 (1983).

4. H. Matsuyama, T. Takano, Y. Tazuke, T. Sato, Y. Miyako, C. D. Amarasekara, and P. H. Keesom, "Random magnet of quasi-one dimensional conductor $Na_{0.2}V_2O_5$ bronzes," J. Phys. Soc. Jpn. **52**, 77 (1983).

5. K. Koike, H. Matsuyama, H. Todokoro, and K. Hayakawa, "Spin-polarized scanning electron microscope for magnetic domain observation," Jpn. J. Appl. Phys. **24**, L542 (1985).

6. K. Koike, H. Matsuyama, H. Todokoro, and K. Hayakawa, "Spin-polarized scanning electron microscopy," Jpn. J. Appl. Phys. **24**, 1078 (1985).

7. K. Koike, H. Matsuyama, H. Todokoro, and K. Hayakawa, "High spatial resolution spin-polarized scanning electron microscope," Jpn. J. Appl. Phys. **24**, L833 (1985).

8. K. Koike, H. Matsuyama, K. Mitsuoka, and K. Hayakawa, "Spin-polarized scanning electron microscope for analysis of complicated magnetic domain structure," Jpn. J. Appl. Phys. **25**, L758 (1986).

9. K. Koike, H. Matsuyama, K. Hayakawa, K. Mitsuoka, S. Narishige, Y. Sugita, K. Shiiki, and C. Saka, "Observation of Néel structure walls on the surface of 1.4 μm-thick magnetic domain structure," Appl. Phys. Lett. **49**, 980 (1986).

10. H. Matsuyama, K. Koike, K. Hayakawa, K. Mitsuoka, S. Sudo, S. Narishige, and Y. Sugita, "Spin-polarized-SEM observation of surface magnetization across domain wall in permalloy films," IEEE Trans. Magn. **MAG-23**, 2173 (1987).

11. K. Mitsuoka, S. Sudo, S. Narishige, M. Hanazono, Y. Sugita, K. Koike, H. Matsuyama, and K. Hayakawa, "Magnetic domains of permalloy films for magnetic recording thin film heads observed spin-polarized SEM," IEEE Trans. Magn. **MAG-23**, 2155 (1987).

12. K. Koike, H. Matsuyama, and K. Hayakawa, "Spin-polarized scanning electron microscopy for micro-magnetic structure observation," Scanning Microsc. Suppl.**1**, 241 (1987).

13. K. Koike, H. Matsuyama, and K. Hayakawa, "Spin-polarized scanning electron microscope with a thumb-size spin detector," Jpn. J. Appl. Phys. **27**, L1352 (1988).

14. H. Aoi, R. Tsuchiya, and H. Matsuyama, "A study on thin-film-media noise by magnetic domain observation," IEEE Trans. Magn. **MAG-24**, 2715 (1988).

15. H. Matsuyama and K. Koike, "A data-acquisition and display system for spin-polarized scanning electron microscopy," J. Electron Microsc. **39**, 92 (1990).

16. H. Matsuyama and K. Koike, "Side plane domain observation of Fe-C/Ni-Fe/BN multilayers with a spin polarized scanning electron microscope," Appl. Phys. Lett. **57**, 2028 (1990).

17. H. Matsuyama and K. Koike, "A data-acquisition and display system for spin-polarized scanning electron microscopy (spin SEM)," Rev. Sci. Instrum. **62**, 970 (1991).

18. K. Koike, H. Matsuyama, W. J. Tseng, and J. C. M. Li, "Fine magnetic domain structure of stressed amorphous metal," Appl. Phys. Lett. **62**, 2581 (1993).

19. S. Sudo, K. Mitsuoka, K. Koike, H. Matsuyama, and Y. Sugita, "Observation of magnetic stripe domains in Ni-Fe films using spin-SEM," Jpn. J. Appl. Phys. **33**, L30 (1994).

20. H. Matsuyama, K. Koike, F. Tomiyama, Y. Shiroishi, A. Ishikawa, and H. Aoi, "High spatial-resolution domain-observation of longitudinal thin film media by spin-polarized scanning electron microscopy," IEEE Trans. Magn. **MAG-30**, (1994). to be published.

21. H. Matsuyama and K. Koike, "20-nm resolution spin-polarized scanning electron microscope," J. Electron Microsopy. to be submitted.